



The Influence of Large Coherent Structures on Near-Surface and Entrainment Zone Properties in Convective Boundary Layers



Katherine Fodor

Hamburg 2020

Hinweis

Die Berichte zur Erdsystemforschung werden vom Max-Planck-Institut für Meteorologie in Hamburg in unregelmäßiger Abfolge herausgegeben.

Sie enthalten wissenschaftliche und technische Beiträge, inklusive Dissertationen.

Die Beiträge geben nicht notwendigerweise die Auffassung des Instituts wieder.

Die "Berichte zur Erdsystemforschung" führen die vorherigen Reihen "Reports" und "Examensarbeiten" weiter.

Anschrift / Address

Max-Planck-Institut für Meteorologie
Bundesstrasse 53
20146 Hamburg
Deutschland

Tel./Phone: +49 (0)40 4 11 73 - 0
Fax: +49 (0)40 4 11 73 - 298

name.surname@mpimet.mpg.de
www.mpimet.mpg.de

Notice

The Reports on Earth System Science are published by the Max Planck Institute for Meteorology in Hamburg. They appear in irregular intervals.

They contain scientific and technical contributions, including Ph. D. theses.

The Reports do not necessarily reflect the opinion of the Institute.

The "Reports on Earth System Science" continue the former "Reports" and "Examensarbeiten" of the Max Planck Institute.

Layout

Bettina Diallo and Norbert P. Noreiks
Communication

Copyright

Photos below: ©MPI-M
Photos on the back from left to right:
Christian Klepp, Jochem Marotzke,
Christian Klepp, Clotilde Dubois,
Christian Klepp, Katsumasa Tanaka



The Influence of Large Coherent Structures on Near-Surface and Entrainment Zone Properties in Convective Boundary Layers



Katherine Fodor

Hamburg 2020

Katherine Fodor

aus Gloucester, United Kingdom

Max-Planck-Institut für Meteorologie
The International Max Planck Research School on Earth System Modelling
(IMPRS-ESM)
Bundesstrasse 53
20146 Hamburg

Universität Hamburg
Geowissenschaften
Meteorologisches Institut
Bundesstr. 55
20146 Hamburg

Tag der Disputation: 20. April 2020

Folgende Gutachter empfehlen die Annahme der Dissertation:

Prof. Dr. Juan Pedro Mellado

Prof. Dr. Bjorn Stevens

Vorsitzender des Promotionsausschusses:

Prof. Dr. Dirk Gajewski

Dekan der MIN-Fakultät:

Prof. Dr. Heinrich Graener

Front cover image used with kind permission of Juan Pedro Mellado. This document was typeset using the classicthesis template developed by André Miede and Ivo Pletikosić available at: <https://bitbucket.org/amiede/classicthesis/>.

The first priority should be given to the study of basic physical mechanisms of turbulence with the emphasis on qualitative aspects, keeping in mind a somewhat old-fashioned view that curiosity drives better science than 'strategies'. This priority includes the study of turbulence itself (*per se*), rather than multitudes of its models. From the basic point of view, it seems not justified to put too much (often futile) effort into its modelling which mostly is mimicking it without much understanding, as the former is not synonymous to the latter.

— Tsinober (2009, p. 345)

ABSTRACT

Turbulent flows exhibit not only chaotic motion, but also coherent structures. In the convective boundary layer (CBL), these structures take the form of circulation cells or rolls on the scale of the boundary layer depth (referred to here as “large scale”). The influence of these large-scale structures on the small-scale eddies embedded within them challenges our understanding of the surface layer and of the entrainment process. Using conditional analysis to isolate the behaviour within different parts of the large-scale structures and direct numerical simulation to accurately represent the full range of turbulence scales, we address three open questions regarding the influence of large coherent structures on the surface layer and entrainment zone of the CBL.

The first question tackles the failure of Monin–Obukhov similarity theory (MOST) in free convection. Surface-layer statistics have been found to deviate from the scaling laws predicted by MOST and various hypotheses have been proposed to explain this. We test the hypothesis that large-scale downdrafts are the primary culprit, as they introduce non-local properties to the surface layer and thereby violate the assumption of no interaction with the outer layer. We find that the buoyancy and vertical velocity variance do not follow MOST within large-scale downdraft regions, but neither do they in large-scale updraft regions. The updraft regions are at least as important as the downdraft regions, if not more so, for determining the near-surface behaviour and hence the cause of departures from MOST is not as straightforward as has been hypothesised.

The second question is whether more idealised flows with similar large coherent structures to the CBL exhibit similar near-surface behaviour. In particular, we compare surface-layer properties between the shear-free CBL and Rayleigh–Bénard convection. We find that statistical properties in the near-surface region of Rayleigh–Bénard convection have substantially different behaviour to those in the CBL. This is due to a difference of sign and magnitude of the buoyancy flux at the top of the fluid layer: the small, negative buoyancy flux at the top of the CBL generates weak, warm downdrafts, whereas the large, positive buoyancy flux at the upper plate of Rayleigh–Bénard convection generates strong, cold downdrafts that modify the near-surface region. However, we also find that only a small change to the classical setup of Rayleigh–Bénard convection is needed for surface-layer properties to behave in a similar way to the CBL. By substituting the cooled upper plate for an adiabatic one, the downdrafts are weaker and warmer, resulting in surface-layer statistics that are almost indistinguishable from those in the CBL.

Finally, we reconsider the causes of wind shear enhancement of the entrainment buoyancy flux. The entrainment zone consists partly of non-turbulent, entrained air, and partly of turbulent plumes, associated with the ascending branch of the large-scale circulations, penetrating into the overlying stratification. Our third question asks how wind shear modifies properties within these different regions and how important each of these changes are for increasing the magnitude of the entrainment buoyancy flux. We find that in both the shear-free and the sheared CBL, the buoyancy flux is strongest within turbulent regions. However, wind shear does not increase the magnitude of the flux itself within those regions, but can even weaken it. The important effect of wind shear is that it substantially increases the turbulent area fraction in the entrainment zone, thereby reducing the non-turbulent area where entrainment is much less efficient.

ZUSAMMENFASSUNG

Turbulente Strömungen sind chaotisch, aber sie zeigen auch kohärente Strukturen. In der konvektiven Grenzschicht haben diese Strukturen die Form von Zirkulationen, die so hoch wie die Grenzschicht selbst sind. Hier bezeichnen wir diese Zirkulationen als "großskalige" Strukturen. Der Einfluss von diesen großskaligen Strukturen auf die in sie eingebetteten kleinskaligen Wirbel stellt unser Verständnis der Oberflächenschicht sowie auch des Entrainments in Frage. Wir verwenden statistische Methoden um das Verhalten in verschiedenen Teilen der großskaligen Strukturen zu isolieren und direkte numerische Simulationen um eine genaue Darstellung von allen turbulenten Bewegungsskalen zu haben. Damit adressieren wir drei offene Fragen, die den Einfluss der großen kohärenten Strukturen auf die Oberflächenschicht und Entrainmentzone der konvektiven Grenzschicht betreffen.

Die erste Frage beschäftigt sich mit dem Versagen von Monin–Obukhov Ähnlichkeitstheorie bei freier Konvektion. Vorherige Studien haben gezeigt, dass Statistiken in der Oberflächenschicht von den von der Ähnlichkeitstheorie erwarteten Skalierungsgesetze abweichen. Verschiedene Hypothesen wurden vorgeschlagen, um dies zu erklären. Wir untersuchen die Hypothese, dass großskalige Abwinde dafür verantwortlich sind, da sie nicht-lokale Eigenschaften in die Oberflächenschicht einbringen und damit der Annahme widersprechen, dass es keine Interaktion zwischen der Oberflächenschicht und der Außenschicht gibt. Wir zeigen, dass innerhalb der großskaligen Abwindregionen weder die Varianz der Vertikalgeschwindigkeit noch die des Auftriebs der Ähnlichkeitstheorie folgen. Dies gilt allerdings auch in der großskaligen Aufwindregionen. Die Aufwindregionen sind, wenn nicht sogar bedeutender, mindestens ebenso bedeutend wie die Abwindregionen für die Bestimmung des Verhaltens in der Oberflächenschicht. Damit ist die Ursache der Abweichungen von der Ähnlichkeitstheorie nicht so eindeutig wie bislang angenommen wurde.

Die zweite Frage ist, ob idealisierte Strömungen mit der konvektiven Grenzschicht ähnlichen großen kohärenten Strukturen auch ähnliches Verhalten in der Oberflächenschicht zeigen. Namentlich vergleichen wir die Eigenschaften der Oberflächenschicht der scherungsfreien konvektiven Grenzschicht mit der der Rayleigh–Bénard Konvektion. Wir zeigen, dass sich die statistischen Eigenschaften in der Oberflächenschicht der Rayleigh–Bénard Konvektion wesentlich von der der konvektiven Grenzschicht unterscheiden. Das liegt daran, dass sich das Vorzeichen und die Größenordnung des Auftriebsflusses am oberen Rand der zwei Systemen unterscheiden. Der kleine negative Auftriebsfluss am oberen Rand der konvektiven Grenzschicht erzeugt schwache warme Abwinde, während der große positive Auftriebsfluss am oberen Rand der Rayleigh–Bénard Konvektion starke kalte Abwinde erzeugt. Diese Abwinde in der Rayleigh–Bénard Konvektion haben einen Einfluss auf die Oberflächenschicht. Dennoch zeigen wir auch, dass nur eine kleine Änderung an dem klassischen Versuchsaufbau der Rayleigh–Bénard Konvektion nötig ist, um ähnliche Oberflächenschichtseigenschaften wie die der konvektiven Grenzschicht zu erreichen. Wenn man die gekühlte obere Platte durch eine adiabatische ersetzt, sind die Abwinde schwächer und wärmer, was zu Oberflächenschichtstatistiken führt, die sich fast nicht von denen in der konvektiven Grenzschicht unterscheiden.

Zuletzt überprüfen wir, warum der Entrainmentauftriebsfluss durch Windscherung erhöht wird. Die Entrainmentzone besteht teilweise aus turbulenten Fahnen, die mit

dem aufsteigenden Teil der großskaligen Zirkulationen verbunden sind und durch die darüber liegende stabile Schicht dringt, und teilweise aus nicht turbulenter Luft, die durch Entrainment eingebracht wird. Wir beschäftigen uns mit der Frage wie die Windscherung die Eigenschaften in diesen verschiedenen Regionen ändert und wie wichtig diese Änderungen für den verstärkten Entrainmentauftriebsfluss sind. Wir zeigen, dass der Entrainmentauftriebsfluss innerhalb der turbulente Regionen am stärksten ist, sowohl in der konvektiven Grenzschicht mit als auch ohne Windscherung. Während Windscherung die Stärke des Flusses innerhalb dieser Regionen nicht erhöht, sondern sogar verringern kann, ist der entscheidende Effekt, dass die Windscherung zu einer Vergrößerung der turbulenten und einer Verkleinerung der nicht-turbulenten Region führt, in der das Entrainment viel weniger effizient ist.

PUBLICATIONS RELATED TO THIS DISSERTATION

Appendix A:

Fodor, K., J.P. Mellado and M. Wilczek (2019). "On the Role of Large-Scale Updrafts and Downdrafts in Deviations From Monin–Obukhov Similarity Theory in Free Convection". *Boundary-Layer Meteorol.* 172, pp. 371-396.

Appendix B:

Fodor, K. and J.P. Mellado (2020). "New Insights into Wind Shear Effects on Entrainment in Convective Boundary Layers Using Conditional Analysis". *Submitted to Journal of Atmospheric Sciences*.

ACKNOWLEDGMENTS

There are many people that have had a positive impact during my PhD time and I cannot adequately express my gratitude to all those that have done so. I feel very lucky to have worked in such a friendly, international place and have had many wonderful opportunities and experiences.

I am most grateful to Juan Pedro, who has calmly and competently supervised me throughout my PhD. It has been a pleasure and a privilege to learn from and work with him. More than that, he is a kind and caring person who I am happy to have spent three and a half years getting to know. I am also indebted to him and his family for their incredible hospitality.

In addition to my direct supervision, I have also been supported in various ways by the other members of the Turbulent Mixing Processes group: Armin, Bernhard, Mona and Moritz. Special thanks go to Armin and Bernhard for never once getting frustrated by me repeatedly bursting into their office to ask them a question and also for some truly epic games of Wizard.

Many thanks to my co-supervisor, Gualtiero and my Advisory Panel chair, Cathy, for taking the time and interest to read my progress reports and ask thought-provoking questions. Thanks also to Julia for reviewing my first paper, helping me with the German version of my thesis abstract and always looking so delighted to see me (although I suspect this was partly because I held the key to her secret stash of chocolate that she kept in my office - but thanks for always offering me some!). I also thank Claudia for reviewing my second paper.

I thank everyone that sat on my defence committee: Juan Pedro, Bjorn, Felix, Corinna and Eva-Maria. Especially given the strange circumstances in which my defence took place, everything ran very smoothly. Special thanks go to Felix for helping set up all the technology, and to Bjorn for his careful and accurate review of my thesis.

The members of the IMPRS Office, Antje, Connie and Michela, have been a source of enormous help in many matters. Thank you for being so on top of everything. I am especially grateful to Antje for helping me move flat (twice)!

I am glad to have had such fantastic office mates throughout my time here: Raphaela, Matthias, Geet and Almuth. In particular, I thank Raphaela for helping me settle in when I first arrived at the institute and Geet for answering my endless questions, whether work-related or not.

Various work colleagues have also been great friends outside of work. Elnaz did a marvellous job of being my buddy and I am very grateful to her for treating me to Iranian food on several occasions. Thanks to the Doppelkopf group (Tobias, Clara, Laura S, Bernhard, Veit, Aaron and Rike) for patiently teaching me and for many lively games. I have enjoyed many pub quizzes with Lydi, Shupi, Tom, Andreas, Josefine, Anke, Phillip, Olga, Rafaela, Laura P, Clara and Clarissa. I have also sampled a number of delicious dishes made by the Latin American Night people: Diego, Violetta, David, Pedro, Laura P, Rafaela, Guilherme, Isabella and Geet. I have gone on wonderful bike rides with Geet, Sally, Tobias and Lydi, as well as some memorable walking trips with two Sebastians, Sally, Vimal, Diego, Gabor, Tobias and Johannes.

There were some hobbies of mine that I found it difficult to maintain in Hamburg, one of which was performing music. I am very glad to have met Vinicius, Markus and

De Joy, with whom I was able to enjoy playing in a jazz quartet for a while. I would also like to thank Lukas, for showing me the practice room and for singing some lovely duets with me. Also, thanks to the MPI choir for providing a very pleasant break in the middle of the day.

I have also been exposed to some new things since being in Hamburg: I'm grateful to Sally for making me appreciate swimming in cold water and to Sebastian and Sahir for making me feel welcome when I first started at MPI by taking me climbing with them (even if I did end up mainly going for the delicious veggie burger).

Lastly, thanks to David for being my dream flatmate, to my parents for not having a clue what it is that I did for the last three and a half years, but being very enthusiastic about it anyway, and to Anna for being a kind and supportive sister.

CONTENTS

I UNIFYING TEXT

1	THE ATMOSPHERIC BOUNDARY LAYER AND ITS ROLE IN WEATHER AND CLIMATE	2
1.1	What is the Atmospheric Boundary Layer?	2
1.2	Influence of the ABL on Weather	3
1.3	Influence of the ABL on Climate	3
1.4	A Way Forward	4
2	MODELLING THE CONVECTIVE BOUNDARY LAYER	5
2.1	Why use Direct Numerical Simulation?	5
2.2	An Idealised System	5
2.3	Dimensional Analysis	7
2.3.1	Control Parameters	7
2.3.2	Independent Variables	8
3	LARGE COHERENT STRUCTURES AND SMALL-SCALE TURBULENCE IN THE CONVECTIVE BOUNDARY LAYER	10
3.1	Large Coherent Structures	10
3.2	Small-Scale Turbulence	11
3.2.1	The Surface Layer	12
3.2.2	The Entrainment Zone	13
3.3	Research Questions	14
3.4	Beyond Conventional Statistics	15
4	SUMMARY OF RESULTS	17
4.1	Deviations from Monin–Obukhov Similarity Theory in Free Convection	17
4.2	Rayleigh–Bénard Convection as a Model of the Unstable Atmospheric Surface Layer	18
4.3	Implications of External Intermittency for Understanding Shear-Enhanced Entrainment	20
5	CONCLUSIONS AND OUTLOOK	23
5.1	Response to Research Questions	23
5.2	Looking Back and Ahead	24
5.3	A Final Reflection	25

II APPENDICES

A	ON THE ROLE OF LARGE-SCALE UPDRAFTS AND DOWNDRAFTS IN DEVIATIONS FROM MONIN–OBUKHOV SIMILARITY THEORY IN FREE CONVECTION	28
A.1	Introduction	30
A.2	Formulation	32
A.2.1	Governing Equations	32
A.2.2	Boundary Conditions	32
A.2.3	Dimensional Analysis	34
A.2.4	Numerical Method, Resolution Requirements and Domain Size	38
A.3	Conditional Analysis	39

A.3.1	Defining a Large-Scale Field	39
A.3.2	Conditioning Criteria	42
A.3.3	Area Fraction	43
A.3.4	Buoyancy Statistics	43
A.3.5	Top-Down Scalar Statistics	46
A.3.6	Vertical Velocity Statistics	47
A.3.7	Dependence on Filter Size	47
A.4	Summary and Conclusions	49
B	NEW INSIGHTS INTO WIND SHEAR EFFECTS ON ENTRAINMENT IN CON- VECTIVE BOUNDARY LAYERS USING CONDITIONAL ANALYSIS	53
B.1	Introduction	56
B.2	Numerical Simulations and Analysis Methods	57
B.2.1	Governing Equations	57
B.2.2	Simulations	58
B.2.3	Structure of the Entrainment Zone	59
B.2.4	Conditional Analysis Preliminaries	60
B.3	Definition of Turbulent and Non-turbulent Regions	60
B.4	Turbulent Area Fraction	63
B.5	Wind Shear Effects on the Buoyancy Flux	64
B.5.1	Why is the mean difference term so small?	65
B.5.2	Why does the buoyancy flux in turbulent regions not increase with wind shear?	66
B.6	Summary and Conclusions	68
	BIBLIOGRAPHY	73

ACRONYMS

ABL	Atmospheric Boundary Layer
ASL	Atmospheric Surface Layer
CBL	Convective Boundary Layer
DNS	Direct Numerical Simulation
GCMs	Global Climate Models
LES	Large Eddy Simulation
LSCs	Large-Scale Circulations
MOST	Monin–Obukhov Similarity Theory
PDF	Probability Density Function
RBC	Rayleigh–Bénard Convection
TKE	Turbulent Kinetic Energy
TNTI	Turbulent/Non-Turbulent Interface

Part I

UNIFYING TEXT

THE ATMOSPHERIC BOUNDARY LAYER AND ITS ROLE IN WEATHER AND CLIMATE

The boundary layer is not only the physical interface between the atmosphere and the surface. It also provides an intellectual interface between meteorology and other branches of fluid mechanics. Ideas about how to deal with the problems of turbulence pass from one discipline to another.

— Stewart (1979)

1.1 WHAT IS THE ATMOSPHERIC BOUNDARY LAYER?

The term *boundary layer* owes its origins to Prandtl (1904), who was concerned with the problem of a low-viscosity fluid flowing on the surface of a solid body. Given the small viscosity, the typical approach was to use the equations governing the motion of non-viscous fluids, but solutions of these equations did not match well with experiments. Prandtl was the first to show that this mismatch was due to the existence of a thin layer close to the body - the boundary layer - where the effects of viscosity could not be ignored (Schlichting, 1979).

In principle, boundary layers can be laminar, though in many practical situations they are turbulent. The essence of Prandtl's idea also holds true of the Earth's atmosphere. Most of the atmosphere is occupied by essentially inviscid flow, known as the *free atmosphere*, characterised by the general circulation and wave activity. Between the Earth's surface and the free atmosphere lies the Atmospheric Boundary Layer (ABL), conspicuous for its turbulent nature.

Beyond Prandtl's original concept, the ABL also has several additional features. One distinguishing feature is the presence of density stratification. The ABL may be classified as stable (heavier fluid below lighter fluid), neutral (no stratification) or unstable (lighter fluid below heavier fluid). In the stable and neutral regimes, wind shear is the only source of Turbulent Kinetic Energy (TKE) and buoyancy either plays no role (neutral case) or is a sink of TKE (stable case). In the unstable regime, both wind shear and buoyancy are sources of TKE. In the limiting case of free convection, motion is generated solely by buoyancy differences within the fluid.

Another feature unique to the ABL is the presence of clouds. There are three main types of boundary layer clouds: shallow cumulus, stratocumulus and stratus. Fog may be classed as a branch of the stratus regime, where the cloud extends to the Earth's surface (Garratt, 1992). The situation is complicated by the presence of clouds as there is a two-way interaction between the boundary layer and the cloud layer; the boundary layer acts as a source of heat and moisture for the cloud, whilst the clouds affect the temperature, humidity and growth of the boundary layer (Emmitt, 1978; Moeng, 1998; van Stratum et al., 2014).

Qualitative differences between the ABL and the free atmosphere can result in a tendency to think of the boundary layer as a standalone sub-system within the troposphere. Whilst sometimes practical to do so, it is worthwhile to remind ourselves that

the boundary layer is what couples the free atmosphere above with the surface beneath and is therefore closely tied to both weather and climate.

1.2 INFLUENCE OF THE ABL ON WEATHER

Weather is a fundamentally atmospheric phenomenon. One important way in which the ABL plays a role in the weather we experience has already been mentioned, namely by modulating the presence of low-level cloud. Radiative cooling of the Earth's surface overnight can result in the development of fog if the cooling is sufficient to cause the air near the surface to condense. During the day, the Earth's surface warms, creating an unstable layer in which thermals of air rise, transporting water vapour with them. As the air parcels rise, they also cool and may become saturated, at which point they condense and start to form low-level clouds. Particularly strong thermals may overcome the inversion layer that caps the daytime boundary layer. If the environmental temperature decreases faster with height than the moist adiabatic lapse rate, the saturated air parcel becomes positively buoyant and continues to ascend, generating deeper cumulus clouds (Siebesma, 1998). The moisture, temperature, wind speed and degree of inhomogeneity in the boundary layer all play a key role in setting up favourable conditions for deep convection to grow from shallow convection (Zhang and Klein, 2010) and in this way, the boundary layer can exert its influence right up to the tropopause (Stewart, 1979).

A rather more dramatic way in which the boundary layer is relevant for weather phenomena is in the genesis and intensification of tropical cyclones. Although the precise mechanisms behind tropical cyclogenesis and subsequent intensification are fraught with controversy, all major theories acknowledge the importance of the boundary layer (Charney and Eliassen, 1964; Ooyama, 1969; Emanuel, 1991) and its crucial role is exemplified by the sensitivity of hurricane intensity and structure in models to the boundary-layer parameterisation (Montgomery and Smith, 2014).

1.3 INFLUENCE OF THE ABL ON CLIMATE

The ABL interacts with all physical components of the climate system: the atmosphere, the ocean and the land. On land, evapotranspiration is affected by the near-surface relative humidity and wind speed. A more humid environment makes it harder for plants to transpire and for moist soil to evaporate than a dry environment. Wind advects moisture away and helps maintain a moisture gradient between the soil or plant and the overlying air (Bonan, 2008).

In the ocean, the exchange of momentum, heat and water at the air-sea interface are important drivers of ocean circulation. The ocean receives kinetic energy from near-surface winds, whilst heat fluxes and evaporation at the air-sea interface modify the density of the surface waters, resulting in overturning (Barnier, 1998).

The distribution of boundary layer clouds modifies the planetary albedo, which is important for determining the Earth's climate sensitivity. In fact, one of the largest contributions to inter-model spread in climate sensitivity is due to uncertainties in feedbacks from marine boundary layer clouds (Bony et al., 2015). The prominent thinking is that as surface temperatures increase under climate change, the boundary layer deepens, resulting in more entrainment drying of the boundary layer. With the moisture supply cut back, low cloud cover reduces, which leads to further warming (Rieck et al., 2012). The rate of drying with increasing temperature depends on lower-tropospheric

mixing, including that incurred in the boundary layer (Sherwood et al., 2014). Due to the uncertainties inherent to convective and boundary-layer parameterisations, Global Climate Models (GCMs) inevitably vary in the strength of their lower-tropospheric mixing and thus in their climate sensitivity.

1.4 A WAY FORWARD

If parameterisations are failing to give a consistent picture of what turbulent mixing does, what can we do to see the picture more clearly? Or perhaps first and foremost: what does the picture look like? Intuitively we assume the picture is one of chaotic, disorganised motion and certainly there are some aspects of turbulence that comply with this view. But on the other hand, this disregards the fact that coherent structures are ubiquitous to turbulent flows. These structures interact with the more disorganised, smaller scales of turbulence and the details of that interaction can change under different environmental conditions. Understanding the implications of these interactions for turbulent mixing requires knowledge of the full range of turbulence scales. Observations covering a vast enough area at the required spatial resolution are scarce, if not absent altogether, though upcoming campaigns such as EUREC⁴A (Bony et al., 2017) and the Field Experiment on Submesoscale Spatio-Temporal Variability in Lindenberg (FESSTVaL) will begin to address this issue. As will be discussed in Chapter 2, Direct Numerical Simulation (DNS) already makes an understanding of scale interactions in the ABL possible, and supplements observations by affording us an accurate and detailed view of the turbulent exchange of heat, momentum and moisture that is vital for weather and climate-relevant processes, but is buried by complex models under a veil of parameterisation.

The ABL undergoes structural changes throughout the day and encompasses a variety of different regimes. A thorough investigation of them all is certainly beyond the scope of a single dissertation. Partly for that reason, we restrict ourselves here to the cloud-free, unstable regime, also known as the Convective Boundary Layer (CBL). A comprehensive overview of the neutral and stably-stratified boundary layer is given by Anson (2017). Whilst the cloud-topped boundary layer is arguably the more important regime in terms of its influence on climate (Mellado, 2017; Schulz, 2019), the cloud-free, unstable boundary layer presents a more tractable scenario that is still relevant for the cloudy regime, as it serves as both a precursor of shallow clouds as well as a reference case, which shapes our thinking about cloudy regimes.

MODELLING THE CONVECTIVE BOUNDARY LAYER

Even when a system is controlled by explicit laws of evolution, it often happens that its qualitative behavior is still not computable and predictable.

— Thom (1975)

The end result of a successful mathematical model may be an accurate method of prediction. Or it may be something quite different but not necessarily less valuable: *a new insight*.

— Hirsch (1984)

2.1 WHY USE DIRECT NUMERICAL SIMULATION?

Some of the errors in weather forecasts and biases in climate models are at least partly attributable to the simplifying assumptions made about the behaviour of the flow on scales smaller than the grid resolution. In some situations, these types of model are useful, or even necessary. But for studying certain sub-systems within the atmosphere and ocean, an accurate representation of a small number of processes can be a more valuable asset than representing a great number of processes poorly.

We are fortunate that we already have available to us what is probably the best possible model for fluid flow; very likely there is no simpler set of equations that can emulate the Navier–Stokes Equations. We are unfortunate that even for the simplest turbulent flows, those equations still present a formidable problem to which there is no known solution. For want of analytic solutions, many have turned to solving the equations numerically by means of DNS, though it is usually restricted to simple geometries and other idealisations, and still comes at a high computational cost. Despite these disadvantages, DNS also offers several rewards. We have measurement precision that is far beyond what can be achieved in laboratory experiments or out in the field. We have ideal conditions that we are completely in control of. But most of all, DNS provides us with a unique opportunity to see the mechanics of turbulence in a level of detail that is simply not possible by other means (Moin and Mahesh, 1998).

2.2 AN IDEALISED SYSTEM

Representing the CBL in a model could be a daunting task. Even in the case without clouds, the boundary layer is coupled to a heterogeneous surface with varying topography and roughness and is forced by differential heating that varies in time. Moreover, the full range of scales in the real ABL is on the order of 10^6 ; three-dimensional simulations on a grid containing 10^6 points in each direction is well beyond the capacity of modern computer simulations (Mellado et al., 2018). But are all of these complexities necessary to have a reasonable model of the CBL? Naturally, it depends on what one wants to achieve.

Whilst all of these aspects and more would be needed to reproduce atmospheric flow exactly, we are typically not interested in the precise trajectory of individual fluid parcels,

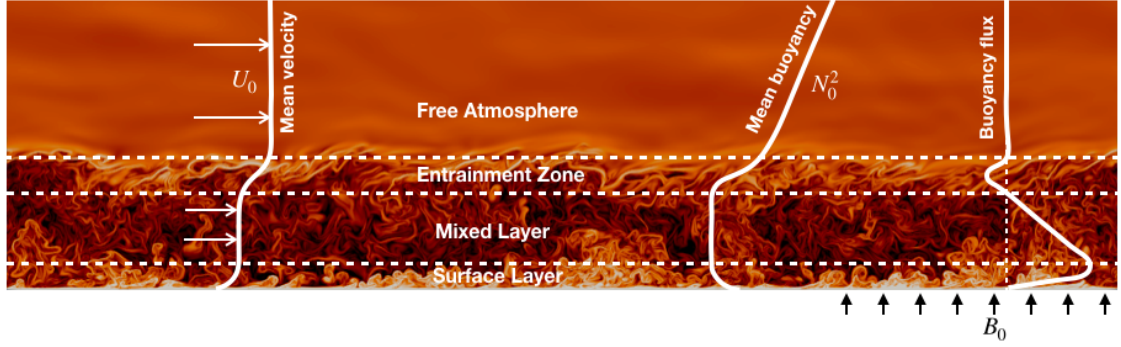


Figure 2.1: Snapshot from a direct numerical simulation of the sheared CBL showing the logarithm of the buoyancy gradient. Sketches of the mean velocity, mean buoyancy and buoyancy flux profiles are also shown. In the buoyancy flux profile, the dashed vertical line indicates the zero-line. A rough indication is given of where the surface layer, mixed layer, entrainment zone and free atmosphere are.

but rather in statistical properties of the flow. Mercifully, the requirements for obtaining realistic statistical profiles are far less stringent and we retain only those features that we believe are necessary to investigate the aspects we are interested in.

We solve the Navier–Stokes equations under the Boussinesq approximation:

$$\frac{\partial \mathbf{v}}{\partial t} + \nabla \cdot (\mathbf{v} \otimes \mathbf{v}) = -\nabla p + \nu \nabla^2 \mathbf{v} + b \mathbf{k}, \quad (2.1a)$$

$$\nabla \cdot \mathbf{v} = 0, \quad (2.1b)$$

$$\frac{\partial b}{\partial t} + \nabla \cdot (\mathbf{v} b) = \kappa \nabla^2 b, \quad (2.1c)$$

where $\mathbf{u}(\mathbf{x}, t)$ is the velocity vector with components (u, v, w) , $\mathbf{x} = (x, y, z)$ is the position vector with z as the vertical coordinate, t is time, $\mathbf{k} = (0, 0, 1)$ is the unit vector in the vertical direction and p is the modified pressure divided by a constant reference density. The buoyancy, b , is related to the virtual potential temperature, θ_v , via $b \approx g(\theta_v - \theta_{v,0})/\theta_{v,0}$, where $\theta_{v,0}$ is a constant reference value and g is the gravitational acceleration. The parameters ν and κ are the kinematic viscosity and the thermal diffusivity respectively.

We represent the CBL as an incompressible fluid developing over a flat, aerodynamically smooth surface that is forced by a constant and homogeneous surface buoyancy flux, B_0 (Fig. 2.1). The boundary layer grows into a free atmosphere characterised by a mean buoyancy gradient, N_0^2 . The sheared case can also be considered by initialising the simulation with a wind velocity, U_0 , that, for barotropic conditions, is constant with height in the free atmosphere. Over time, the CBL develops into a quasi-steady state, where the growth of the boundary layer is slow compared to the turnover time of boundary-layer scale circulations. Often, the structure of the CBL is regarded in terms of three main layers: the unstable surface layer, the well-mixed layer and the stably-stratified entrainment zone. This simple set-up is, perhaps surprisingly, sufficient to replicate typical midday to mid-afternoon conditions over land (Caughey, 1982).

2.3 DIMENSIONAL ANALYSIS

2.3.1 Control Parameters

One of the advantages of considering this idealised system is that all of the control parameters are known. For the shear-free CBL, there are four control parameters: $\{B_0, N_0, \nu, \kappa\}$. In the sheared CBL, there is one additional control parameter, U_0 . Through non-dimensionalisation, we can eliminate redundancy by reducing the number of control parameters to the minimum needed to fully characterise the system. Given n dimensional control parameters and m fundamental dimensions, the Buckingham Pi Theorem implies that $n - m$ non-dimensional parameters are sufficient to capture the dependence of the system on all n dimensional parameters (Buckingham, 1914). We have two fundamental dimensions: length and time. Hence, in the shear-free CBL, two non-dimensional parameters are sufficient, namely the Prandtl number,

$$Pr \equiv \frac{\nu}{\kappa}, \quad (2.2)$$

and the reference Reynolds number,

$$Re_0 \equiv \frac{B_0}{\nu N_0^2}, \quad (2.3)$$

whilst in the sheared CBL a third is required, namely the reference Froude number,

$$Fr_0 \equiv \frac{U_0}{N_0 L_0}, \quad (2.4)$$

where

$$L_0 \equiv \left(\frac{B_0}{N_0^3} \right)^{1/2} \quad (2.5)$$

is a reference Ozmidov length. The Ozmidov length,

$$L_{Oz} \equiv \left(\frac{\varepsilon}{N^3} \right)^{1/2}, \quad (2.6)$$

represents the largest scale at which overturning of eddies is uninhibited by the stratification (Dougherty, 1961; Ozmidov, 1965). In Eq. (2.6), ε is the viscous dissipation rate of TKE and $N = \partial_z \langle b \rangle$, with angled brackets denoting a horizontal average. The Prandtl number, Eq. (2.2), characterises how well momentum is diffused compared to heat and is a property of the working fluid. The reference Reynolds number, Eq. (2.3) is analogous to the buoyancy Reynolds number,

$$Re_b \equiv \frac{\varepsilon}{\nu N^2}, \quad (2.7)$$

which represents the scale separation between L_{Oz} and the Kolmogorov length, $\eta \equiv (\nu^3/\varepsilon)^{1/4}$, since $Re_b = (L_{Oz}/\eta)^{4/3}$. The Kolmogorov length is one of the smallest turbulence length scales, representing the scale at which TKE is dissipated into internal energy. The reference Froude number, Eq. (2.4), is a measure of the strength of wind shear as it compares the velocity in the free atmosphere with a velocity scale in the entrainment zone.

By considering typical values of the dimensional parameters in the CBL, we can see what parts of the non-dimensional parameter space the CBL occupies. At 15 °C, the kinematic viscosity of air is $1.47 \times 10^{-5} \text{ m}^2 \text{ s}^{-1}$ and the thermal diffusivity is $2 \times 10^{-5} \text{ m}^2 \text{ s}^{-1}$, yielding a Prandtl number of around one.¹ For typical midday conditions over land, one finds $B_0 \approx (0.1 - 1) \times 10^{-2} \text{ m}^2 \text{ s}^{-3}$, $N_0 \approx (0.6 - 1.8) \times 10^{-2} \text{ s}^{-1}$ and $U_0 \approx 0 - 20 \text{ m s}^{-1}$, yielding Re_0 on the order of $10^5 - 10^7$, $L_0 \approx 10 - 200 \text{ m}$ and Fr_0 in the range $0 - 85$.

As an example of the utility of non-dimensionalisation, consider one day where the free-tropospheric wind speed is $U_0 = 10 \text{ m s}^{-1}$, the buoyancy frequency is $N_0 = 10^{-2} \text{ s}^{-1}$ and the surface buoyancy flux is $B_0 = 2.5 \times 10^{-3} \text{ m}^2 \text{ s}^{-3}$ and another day where the free-tropospheric wind speed is $U_0 = 15 \text{ m s}^{-1}$, the buoyancy frequency is $N_0 = 0.75 \times 10^{-2} \text{ s}^{-1}$ and the surface buoyancy flux is $B_0 = 4.2 \times 10^{-3} \text{ m}^2 \text{ s}^{-3}$. One might assume that wind shear is stronger on the day with the higher wind speed, but in fact, both days correspond to the same shear condition as both days correspond to $Fr_0 = 20$. Only by performing the non-dimensional analysis can this insight be ascertained.

A key aspect of non-dimensionalisation is that flows with the same non-dimensional parameter values may be considered similar and comparable. Of the non-dimensional control parameters, Eq. (2.2-2.4), we can match all but one to typical atmospheric values. The one parameter we cannot match is the Reynolds number as this determines the range of scales present in the flow and hence the computing requirements to simulate that flow. We therefore simulate a flow with a much smaller Reynolds number than the real atmosphere. This, in combination with the idealised set-up, may cast doubt on the applicability of DNS results to the real atmosphere. Fortunately, sensitivity to the Reynolds number can be easily quantified and we already observe that for many important quantities, Reynolds number effects are small, indicating a tendency towards Reynolds number similarity (Garcia and Mellado, 2014; Mellado et al., 2017; Haghshenas and Mellado, 2019). Uncertainty associated with the idealisations we make necessitate comparisons to be made with other sources of inquiry such as Large Eddy Simulation (LES), laboratory experiments and field measurements, and here too there are promising signs of agreement across methodologies, despite the various uncertainties inherent to each approach (Mellado et al., 2018).

2.3.2 Independent Variables

Statistical properties in the CBL are functions not only of the non-dimensional control parameters, but also of some independent variables. Due to statistical homogeneity in the horizontal directions, the only independent variables on which statistics depend are height and time. These variables too can be non-dimensionalised, but in doing so, we have to make a choice about the appropriate length and time scales to normalise by. This depends on the specific problem one is addressing and in the following, we consider various options.

¹ The kinematic viscosity and thermal diffusivity of air depend slightly on temperature, but for the typical range of temperatures exhibited on Earth, they remain of order $10^{-5} \text{ m}^2 \text{ s}^{-1}$ and the Prandtl number remains approximately one.

2.3.2.1 Mixed-Layer Scales

The depth of the mixed layer in both the shear-free and sheared CBL is characterised by the encroachment length scale (Carson and Smith, 1975; Haghshenas and Mellado, 2019):

$$z_{\text{enc}} \equiv \left\{ 2N_0^{-2} \int_0^{z_\infty} [\langle b \rangle(z, t) - N_0^2 z] dz \right\}^{1/2}, \quad (2.8)$$

where z_∞ is located far enough into the free atmosphere for the integral to be approximately independent of z_∞ . Through an integral analysis of the buoyancy equation, Eq. (2.1c), one obtains

$$\frac{z_{\text{enc}}}{L_0} = [2N_0(1 + \text{Re}_0^{-1})(t - t_0)]^{1/2}, \quad (2.9)$$

with t_0 a constant of integration. Eq. (2.9) is an explicit expression for how the mixed layer depth evolves with time. The non-dimensional variables z/z_{enc} and z_{enc}/L_0 can replace the independent variables z and t .

Garcia and Mellado (2014) showed that beyond $z_{\text{enc}}/L_0 \approx 10$, the CBL is in a quasi-steady state and there is a dominant balance in the TKE budget equation between buoyancy production and viscous dissipation. In Section 4.3, in our discussion of the entrainment zone, we will concentrate on this quasi-steady state and consider how properties develop in the range $15 \leq z_{\text{enc}}/L_0 \leq 30$, i.e. over a time period in which the mixed-layer depth doubles. This could correspond, for example, to a CBL with $L_0 = 30$ m growing from 450 m to 900 m, or equivalently to a CBL with $L_0 = 50$ m growing from 750 m to 1500 m.

2.3.2.2 Diffusive Scales

In the surface layer, mixed-layer scales are inappropriately large and smaller scales are required for normalised properties to be of order one. Directly adjacent to an aerodynamically smooth surface lies the diffusive sublayer, where the molecular diffusion of heat is equally or more important than the turbulent flux. One can define diffusive length, velocity and buoyancy scales that give an appropriate measure of these properties in the diffusive sublayer (Townsend, 1959; Mellado, 2012):

$$z_\kappa = (\kappa^3/B_0)^{1/4}, \quad (2.10a)$$

$$w_\kappa = (\kappa B_0)^{1/4} = (z_\kappa B_0)^{1/3}, \quad (2.10b)$$

$$b_\kappa = (B_0^3/\kappa)^{1/4} = (B_0^2/z_\kappa)^{1/3}. \quad (2.10c)$$

The diffusive sublayer extends approximately up to $10z_\kappa$. The surface layer, which lies above the diffusive sublayer, has a depth that increases with the Reynolds number. For the Reynolds numbers considered in this work, the surface layer can be thought of as lying roughly between $10 \lesssim z/z_\kappa \lesssim 100$. The non-dimensional variables z/z_κ , w/w_κ and b/b_κ will be used extensively in Section 4.1 in our discussion of the surface layer.

In the case of an aerodynamically rough surface, analogous scales to those defined by Eq. (2.10) can be used simply by replacing the diffusive length with the roughness length, z_0 . Properties in the roughness sublayer differ from those in the diffusive sublayer, but beyond that, properties behave in a similar way regardless of whether the surface is smooth or rough, provided the Reynolds number is large enough (Raupach et al., 1991).

LARGE COHERENT STRUCTURES AND SMALL-SCALE TURBULENCE IN THE CONVECTIVE BOUNDARY LAYER

It is a great pity that of the three concepts of turbulence:

1. all eddies small compared to mean flow dimensions (Boussinesq "eddy viscosity" hypothesis, 1877);
2. some eddies large but weak (Townsend's hypothesis, 1956);
3. some eddies large and strong, interacting with smaller and weaker eddies (current view);

the most recent is both the most realistic and the most complicated.

— Bradshaw (1972)

In Section 1 we discussed that turbulence is not just an amalgamation of randomly moving vortices, but that coherent structures also emerge. In this section we elaborate on what these structures are, how they interact with small-scale turbulence in the CBL and what that interaction implies.

3.1 LARGE COHERENT STRUCTURES

Coherent structures in turbulent flows take many different forms, just as there are a variety of turbulent flows. For example, hairpin vortices and the somewhat unimaginatively named "very-large-scale motions" are features of wall-bounded flows (Kim and Adrian, 1999; Adrian, 2007; Balakumar and Adrian, 2007), large-scale vortices are found in both rotating flows and free shear flows (Koschmieder, 1979; Cantwell, 1981; Guervilly et al., 2014), whilst convective flows organise into circulation cells or rolls (Hartlep et al., 2003; Emran and Schumacher, 2015; Pandey et al., 2018).

Given the many different types of coherent structures, it is not easy to formulate a rigorous definition. They have been described as "organized spatial features which repeatedly appear [...] and undergo a characteristic temporal life cycle" (Berkooz et al., 1993), and also as "a distinct large-scale fluctuation pattern which is regularly observed in a given turbulent flow" (Wilczak, 1984). The recurring theme in these definitions is that of something which is organised in space and persistent in time.

Large-scale coherent structures change from flow to flow due to changes in the boundary conditions. In addition, these structures impose themselves on regions of the flow otherwise characterised by small-scale motion. Hence, any change to the coherent structures suggests that there may be an impact on the small-scale eddies embedded within them. This puts into question the traditional view that "the motion of the smaller eddies is related only weakly to the, possibly, inhomogeneous and anisotropic large eddies and their motion should be nearly isotropic" (Townsend, 1976). Indeed, the view of turbulence underwent a paradigm shift when it was recognised that large and small scales interact (Kline et al., 1967; Rao et al., 1971; Dimotakis and Brown, 1976; Cantwell,

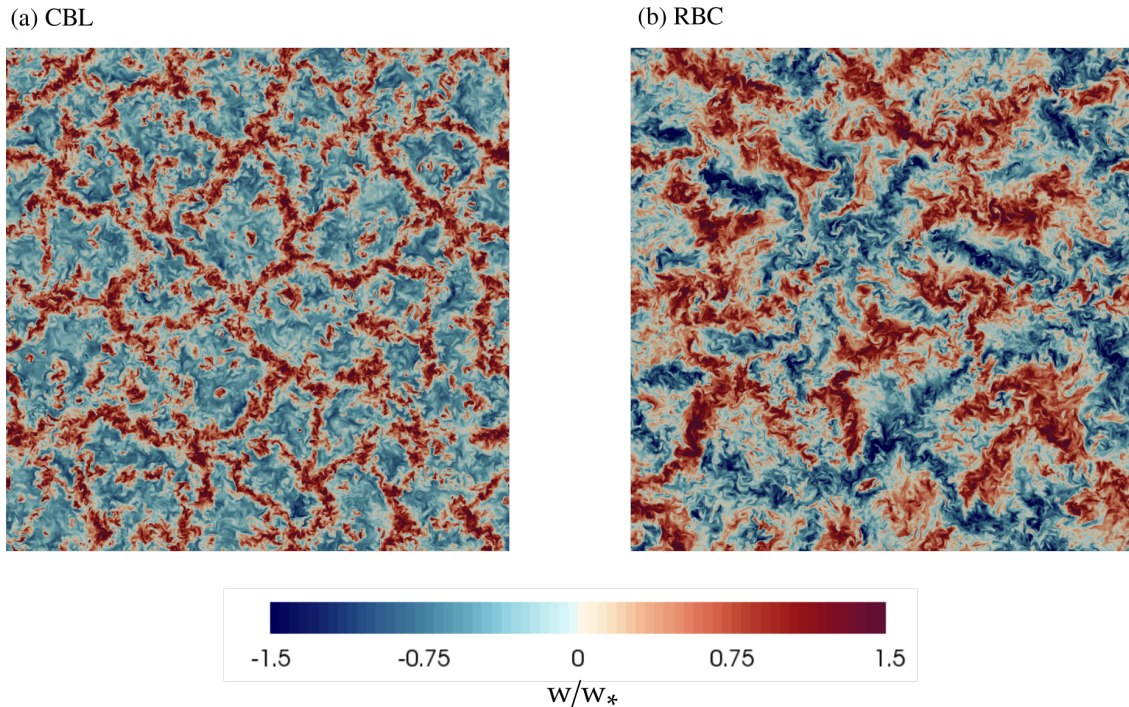


Figure 3.1: Horizontal cross-section of the vertical velocity field at the height of maximum vertical velocity variance, taken from direct numerical simulations of (a) the shear-free CBL and (b) Rayleigh–Bénard convection. The vertical velocity is normalised by the convective velocity scale, $w_* = (B_0 h)^{1/3}$, where h is the depth of the fluid layer.

1981) and the assumption of local isotropy of small-scales is often violated (Stewart, 1969; Warhaft, 2000).

Despite changes to the boundary conditions modifying the large scales, flows in nature often give rise to structures that bear a striking resemblance to those found in canonical flows in fluid mechanics. Examples that lend themselves to visualisation are cloud streets (Atkinson and Zhang, 1996), related to convection rolls, and solar granulation (Nordlund et al., 2009), related to cellular convection. Even when not made visible to the naked eye by the formation of clouds, circulation cells develop in the CBL that extend from the surface to the boundary-layer top and are several times the CBL depth in width (Mellado et al., 2016). These so-called Large-Scale Circulations (LSCs) are reminiscent of those occurring in classical Rayleigh–Bénard Convection (RBC) (Fig. 3.1). Consisting of a fluid layer heated from below and cooled from above, RBC stands as the simplest archetype of free convective flow. Despite its simplicity, the study of RBC has led to findings that have had far-reaching implications, with one of the most pertinent examples being the discovery of chaos by Lorenz (1963). The similarity of the coherent structures occurring in RBC and the CBL thus leads to the tempting speculation that results obtained from the former are applicable to the latter and can be transferred in a straightforward way. Still, the issue of changes to the large scales is problematic and the impact of this on the small scales of motion needs to be assessed.

3.2 SMALL-SCALE TURBULENCE

Small-scale turbulence occurs throughout the boundary layer, but only in some regions is it especially important for mixing. The details of the small scales matter in regions of

the flow where there are strong gradients, because the gradient determines the length scale over which properties vary rapidly and thus the scale of the mixing. In the CBL, the regions with the sharpest gradients are the surface layer and the entrainment zone (Fig. 2.1). Typically these regions are no more than a few hundred metres in depth and are thus small compared to the boundary layer as whole, which has a typical depth of one or two kilometres. To understand the implications of structures on the scale of the boundary layer depth (what we refer to as “large scale”) superimposed upon the flow in the surface layer and entrainment zone, it is necessary to review some fundamental concepts.

3.2.1 The Surface Layer

Perhaps harder to define than the boundary layer itself is the surface layer. Loosely, one can think of it as the bottom 10% of the boundary layer (Stull, 1988), but the essential point about the surface layer is that it scales in a very distinct way to the rest of the boundary layer. This means that surface-layer properties are of order one when normalised using the appropriate scales, whereas different scales are needed in other parts of the boundary layer for properties to be of order one there (cf. Section 2.3.2).

Compared to other regions of the boundary layer, the surface layer has probably enjoyed the most theoretical treatment, albeit a semi-empirical one. The theory known as Monin–Obukhov Similarity Theory (MOST) has been the cornerstone of investigations into the Atmospheric Surface Layer (ASL) since its emergence (Monin and Obukhov, 1954). The fundamental tenet of MOST is that the surface layer and the outer layer are decoupled and that surface-layer properties are determined exclusively by local parameters, namely the friction velocity, u_* , the surface buoyancy flux, B_0 , and the height above the ground, z . From these three parameters, one can form a non-dimensional “stability parameter”,

$$\frac{z}{L} = -\frac{zkB_0}{u_*^3}, \quad (3.1)$$

where $L = -u_*^3/(kB_0)$ is the Obukhov length and k is the von Kármán constant. The theory states that all surface-layer properties depend only on z/L , with the functional relationship needing to be obtained empirically. Observations have provided a proof of concept for boundary-layer regimes that are close to neutral, i.e. for small z/L (Wyngaard, 2010). Limiting cases on the other hand, where $z/L \rightarrow \pm\infty$, have proven to be more problematic (Högström, 1996).

In a state of free convection, such as the shear-free CBL, $z/L = -\infty$ and the friction velocity drops out of the scaling. In this case, the theory predicts specific scaling laws to hold: the variation with height of the n -th moment of velocity and buoyancy is derived to be $z^{\pm n/3}$ (positive sign applies to the velocity and negative sign to the buoyancy). Initially, measurements made in Kansas (Businger et al., 1971) and Minnesota (Kaimal et al., 1976) seemed to support these predictions, but since then, laboratory experiments and numerical simulations have repeatedly found deviations from the predicted scaling laws (Adrian, 1996; Khanna and Brasseur, 1997; Maronga and Reuder, 2017). These deviations are understood to stem from the existence of LSCs, that violate the assumption of no interaction with the outer layer (Mellado et al., 2016; Salesky and Anderson, 2018), yet the precise mechanism by which LSCs introduce non-local effects into the surface layer is still uncertain.

There are two main competing theories to explain the observed deviations from MOST. The first speculates that z and B_0 are insufficient to characterise surface-layer properties in free convection, and that a velocity scale associated with the large-scale horizontal flow near the surface is needed in addition. Businger (1973) supposed that this would be proportional to the convective velocity scale, w_* , which would effectively substitute for the friction velocity in the stability parameter. In this case, the theory again becomes empirical and dependence on the modified stability parameter needs to be determined through experiment. This idea seems to have been proposed in order to argue that the mean temperature gradient does not switch to a $-1/3$ power law in free convective conditions as predicted by MOST, but maintains the $(z/L)^{-1/2}$ scaling measured by Businger et al. (1971). However, more recent results have indicated that there is indeed a transition to the $-1/3$ scaling under strongly unstable conditions (Mellado et al., 2016; Maronga and Reuder, 2017), and as such the argument loses some of its grounding.

The second theory argues that the descending branches of the LSCs introduce non-local properties to the surface layer by transporting free-tropospheric air down to the surface - a theory which so far has mainly been supported by measurements of the specific humidity variance (de Bruin et al., 1993; Lohou et al., 2010; van de Boer et al., 2014). However, given that deviations from MOST have also been found for the temperature and vertical velocity variance (Adrian, 1996; Mellado et al., 2016; Maronga and Reuder, 2017), the possibility that large-scale downdrafts may also cause deviations from MOST in these quantities is still open.

3.2.2 The Entrainment Zone

Although there is no unique way to define the entrainment zone, a straightforward definition that we will use is the region of negative buoyancy flux (see Fig. 2.1). It is distinctive for being a region that is not entirely turbulent. Turbulence occurs where strong thermal plumes, associated with the ascending branch of the LSCs, penetrate into the overlying stratification, but these regions are surrounded by non-turbulent, free-tropospheric air being pulled into the boundary layer (Sullivan et al., 1998). The alternation of turbulent and non-turbulent patches is evident in the large-scale horizontal variation of the vorticity magnitude across the entrainment zone (Fig. 3.2), a phenomenon termed *external intermittency*.

The entrainment buoyancy flux that is responsible for the CBL growth is fundamentally affected by external intermittency. The turbulent area fraction varies sharply across the intermittent region and properties within turbulent and non-turbulent regions can differ strongly (Pope, 2000). The magnitude of the buoyancy flux in the entrainment zone is thus dictated by several factors: how large the turbulent area is, how strong the buoyancy flux is in the turbulent regions compared to the non-turbulent regions, and how much mean properties differ between the two regions.

The entrainment process is compounded not only by external intermittency, but also by wind shear. It has been well documented that wind shear generates a stronger entrainment buoyancy flux, which is commonly put down to the additional shear production of TKE (Pino et al., 2003; Conzemius and Fedorovich, 2006; Pino and Arrellano, 2006; Fedorovich and Conzemius, 2008). However, external intermittency implies that the situation could be more nuanced. With more TKE, wind shear may well simply generate stronger fluctuations in turbulent regions. But in addition, large-scale structures present in the flow are changed by wind shear from cells to rolls (see Salesky et al. (2017) and Fig. 3.2), which impacts the distribution of turbulent and non-turbulent patches.

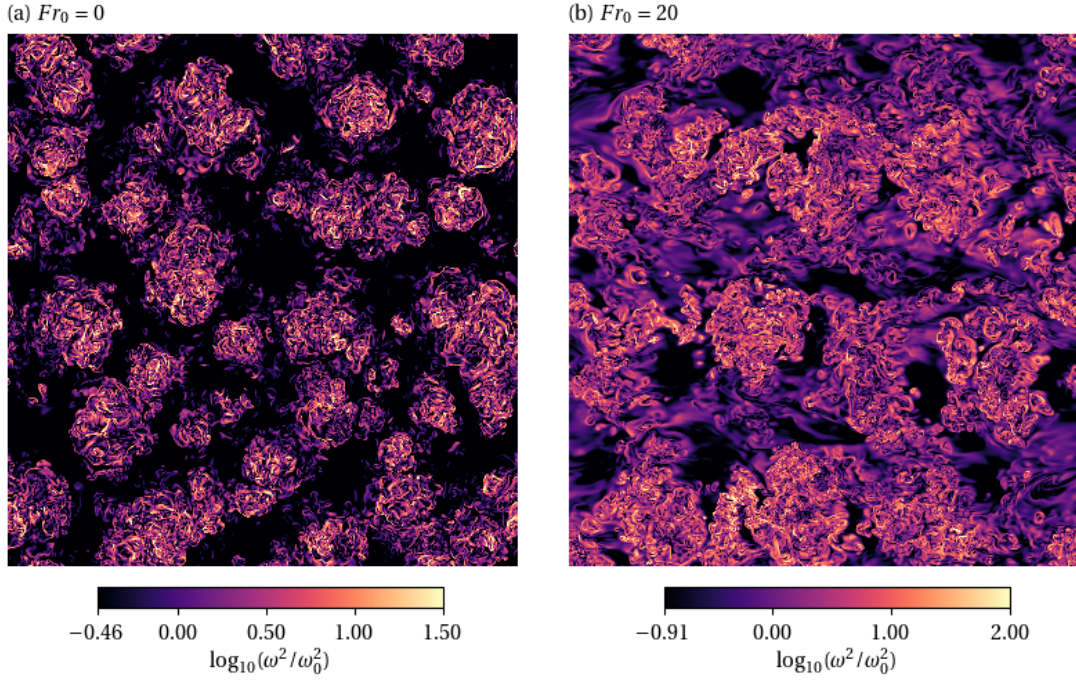


Figure 3.2: Horizontal cross-section of the enstrophy field at the height of minimum buoyancy flux, taken from a direct numerical simulation of (a) the shear-free CBL and (b) the sheared CBL at $Fr_0 = 20$. The enstrophy has been normalised by a reference enstrophy scale in the mixed layer, $\omega_0^2 = 0.1B_0/\nu$.

Moreover, wind shear has been shown to increase the amplitude of oscillations of the Turbulent/Non-Turbulent Interface (TNTI) (Kim et al., 2003), which suggests the difference in mean properties between the two regions may change. The interplay between these various wind-shear effects has yet to be disentangled.

3.3 RESEARCH QUESTIONS

We have seen that large coherent structures interact with small-scale turbulence in the CBL and this interaction challenges our understanding of the surface layer and of entrainment. From the previous discussion, the following questions arise:

Q1: Are deviations from Monin–Obukhov Similarity Theory in free convection caused by large-scale downdrafts impinging into the surface layer?

When conventional statistics are taken in the ASL, they average over both the updraft and downdraft regions of the LSCs. Updraft properties might be expected to comply with MOST, because we think of updrafts as being formed from buoyant thermals rising from the surface and merging together (Schmidt and Schumann, 1989). This suggests that updraft properties are characterised by a local length scale (the height above the ground) and the surface buoyancy flux, in agreement with MOST. Downdrafts, on the other hand, stem from the outer layer and due to covering a significant area near the surface, may be masking the behaviour inside large-scale updrafts regions when conventional statistics are taken.

Q2: Do more idealised flows with similar large coherent structures to the CBL have similar near-surface behaviour?

Rayleigh–Bénard convection shares many commonalities with the CBL, from the qualitative similarity of their large-scale structures, to more quantitative results, such as the same scaling of the Nusselt number with the Rayleigh number (Mellado et al., 2016). But RBC also offers many advantages over the CBL: it is symmetric, statistically steady and a simpler experimental set-up. It is perhaps the most well-studied form of free convection, for which many analytical results have been obtained (Chillà and Schumacher, 2012). If surface-layer properties in the two systems also scale similarly, this could rapidly advance our understanding of the unstable ASL.

However, differences in the boundary conditions between the two systems, namely the cooled upper plate of RBC and the stable stratification bounding the CBL, weaken the prospect of a straightforward transfer of results. To explore systematically how changes to the boundary conditions and the large-scale structures affect the near-surface region, it is useful to consider an intermediary case: Rayleigh–Bénard convection with an adiabatic top lid, which we shall refer to as the LID case. This case may be interpreted as a CBL capped by an infinitely strong inversion. The adiabatic upper plate prevents any heat from escaping and the fluid thus constantly warms over time, as in the CBL, but because the fluid depth does not change, many other properties do reach a statistically steady state. The inclusion of the LID case allows us to interpret more easily why differences occur and further assess to what extent idealised configurations are representative of the unstable ASL.

Q3: How do wind shear-induced changes to turbulent and non-turbulent regions in the entrainment zone contribute to shear-enhanced entrainment?

In a similar way to the surface layer, when conventional statistics are taken in the entrainment zone, they average over large-scale regions with potentially vastly different properties to each other, in this case, turbulent and non-turbulent regions. Changes in the boundary conditions, in this case the addition of wind shear, modify the large scales, which may in turn change the structure and properties of turbulent and non-turbulent regions. Hence, any analysis that fails to distinguish these regions from one another may be intermingling a number of different wind shear effects. This muddies our view and suggests we may not yet have fully explained the causes of shear-enhanced entrainment.

3.4 BEYOND CONVENTIONAL STATISTICS

The existence of large coherent structures in the CBL indicates that the use of conventional statistics is not always appropriate. The large-scale variation between updraft and downdraft regions, or between turbulent and non-turbulent regions, naturally calls for the use of conditional analysis (Dopazo, 1977; Antonia, 1981). This allows us to isolate the behaviour within different parts of the large-scale structure present in the flow.

Conditioning the CBL into updraft and downdraft regions is not a new idea. Aircraft observations were employed to this end by Young (1988) and Williams and Hacker (1992) and LES has also been a popular choice (Schumann and Moeng, 1991; Couvreur et al., 2010). However, for a thorough investigation into MOST and the surface layer, these methodologies pose problems. Flying an aircraft in the first few hundred metres above the ground for a sustained period of time is difficult, whilst LES suffers from the catch-22 that the theory one is trying to test the validity of is itself used in the simulation to provide boundary conditions. For this reason, DNS is becoming an ever more popular choice for investigations into the ASL, although the focus has largely been on stable

(Chung and Matheou, 2012; Ansorge and Mellado, 2014; Shah and Bou-Zeid, 2014) or mildly unstable conditions (McColl et al., 2017; Li et al., 2018), further motivating our consideration of the free convective case.

Conditioning statistics on either side of the TNTI using DNS has seen a wide variety of applications in canonical flows in fluid mechanics (Bisset et al., 2002; Mellado et al., 2009; van Reeuwijk and Holzner, 2014), unstratified penetrative convection (Holzner and van Reeuwijk, 2017) and gravity currents (van Reeuwijk et al., 2018). In terms of atmospheric flows, this kind of conditional analysis has proven very effective in direct numerical simulations of the stably-stratified Ekman layer (Ansorge and Mellado, 2016). The first efforts to measure the turbulent area fraction in the entrainment zone of the CBL were made by Deardorff et al. (1980) in their tank experiments. Our use of DNS in this setting enables the accurate detection of small-scale fluctuations in the enstrophy field needed for the partitioning into turbulent and non-turbulent regions.

SUMMARY OF RESULTS

We sometimes underestimate the influence of little things.

— Chesnutt (1999)

The questions posed in Section 3.3 are dealt with thoroughly in the Appendices; questions 1 and 2 in Appendix A and question 3 in Appendix B. In this section, we provide an overview of the main results.

4.1 DEVIATIONS FROM MONIN–OBUKHOV SIMILARITY THEORY IN FREE CONVECTION

In order to test the hypothesis that large-scale downdrafts cause deviations from MOST in free convection, we condition the flow into large-scale updraft and downdraft regions based on the sign of the low-pass filtered vertical velocity field. The filter size determines the definition of “large scale” and in Appendix A we consider two alternative choices based on characteristic length scales of the LSCs; a vertical scale and a horizontal scale. There it is shown that the response to our research question does not depend on the choice of filter size and so here we only consider the vertical length scale, namely the depth of the LSCs, as the filter size. We emphasise that the filtered vertical velocity field is only used to determine the location of large-scale updraft and downdraft regions, and the statistics themselves are obtained from the unfiltered, original DNS data.

By partitioning fields into large-scale updraft and downdraft regions, the mean of a dependent variable, ϕ , may be expressed as:

$$\langle \phi \rangle = a_u \langle \phi \rangle_u + a_d \langle \phi \rangle_d, \quad (4.1)$$

and the variance as:

$$\langle \phi'^2 \rangle = a_u \langle \phi'^2 \rangle_u + a_d \langle \phi'^2 \rangle_d + a_u a_d (\langle \phi \rangle_u - \langle \phi \rangle_d)^2, \quad (4.2)$$

where a_u is the updraft area fraction, $a_d = 1 - a_u$ is the remaining area fraction covered by downdrafts, $\langle \phi \rangle_u$ and $\langle \phi \rangle_d$ indicate the mean inside updrafts and downdrafts respectively, $\langle \phi'^2 \rangle_u = \langle \phi^2 \rangle_u - \langle \phi \rangle_u^2$ and $\langle \phi'^2 \rangle_d = \langle \phi^2 \rangle_d - \langle \phi \rangle_d^2$ indicate the variance inside updrafts and downdrafts respectively, and the final term on the right-hand side of Eq. (4.2) is the “mean difference term”.

Several conditional statistics from the shear-free CBL are shown in Fig. 4.1. Statistics have been averaged in time to improve statistical convergence and have been normalised by the scaling law predicted by MOST, such that if the profile is vertical, it indicates agreement with the MOST prediction. The first point to note is that the large-scale updraft area fraction varies by less than 5% with height within the surface layer (Fig. 4.1a). This indicates that any deviations from MOST that may occur are not due to variations with height of the updraft area fraction.

Previous studies have found that the mean buoyancy gradient follows the predicted scaling law of $(z/z_\kappa)^{-4/3}$ (Kader and Yaglom, 1990; Mellado et al., 2016; Maronga and

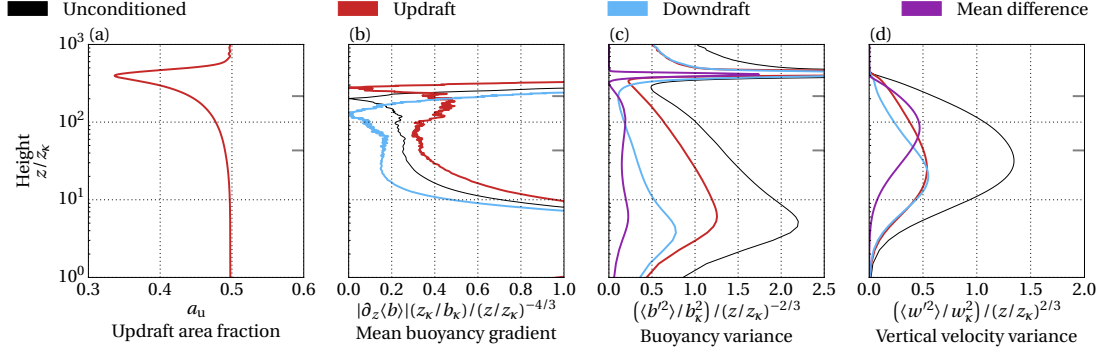


Figure 4.1: Conditional statistics in the shear-free CBL. For the buoyancy and vertical velocity variance, the updraft/downdraft area fractions are included, so that the sum of the coloured lines equals the unconditioned profile. The grey markers on the right-hand-side indicate (lower) 10% and (upper) 50% of the CBL depth.

Reuder, 2017). We find that this is true not only within updrafts between $40 \lesssim z/z_\kappa \lesssim 100$, but also within downdrafts between $20 \lesssim z/z_\kappa \lesssim 80$ (Fig. 4.1b).

Deviations from MOST occur in the buoyancy and vertical velocity variance profiles (Fig. 4.1c,d). Since the buoyancy variance profile leans to the left of a vertical line, this indicates that it decreases with height faster than predicted by MOST. This behaviour is maintained throughout the surface layer and right up to the centre of the CBL (shown by the upper grey marker on the right-hand-side of Fig. 4.1c). The vertical velocity variance on the other hand has a more complex behaviour. At around 10% of the CBL depth (shown by the lower grey marker on the right-hand-side of Fig. 4.1d), there is a stationary point, below which the vertical velocity variance increases with height faster than predicted by MOST (the profile leans to the right of a vertical line) and above which it increases more slowly with height than predicted by MOST (the profile leans to the left of a vertical line).

The behaviour of the buoyancy and vertical velocity variance cannot be explained by the mean difference term, which contributes the least to these properties in the surface layer. In accordance with our hypothesis, deviations from MOST do occur within large-scale downdraft regions. However, contrary to our hypothesis, strong deviations also occur within large-scale updraft regions and are at least as important as downdrafts, if not more so, for determining the near-surface behaviour. This suggests that even updraft properties are not just determined locally, but also by outer scales.

4.2 RAYLEIGH-BÉNARD CONVECTION AS A MODEL OF THE UNSTABLE ATMOSPHERIC SURFACE LAYER

In this section we consider the same properties as in Section 4.1, but now for the RBC and LID cases (Fig. 4.2). We note that although statistical profiles in RBC are symmetric in the vertical direction, this symmetry is not visible in Fig. 4.2a-d due to the logarithmic scale and normalisation by the scaling laws predicted by MOST.

The updraft area fraction in both the RBC and LID cases behaves in a similar way as in the CBL and is larger only by around 3% in the RBC case. Yet despite these similarities in the updraft area fraction, other conditional statistics in RBC differ from the CBL in several significant ways. All of these differences can be attributed to the colder, stronger downdrafts in RBC.

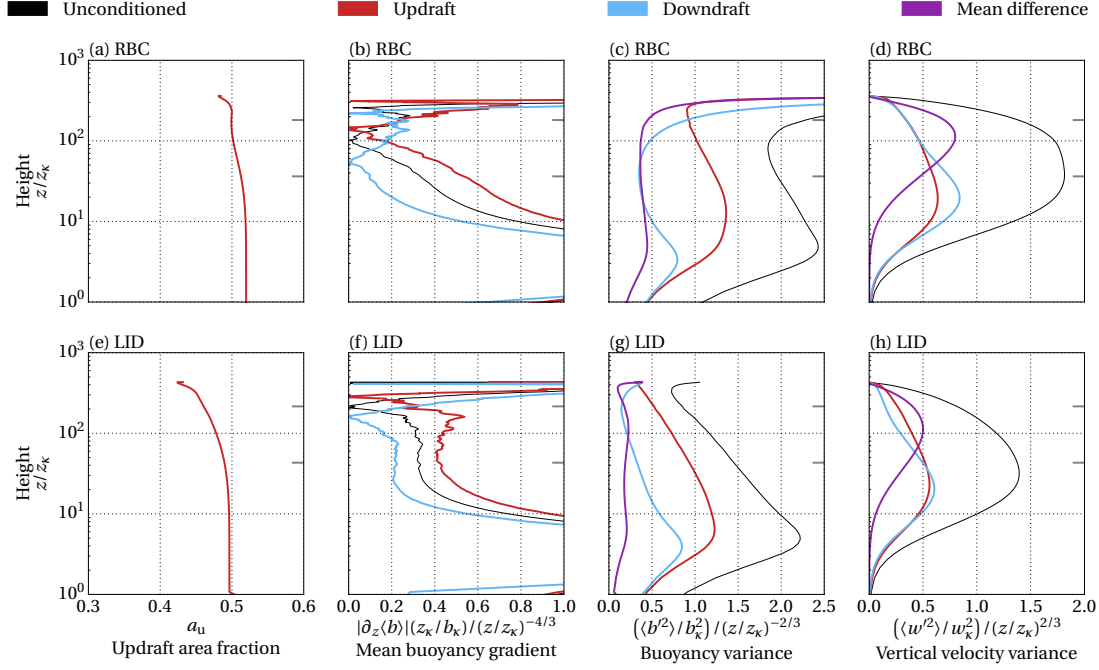


Figure 4.2: Same as Fig. 4.1 but for the RBC and LID cases. The grey markers on the right-hand-side indicate (lower) 10% and (upper) 50% of the depth of the domain.

The first main difference from the CBL is that the mean buoyancy gradient in RBC does not follow the scaling law predicted by MOST, neither in updraft nor in downdraft regions (Fig. 4.2b). This is because the colder descending plumes in RBC result in the air becoming well-mixed lower down in the cell compared to the CBL. Consequently, the mean buoyancy profile has less space to develop the expected scaling behaviour before its vertical gradient vanishes. However, at higher Reynolds number, where the surface layer is deeper compared to the receding diffusive sublayer, the mean buoyancy gradient may vanish higher up, and it is possible that the profiles in the RBC case then tend towards those found in the CBL.

A further way in which RBC differs from the CBL is in the behaviour of the buoyancy variance within large-scale downdraft regions. In the CBL, $\langle b^2 \rangle_d$ decays continuously with height in the surface layer faster than $z^{-2/3}$. In RBC however, $\langle b^2 \rangle_d$ begins to decrease markedly slower than $z^{-2/3}$ at a height of around 10% of the depth of the domain, as the profile starts to lean to the right of a vertical line in Fig. 4.2c. In the vicinity of the upper plate of RBC, cold tongues of air lead to a large buoyancy variance. The increasingly slow decay with height of $\langle b^2 \rangle_d$ near the surface indicates that the buoyancy variance within downdraft regions starts to be affected by this cold air descending from aloft. By contrast, the CBL has comparatively warm downdrafts and in the surface layer of the CBL, $\langle b^2 \rangle_d$ is primarily determined by a bottom-up contribution associated with small-scale thermals embedded within the large-scale downdraft region.

A final difference is that the vertical velocity variance within large-scale downdrafts is larger in RBC than in the CBL (Fig. 4.2d). This is due to the more vigorous downdraft plumes reaching the surface layer that generate stronger vertical velocity fluctuations.

Whilst the cold, strong downdrafts of RBC substantially change the behaviour of surface-layer properties compared to the CBL, it turns out that only a small modification to the RBC set-up is needed for statistical profiles in the surface layer to closely match

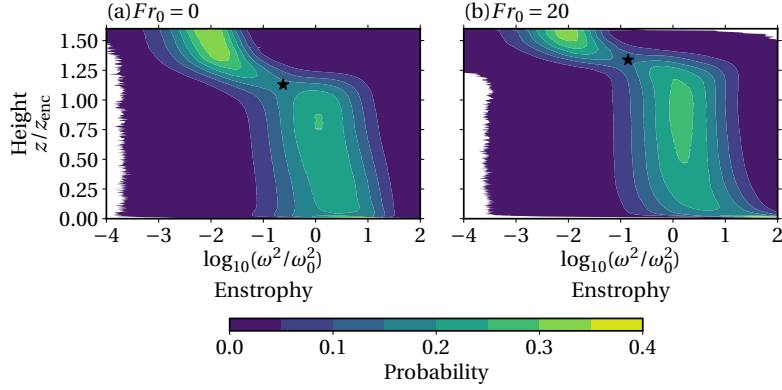


Figure 4.3: Probability density function of the enstrophy for (a) the shear-free CBL and (b) the sheared CBL at $Fr_0 = 20$. The black star indicates the approximate location of the saddle point and the threshold on enstrophy that we use to distinguish turbulent from non-turbulent regions.

those in the CBL. Instead of cooling the upper plate as in classical RBC, if the upper plate is made adiabatic, i.e. no heat is allowed to escape, the downdrafts are no longer as cold or as strong and their impact on the surface layer diminishes. This is evident in Fig. 4.2e-h, where the profiles in the LID case are almost indistinguishable from those in the CBL. Although the LID case is not as commonly studied as classical RBC, it still offers many of the same advantages, such as being a simpler experimental set-up than the CBL and most statistical properties, other than the mean temperature, having a statistically steady behaviour. This allows greater statistical convergence to be obtained through long-time averaging.

4.3 IMPLICATIONS OF EXTERNAL INTERMITTENCY FOR UNDERSTANDING SHEAR-ENHANCED ENTRAINMENT

Having seen how large coherent structures in the form of circulations affect the surface layer, we now turn our attention to the entrainment zone. Here, rising plumes associated with the ascending branch of the LSCs penetrate into the overlying stratification and spread outwards, creating a pattern of turbulent domes separated by regions of non-turbulent fluid as depicted in Fig. 3.2. Hence, instead of conditioning on the vertical velocity field, we now need to condition into turbulent and non-turbulent regions.

Doing so requires a definition of turbulence. One of the defining features of turbulence is that it is characterised by vorticity magnitudes which are orders of magnitude larger than those found in non-turbulent flow. In the CBL, this is apparent from the Probability Density Function (PDF) of the vorticity magnitude (also known as *enstrophy*) which has a dipole structure: one maximum in the PDF occurs within the free atmosphere at a certain enstrophy value and another maximum occurs in the boundary layer at an enstrophy value which, in our simulations, is two orders of magnitude larger than that occurring in the free atmosphere (Fig. 4.3). To define turbulent regions, we place a threshold on the enstrophy, which is chosen to be the saddle point in the enstrophy PDF, as it divides between enstrophy values more likely to be found in the boundary layer and enstrophy values more likely to be found outside of it.

With this, we can now decompose the buoyancy flux in the entrainment zone as follows:

$$\langle b'w' \rangle = a_T \langle b'w' \rangle_T + a_{NT} \langle b'w' \rangle_{NT} + a_T a_{NT} (\langle b \rangle_T - \langle b \rangle_{NT}) (\langle w \rangle_T - \langle w \rangle_{NT}), \quad (4.3)$$

where a_T and $a_{NT} = 1 - a_T$ are the turbulent and non-turbulent area fractions respectively, $\langle b'w' \rangle_T = \langle bw \rangle_T - \langle b \rangle_T \langle w \rangle_T$ is the buoyancy flux within turbulent regions, $\langle b'w' \rangle_{NT} = \langle bw \rangle_{NT} - \langle b \rangle_T \langle w \rangle_{NT}$ is the buoyancy flux within non-turbulent regions and $(\langle b \rangle_T - \langle b \rangle_{NT}) (\langle w \rangle_T - \langle w \rangle_{NT})$ is a contribution resulting from the difference in mean properties between turbulent and non-turbulent regions.

As discussed in Section 3.2, there are several plausible hypotheses for how wind shear may modify turbulent and non-turbulent regions in a way that increases the magnitude of the buoyancy flux in the entrainment zone. These hypotheses can be expressed with regard to the terms in Eq. (4.3):

1. Due to the larger amplitude oscillations of the TNTI, wind shear creates a larger difference in mean properties between turbulent and non-turbulent regions, increasing the term $(\langle b \rangle_T - \langle b \rangle_{NT}) (\langle w \rangle_T - \langle w \rangle_{NT})$.
2. Wind shear generates more vigorous fluctuations in turbulent regions, increasing the term $\langle b'w' \rangle_T$.
3. The large-scale structures in the CBL change when wind shear is added, which alters the distribution of turbulent patches in the entrainment zone and thereby a_T and a_{NT} .

By assessing the terms in Eq. (4.3) individually, we can test these different hypotheses.

To investigate wind shear effects, we consider two cases: a shear-free case, corresponding to $Fr_0 = 0$ (i.e. a free atmospheric wind speed of $U_0 = 0 \text{ m s}^{-1}$) and a sheared case corresponding to $Fr_0 = 20$ (i.e. a free atmospheric wind speed of $U_0 = 10 - 15 \text{ m s}^{-1}$ for typical midday conditions over land). In Fig. 4.4a, we show how each of the terms in Eq. (4.3) contribute to the total buoyancy flux for each Fr_0 . We see that the turbulent contribution is by far the largest to the total buoyancy flux and wind shear does little to modify the other two terms. We can therefore already eliminate the first hypothesis that wind shear increases the mean difference term and write:

$$\langle b'w' \rangle \approx a_T \langle b'w' \rangle_T. \quad (4.4)$$

To examine the second hypothesis, we show the entrainment flux ratio conditioned to turbulent regions as a function of the CBL state of development, z_{enc}/L_0 , in Fig. 4.4b. Surprisingly, the buoyancy flux in turbulent regions is not stronger at $Fr_0 = 20$, but is even weaker than in the shear-free case. This is unexpected as wind shear is well known to generate additional TKE in the entrainment zone, which ought to result in stronger turbulent fluctuations. Indeed, we find that at the height of minimum buoyancy flux, the buoyancy root-mean-square (r.m.s.) within turbulent regions at $Fr_0 = 20$ is around 50% larger than in the shear-free case (not shown). The reason that the entrainment flux ratio within turbulent regions does not show a corresponding increase is due to the effect of wind shear on the correlation between buoyancy and vertical velocity fluctuations. In the shear-free case, this correlation is high because vertical velocity fluctuations are induced by the buoyancy force acting in the same direction. When wind shear is added, buoyancy is no longer the only external source of vertical velocity fluctuations and the

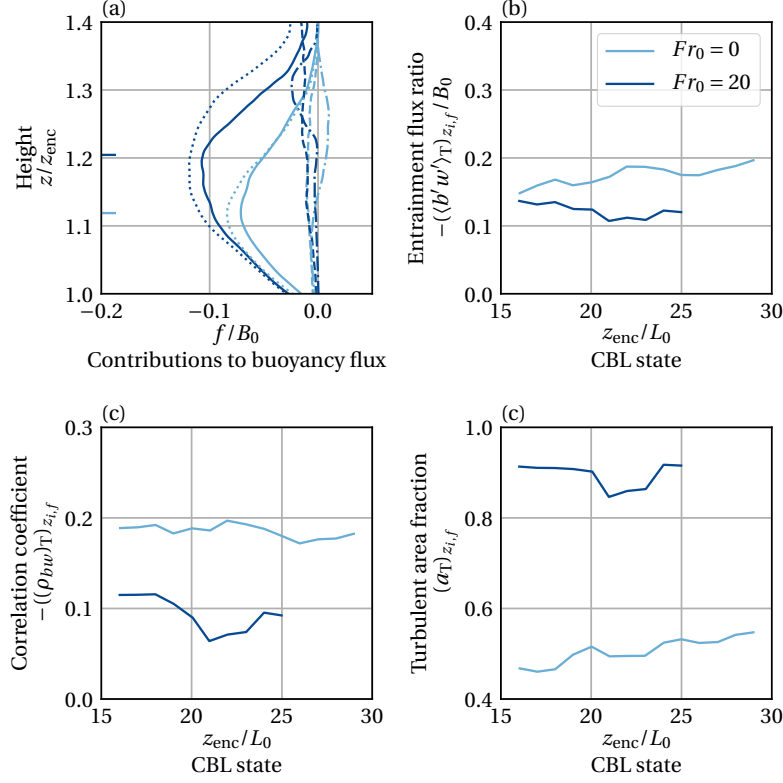


Figure 4.4: (a) Contributions to the total buoyancy flux. (Dotted) $f = \langle b'w' \rangle$, (solid) $f = a_T \langle b'w' \rangle_T$, (dashed) $f = a_{NT} \langle b'w' \rangle_{NT}$ and (dash-dotted) $f = a_T a_{NT} (\langle b \rangle_T - \langle b \rangle_{NT}) (\langle w \rangle_T - \langle w \rangle_{NT})$. The markers on the left-hand side indicate the height of minimum buoyancy flux, $z_{i,f}$. (b) Entrainment flux ratio conditioned to turbulent regions. (c) Correlation between buoyancy and vertical velocity fluctuations within turbulent regions at $z_{i,f}$. (d) Turbulent area fraction at $z_{i,f}$.

correlation consequently decreases (Fig. 4.4c). By expressing the buoyancy flux in terms of the correlation coefficient:

$$\langle b'w' \rangle_T = (\rho_{bw})_T (b_{rms})_T (w_{rms})_T, \quad (4.5)$$

it becomes clear that even though wind shear causes the buoyancy r.m.s. to become stronger in turbulent regions at $z_{i,f}$, the decrease in the correlation coefficient compensates, or even over-compensates that increase, such that buoyancy flux remains similar or weakens within turbulent regions under sheared conditions.

Our final and only remaining hypothesis relates to the effect of wind shear on the turbulent area fraction. By Eq. (4.4), given that $(\langle b'w' \rangle_T)_{z_{i,f}}$ is smaller in magnitude in the sheared case, the turbulent area fraction at $Fr_0 = 20$ must be substantially larger than at $Fr_0 = 0$. Qualitatively, the increase in the turbulent area fraction with wind shear is visible in Fig. 3.2, but in Fig. 4.4d, we quantify this and show that $(a_T)_{z_{i,f}}$ in the sheared case is around 70% larger than the shear-free value. Hence, the main reason that the entrainment flux increases with wind shear is because entrainment takes place more efficiently in turbulent regions than in non-turbulent regions and wind shear spreads turbulence over a wider area in the entrainment zone.

CONCLUSIONS AND OUTLOOK

But much of science concerns not prediction so much as understanding.

— Hirsch (1984)

The future for the study of the boundary layer promises to be rewarding and exciting - but not cheap!

— Stewart (1979)

5.1 RESPONSE TO RESEARCH QUESTIONS

We began by discussing how the ABL is a special and distinct region of the atmosphere that has consequences for both weather and climate, but that the necessity in low resolution models to parameterise boundary layer processes, amongst other phenomena, results in uncertainties that are difficult to quantify and interpret. We proposed DNS as a tool that allows one to study the ABL in a way that is free from assumptions about the underlying physics of turbulence and that affords us an opportunity to look at turbulence in unmatched detail.

We explained that coherent structures on the scale of the CBL depth (referred to here as “large scale”) influence small-scale eddies embedded within them. This interaction opens questions that challenge our existing understanding of the surface layer and entrainment zone. Our findings for the open questions we addressed may be summarised as follows:

Q1: Are deviations from Monin–Obukhov Similarity Theory in free convection caused by large-scale downdrafts impinging into the surface layer?

Although deviations from MOST do occur within large-scale downdraft regions, strong deviations also occur within large-scale updraft regions and these are at least as important, if not more so, for determining the near-surface behaviour. Hence, the cause of departures from MOST is not as straightforward as some have hypothesised.

Q2: Do more idealised flows with similar large coherent structures to the CBL have similar near-surface behaviour?

Surface-layer properties in RBC have several fundamental differences from the CBL. All of these can be attributed to the colder and stronger downdrafts that occur in RBC due to the large, positive buoyancy flux at the top of the fluid layer, as opposed to the small, negative buoyancy flux at the top of the CBL. However, only a small change to the classical RBC setup is required for surface-layer properties to behave in a similar way to the CBL. By substituting the cooled upper plate for an adiabatic one, the downdrafts are weaker and warmer, resulting in near-surface statistics that are almost indistinguishable from those in the CBL.

Q3: How do wind shear-induced changes to turbulent and non-turbulent regions in the entrainment zone contribute to shear-enhanced entrainment?

Turbulent regions contribute by far the most to the entrainment buoyancy flux, but wind shear does not cause the flux itself to become stronger within those regions. Rather, wind shear spreads turbulence over a larger area in the entrainment zone, thereby increasing the area in which entrainment takes place most efficiently.

5.2 LOOKING BACK AND AHEAD

In the process of answering questions, we uncover many more that remain to be answered. We conclude by discussing potential avenues of exploration that this work could lead to in the future.

Our findings from our first research question have eliminated one of the main hypotheses for how LSCs cause MOST to fail in free convection. Still, understanding the causes of deviations from MOST remains an open problem. One could consider continuing in the line of thought of Businger (1973) by investigating possible “wind shear” effects generated by the large-scale horizontal flow near the surface. The idea would be that these strong near-surface horizontal winds create an *internal boundary layer*, where turbulence is not buoyancy-driven, but shear-driven. Then, the predictions made by MOST for free convective conditions could be expected to apply in the buoyancy-driven regions (i.e. regions of strong vertical motion), but not in the shear-driven regions (i.e. regions of strong horizontal motion). By defining shear-driven regions based on where the magnitude of the large-scale horizontal velocity exceeds the magnitude of the large-scale vertical velocity, this hypothesis could be tested.

Another possible extension of our work on the surface layer is to consider the sheared CBL as well. Although there is no specific scaling law to test in this case, MOST predicts that surface-layer properties depend only on the stability parameter, z/L (Eq. 3.1). A number of studies have found that the near-surface region also depends on z_i/L , where z_i is the CBL depth (Panofsky et al., 1977; Khanna and Brasseur, 1997, 1998; Johansson et al., 2001). It has not yet been investigated whether other outer-layer parameters affect the near-surface region of the sheared CBL, such as the stratification in the free atmosphere, or the magnitude of the buoyancy flux at the CBL top. By adding wind shear to the LID case considered in this dissertation, we have a basis for comparison, as it can be thought of as a CBL with infinitely strong stratification and zero entrainment buoyancy flux.

With regards to the entrainment zone, our final result yielded a simple picture: fluxes at the CBL top are primarily controlled by the turbulent area fraction. This demonstrates the importance of taking the changing turbulence structure inside the entrainment zone into account and suggests a number of ways to take this idea forward. One possibility is to add further complexity to the system, for example with the addition of rotation. Preliminary work on this has indicated that the Coriolis force counteracts the shear enhancement of entrainment. Our work on the rotation-free CBL naturally suggests the following questions: How does rotation affect the large-scale structures present in the flow? Does it lead to a smaller turbulent area fraction in the entrainment zone that can explain the reduced entrainment flux? Answering these questions should be fairly straightforward, as we can perform the same kind of conditional analysis as we did to answer our third research question, but here applied to a shear-free and sheared CBL under rotation.

It would also be helpful to apply the conditioning into turbulent and non-turbulent regions to properties other than the buoyancy flux. In particular, temperature and humidity fluctuations caused by turbulent thermals in the entrainment zone generate supersaturation fluctuations that are important in the early stages of cumulus cloud

formation (Siebert and Shaw, 2017). Under what environmental conditions do these supersaturation fluctuations occur? Considering the temperature and moisture variance within turbulent regions in our idealised set-up can help to answer this question. Moreover, given that external intermittency has mainly been considered in cloud-free systems, it would be interesting to apply the conditioning method used here to the cloud-top region and learn how radiative transfer, phase changes and microphysical properties alter the entrainment process (Mellado, 2017). This would tie in well with the recent Azores stratoCumulus measurements Of Radiation, turbulEnce and aeroSols (ACORES) campaign, that obtained data at high spatial resolution within the entrainment interfacial layer of marine boundary layer clouds (Siebert et al., n.d.), and would allow us to further examine how well DNS compares to observations.

5.3 A FINAL REFLECTION

To quote Frisch and Orszag (1990): “Less is known about the fine scale of turbulence - for example, the scale of 1 mm in the atmosphere - than about the structure of atomic nuclei. Lack of basic knowledge about turbulence is holding back progress in fields as diverse as cosmology, meteorology, aeronautics and biomechanics”. Thirty years later and it stings a little to think that these words might still hold true. So have we made any progress since then?

The first part of the answer concerns the apparent difficulty of gaining information about the small scales of turbulence. Although we are still far away from simulating turbulent flows at the Reynolds numbers characteristic of the atmosphere, computing facilities have advanced enough that statistics obtained from direct numerical simulations show encouraging signs of convergence with increasing Reynolds number. This suggests, as succinctly put by Moin and Mahesh (1998), that “DNS need not obtain real-life Reynolds numbers to be useful in the study of real-life applications”. Thus, whilst we may not know for sure how the smallest scales of atmospheric motion behave, we have good reason to believe that it does not differ wildly from what our simulations show. Progress in high performance computing is giving us increasing confidence of this.

The second part of the answer concerns our fundamental understanding of turbulence. Testing existing theories and ideas, and seeking explanations and alternatives for when those theories and ideas fail, is essential for the progression of any science, but is especially needed in areas of science where theoretical ideas are few and far between. The application of this approach to turbulence is thus undoubtedly worthwhile and has formed the basis of this dissertation. Though the advancement of our understanding of turbulence may appear to be slow, advances are being made. It was a pleasure to be a part of that.

Part II

APPENDICES



ON THE ROLE OF LARGE-SCALE UPDRAFTS AND DOWNDRAFTS IN DEVIATIONS FROM MONIN–OBUKHOV SIMILARITY THEORY IN FREE CONVECTION

The work in this appendix has been published with minor modifications as:

Fodor, K., Mellado, J.P. & Wilczek, M. (2019). "On the Role of Large-Scale Updrafts and Downdrafts in Deviations From Monin–Obukhov Similarity Theory in Free Convection", *Boundary-Layer Meteorol.* 172, pp.371-396. <https://doi.org/10.1007/s10546-019-00454-3>

The contributions of the authors to this paper are as follows:

K. Fodor ran the simulations, performed the analysis and wrote the paper. JP. Mellado conceived the original idea for the work, helped set up the simulations, discussed the results, gave direction on how to proceed and reviewed the manuscript. M. Wilczek discussed the results and reviewed the manuscript.

On the Role of Large-Scale Updrafts and Downdrafts in Deviations From Monin–Obukhov Similarity Theory in Free Convection

Katherine Fodor¹, Juan Pedro Mellado¹ and Michael Wilczek²

¹Max Planck Institute for Meteorology, Bundesstraße 53, 20146 Hamburg, Germany

²Max Planck Institute for Dynamics and Self-Organization, Am Faßberg 17, 37077 Göttingen, Germany

Received: 14 November 2018 / Accepted: 29 April 2019 / Published online: 29 May 2019

We investigate by means of direct numerical simulation how large-scale circulations produce deviations from Monin–Obukhov similarity theory (MOST) in the limit of free convection, disentangling the role of large-scale downdrafts from updrafts using conditional analysis. We compare the convective boundary layer to two other free-convective flows: Rayleigh–Bénard convection with an adiabatic top lid and classical Rayleigh–Bénard convection. This serves a dual purpose: firstly, to ascertain how changes in the upper boundary conditions and thereby in the large-scale circulations modify the near-surface behaviour and secondly, to assess to what extent we can extrapolate results from idealized systems to the unstable atmospheric surface layer. Using a low-pass filter to define the large scales we find that, whilst deviations from MOST occur within large-scale downdraft regions, strong deviations also occur within large-scale updraft regions. The deviations within updrafts are independent of the filter length scale used to define the large-scale circulations, independent of whether updrafts are defined as ascending air, or as air that is both ascending and positively buoyant, and are not due to changes with height of the updraft area fraction. This suggests that even updraft properties are not just determined locally, but also by outer scales. Cold, strong downdrafts in classical Rayleigh–Bénard convection notably modify the near-surface behaviour compared to the other two systems. For the moderate Reynolds numbers considered, Rayleigh–Bénard convection with an adiabatic top lid thus seems more appropriate than classical Rayleigh–Bénard convection for studying the unstable atmospheric surface layer in the limit of free convection.

A.1 INTRODUCTION

Much of our understanding of the atmospheric surface layer (ASL) has its roots in Monin–Obukhov similarity theory (MOST), which assumes that all flow properties in the ASL depend only on the friction velocity, the surface buoyancy flux and the height above the ground (Monin and Obukhov, 1954). In the limit of free convection, the friction velocity goes to zero and the only remaining scaling parameters are height, z , and the surface buoyancy flux. Through dimensional analysis, MOST asserts that under free-convective conditions, the n^{th} -order moment of the velocity is proportional to $z^{n/3}$ whilst the n^{th} -order moment of the buoyancy is proportional to $z^{-n/3}$ (Prandtl, 1932; Priestley, 1954).

A key assumption in MOST is that surface-layer properties are determined locally, with no influence from the outer layer. On the whole, early work has provided empirical support for MOST under near-neutral (i.e. weakly stable or weakly unstable) conditions (Wyngaard et al., 1971; Kaimal et al., 1976). However, under strongly unstable and free-convective conditions, measurements of the root-mean-square (r.m.s.) of the buoyancy fluctuation indicate power laws with exponents in the range $[-0.5, -0.3]$ (Adrian, 1996; Mellado et al., 2016; Maronga and Reuder, 2017), whilst both a power law and a logarithmic law support measurements of the vertical velocity r.m.s. equally well (Adrian, 1996; Khanna and Brasseur, 1997; Mellado et al., 2016). These deviations from the predicted scaling laws are known to result from the interaction with large-scale circulations (LSCs), defined as persistent circulatory structures in the velocity field that extend across the whole boundary layer in convectively-driven systems (Chillà and Schumacher, 2012; Mellado et al., 2016; Salesky and Anderson, 2018). Still, there is conflict about the mechanisms by which LSCs introduce non-local effects to the surface layer.

One proposed mechanism involves wind shear induced by the LSCs that may alter scaling laws in the surface layer, since wind shear is not accounted for by MOST in free convection (Kraichnan, 1962; Businger et al., 1971; Businger, 1973). Another proposed mechanism is that large-scale downdrafts introduce non-local properties to the surface layer by transporting free-tropospheric air down to the surface (de Bruin et al., 1993; Lohou et al., 2010; van de Boer et al., 2014). The shear mechanism has been widely discussed, not only in the context of the atmospheric boundary layer (ABL), but also in studies of Rayleigh–Bénard convection, where it is supposed that LSCs induce the laminar boundary layer to become turbulent and thereby modify scaling laws near the surface at a sufficiently high Rayleigh number (van Reeuwijk et al., 2008; Shishkina et al., 2015; Puits and Willert, 2016). This possibility is an on-going source of debate and here we choose to focus on the downdraft mechanism, which has been less studied and where we are able to isolate the role of downdrafts using conditional analysis.

Since downdrafts occupy a significant area fraction near the surface, we hypothesize that when conventional statistics are taken, downdrafts mask the behaviour inside large-scale updraft regions, where, conversely, properties are postulated to follow the predicted scaling laws more closely. This hypothesis stems from an understanding of updrafts as being formed from buoyant thermals rising from the surface and merging together (Schmidt and Schumann, 1989; Mellado et al., 2016). From that point of view, it seems reasonable to suppose that updraft properties are characterized by a local length scale (the height above the ground) and the surface buoyancy flux, in agreement with MOST. A decomposition into large-scale updraft and downdraft regions thus has the potential to not only elucidate the mechanisms producing deviations from MOST, but also simplify scaling laws in the free-convective regime to a combination of the MOST

prediction, representing the updraft contribution, plus a scaling law for the downdraft contribution based on outer scales.

Using conditional analysis, differences between updraft and downdraft properties have previously been found in the bulk of the convective boundary layer (CBL - Young, 1988; Schumann and Moeng, 1991; Siebesma et al., 2007) and in the cloud layer (Siebesma and Cuijpers, 1995; Park et al., 2016). Here we extend this analysis into the surface layer by means of direct numerical simulation (DNS). Although restricted to moderate Reynolds numbers, DNS is an appropriate tool for investigations into the ABL, allowing detailed study of the full range of turbulence scales in relatively large-aspect-ratio domains, without the uncertainty associated with subgrid-scale modelling (Mellado et al., 2018). With the exception of Mellado et al. (2016), DNS studies of the ASL dealing explicitly with MOST have tended to focus on stable (Chung and Matheou, 2012; Ansorge and Mellado, 2014; Shah and Bou-Zeid, 2014) or mildly unstable (McColl et al., 2017; Li et al., 2018) conditions. This further motivates our consideration of the free-convective case.

One question that we also address is the extent to which classical Rayleigh–Bénard convection constitutes a good model of the CBL. Both configurations share commonalities. For example, the LSCs occurring in both systems closely resemble one another (Schmidt and Schumann, 1989) and the scaling of the Nusselt number with the Rayleigh number is the same in both systems (Mellado et al., 2016). These commonalities indicate a potential for results from Rayleigh–Bénard convection to be extrapolated to the ABL, but it is unclear how suitable Rayleigh–Bénard convection is for this purpose because differences in the upper boundary conditions between the two systems modify the LSCs, which in turn may affect surface-layer properties. To address this issue, we compare three configurations: the CBL, Rayleigh–Bénard convection with an adiabatic top lid (LID) and classical Rayleigh–Bénard convection (RBC). The LID case acts as an intermediary step between the warm entrainment zone of the CBL and the cooled upper plate of Rayleigh–Bénard convection (Sorbján, 1996) and allows us to systematically explore how changes in the upper boundary conditions and the large scales affect the near-surface region. We can also thereby assess to what extent idealized configurations such as the LID case, or the more commonly studied RBC case, are representative of the unstable ASL.

Although the CBL, LID and RBC cases have previously been compared in studies by Adrian et al. (1986) and Moeng and Rottuno (1990), only the former study addressed the validity of MOST and concentrated on the LID case in that context. By comparing the three systems using laboratory experiments and atmospheric measurements, Adrian et al. (1986) concluded that all three systems are similar in many respects in the lower half. Here, by using DNS to focus on the surface layer, we show that the LID case provides a better model of the CBL than does the RBC case.

This paper is structured as follows: in Sect. A.2, we detail the numerical procedure and provide a dimensional analysis of the problem that allows us to appropriately compare the three configurations. In Sect. A.3, we explain our conditioning methods, present results from the conditional analysis and consider how the results depend on our definition of “large scale”. Conclusions are given in Sect. A.4.

A.2 FORMULATION

A.2.1 Governing Equations

All three configurations considered are governed by the Navier–Stokes equations under the Boussinesq approximation,

$$\frac{\partial \mathbf{v}}{\partial t} + \nabla \cdot (\mathbf{v} \otimes \mathbf{v}) = -\nabla p + \nu \nabla^2 \mathbf{v} + b \mathbf{k}, \quad (\text{A.1a})$$

$$\nabla \cdot \mathbf{v} = 0, \quad (\text{A.1b})$$

$$\frac{\partial b}{\partial t} + \nabla \cdot (\mathbf{v} b) = \kappa \nabla^2 b, \quad (\text{A.1c})$$

$$\frac{\partial \chi}{\partial t} + \nabla \cdot (\mathbf{v} \chi) = \kappa \nabla^2 \chi, \quad (\text{A.1d})$$

where $\mathbf{v}(\mathbf{x}, t)$ is the velocity vector with components (u, v, w) , \mathbf{x} is the position vector with horizontal coordinates x and y , and vertical coordinate z , t is time and $\mathbf{k} = (0, 0, 1)$ is the unit vector in the vertical direction. The variable p is the pressure divided by a constant reference density and b is the buoyancy (which can be related to, e.g., the virtual potential temperature θ_v via $b = g(\theta_v - \theta_{v,0})/\theta_{v,0}$, where $\theta_{v,0}$ is a reference value and g is the acceleration due to gravity). The parameters ν and κ are the kinematic viscosity and the thermal diffusivity respectively.

The variable χ is a top-down scalar. This top-down scalar is a passive scalar that can be considered as a reference non-dimensional moisture field that, in combination with b , can be used to reconstruct several moisture statistics (Mellado et al., 2017). Here we use it to better interpret the behaviour within downdrafts, since χ has no forcing at the surface whereas b does.

A.2.2 Boundary Conditions

All simulations have periodic lateral boundary conditions and are statistically homogeneous in the horizontal directions. The surface is aerodynamically smooth. The boundary conditions at the surface are no penetration, no-slip on the velocity and Neumann on the scalars, such that a constant surface buoyancy flux is maintained,

$$F_{b,s} = -\kappa \left. \frac{\partial b}{\partial z} \right|_{z=0}, \quad (\text{A.2})$$

and a zero surface flux is maintained for the top-down scalar,

$$F_{\chi,s} = -\kappa \left. \frac{\partial \chi}{\partial z} \right|_{z=0} = 0. \quad (\text{A.3})$$

The three configurations differ in their upper boundary conditions, illustrated schematically in terms of some key properties in Fig. A.1 (symbols used are explained in Table A.1). In the CBL case, the initial buoyancy field increases linearly with height as $N^2 z$, where N is the buoyancy frequency in the free troposphere. The top-down scalar initially decreases with height as $-\gamma_\chi z$, where γ_χ is the lapse rate of χ in the free troposphere. The turbulent boundary layer that forms adjacent to the surface continuously penetrates into this linearly stratified fluid layer. At the top of the computational domain, which is placed far enough away such that it does not affect the turbulent boundary layer (see

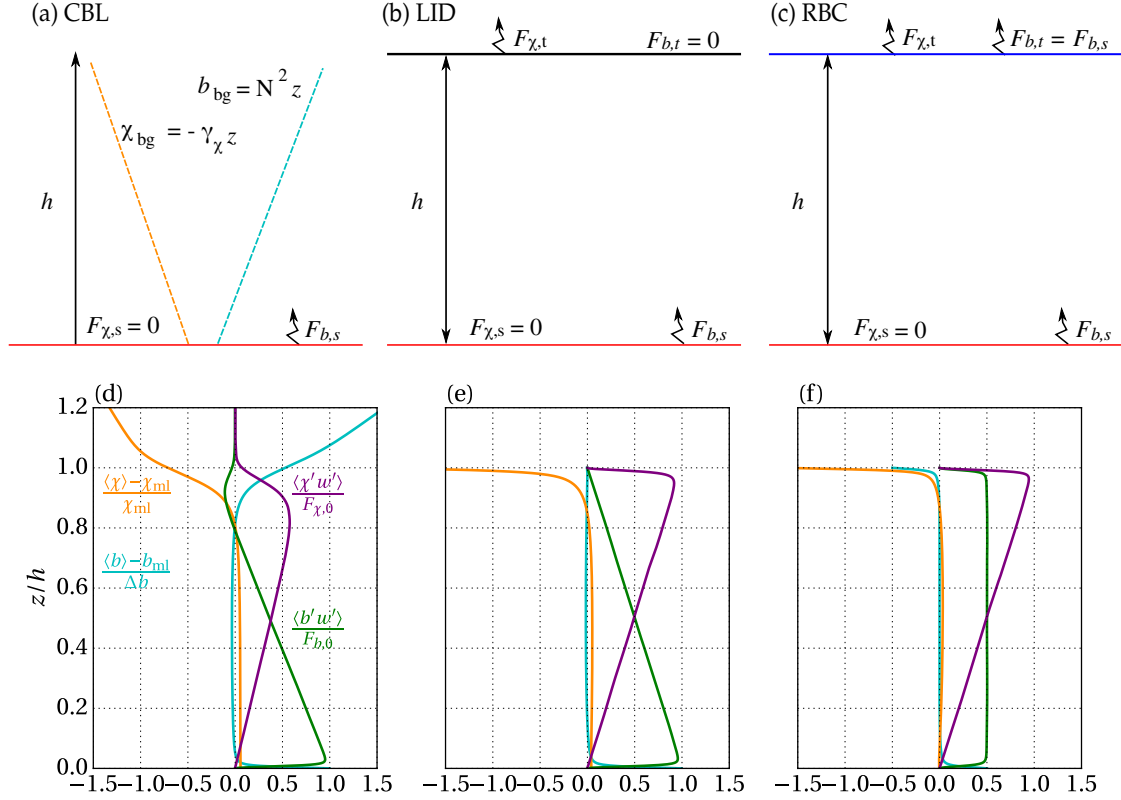


Figure A.1: (a)-(c) Schematics of the three free-convective systems. (d)-(f) Profiles of (cyan) the mean buoyancy, (orange) the mean top-down scalar, (green) the turbulent buoyancy flux, and (purple) the turbulent top-down scalar flux. Note that in the CBL case, only heights up to $1.2h$ are shown, but the full vertical domain extends up to $4.2h$. Symbols used in this figure are defined in Table A.1.

Garcia and Mellado (2014) for a sensitivity study), a Neumann boundary condition is applied on the scalars, maintaining a constant buoyancy flux, $F_{b,t} = -\kappa N^2$, and constant top-down scalar flux, $F_{\chi,t} = \kappa \gamma_{\chi}$. An impenetrable, free-slip condition is used for the velocity. The upper 25% of the computational domain contains a sponge layer, which relaxes all profiles back to their initial state, so as to prevent the reflection of gravity waves. After an initial phase of unsteady development, the CBL reaches a quasi-steady state in which the growth of the CBL is slow compared to the turnover time of the LSCs. For present purposes, we focus on this quasi-steady state.

In the LID case, the upper boundary condition on the velocity is no-penetration, no-slip and on the buoyancy, zero flux is maintained, rendering the top lid adiabatic. The top-down scalar has a constant flux at the upper plate. The LID case may be interpreted as a CBL with infinitely strong stratification. The adiabatic upper plate prevents any heat from escaping and the fluid thus constantly warms over time, but because the depth of the fluid layer does not change, many properties do reach a statistically steady state (Sorbjan, 1996).

In the RBC case, the same upper boundary conditions as in the LID case are used for the velocity and top-down scalar, but for the buoyancy, the flux at the upper plate is equal to that at the surface and the system is thus statistically steady for velocity and buoyancy properties.

It is worth commenting here on the role of the boundary conditions in determining the relative importance of the top-down and bottom-up contributions to the buoyancy

Table A.1: List of symbols used in Fig. A.1. The symbol ϕ refers to any scalar.

Symbol	Description
$F_{\phi,s}$	Flux of ϕ at the surface.
$F_{\phi,t}$	Flux of ϕ at the top of the computational domain (irrelevant for CBL).
$F_{\phi,0}$	Reference flux of ϕ . Eq. A.5 for b and Eq. A.6 for χ .
ϕ_{bg}	Background profile of ϕ in the free troposphere used as initial conditions (CBL only).
ϕ_{ml}	Mixed layer value of ϕ , defined as: $(h)^{-1} \int_0^h \langle \phi \rangle dz$.
$\Delta\phi$	Mean difference in ϕ across the convective region, defined by a positive buoyancy flux.
$\langle \phi \rangle$	Horizontal plane average of ϕ .
ϕ'	Fluctuation of ϕ from the horizontal plane average, defined as: $\phi - \langle \phi \rangle$.
h	Cell depth in the RBC and LID cases and boundary-layer depth in the CBL case, defined by the height of maximum mean buoyancy gradient.
N	Buoyancy frequency in the free troposphere (CBL only).
γ_χ	Lapse rate of χ in the free troposphere (CBL only).

field. In the RBC and CBL cases, the buoyancy is both bottom-up and top-down. In the RBC case, the bottom-up and top-down contributions are equal, since the surface flux equals the flux at the top plate. In the CBL case, the bottom-up contribution dominates as the magnitude of the entrainment flux is around 10% of the surface flux (Garcia and Mellado, 2014). In the LID case, the buoyancy is purely bottom-up, as the flux at the top plate is zero, and the LID case thereby acts as a limit in which the influence of downdrafts on the buoyancy near the surface is minimized.

A.2.3 Dimensional Analysis

In order to define reference scalar fluxes, we approximate the flux of a scalar ϕ , $F_\phi = \langle \phi'w' \rangle - \kappa \partial\phi/\partial z$, as varying linearly with height from the surface to $z = h$ (see Fig. A.1) and take the integral over this linear approximation

$$F_{\phi,0} \equiv \frac{2}{h} \int_0^h [(1 - z/h)F_{\phi,s} + (z/h)F_\phi|_{z=h}] dz. \quad (\text{A.4})$$

For the buoyancy, Eq. A.4 evaluates to

$$F_{b,0} \equiv \begin{cases} F_{b,s}, & \text{CBL,} \\ F_{b,s}, & \text{LID,} \\ 2F_{b,s}, & \text{RBC,} \end{cases} \quad (\text{A.5})$$

where in the CBL, we have neglected $F_b|_{z=h}$ since $-F_b|_{z=h}/F_{b,s} \approx 0.12$ (Garcia and Mellado, 2014). For the top-down scalar, Eq. A.4 evaluates to

$$F_{\chi,0} \equiv \begin{cases} (\gamma_\chi L_0)(L_0 N), & \text{CBL,} \\ F_{\chi,t}, & \text{LID,} \\ F_{\chi,t}, & \text{RBC,} \end{cases} \quad (\text{A.6})$$

(a) CBL



(b) LID



(c) RBC

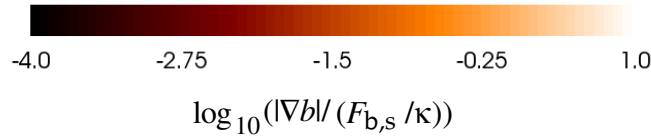
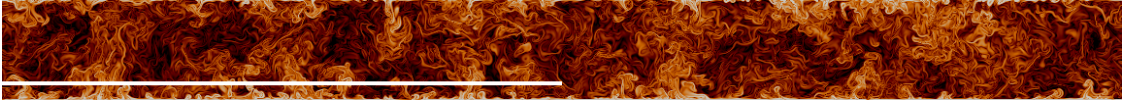


Figure A.2: Logarithm of the magnitude of the buoyancy gradient in each system. The *dashed white line* in panel (a) shows the depth of the CBL, h . The full width of the domain is shown, giving an aspect ratio of 11. The *solid horizontal white lines* show the LSC width as determined from the wavelength of the peak in the azimuthally integrated two-dimensional cospectrum between buoyancy and vertical velocity (see Table A.2).

where in the CBL, we have taken into account the entrainment flux of χ at the CBL top, which is estimated by the product of a passive scalar scale, $\gamma_\chi L_0$, and a velocity scale, $L_0 N$, where

$$L_0 \equiv (F_{b,s} / N^3)^{1/2} \quad (\text{A.7})$$

is the reference Ozmidov length that characterizes the thickness of the entrainment zone at the top of the CBL (Mellado et al., 2017). We note that the entrainment flux in the CBL is not a control parameter, but an outcome of the flow.

A.2.3.1 Convective Scales

Once the flow is fully turbulent and the details of the initial conditions have been sufficiently forgotten, statistical properties in the CBL case depend only on the control parameters $\{F_{b,0}, N, \nu, \kappa\}$ and the independent variables z and t , whilst in the non-penetrative RBC and LID cases, the control parameters are $\{F_{b,0}, h, \nu, \kappa\}$ and the independent variable is z . The outer length scale, h , is equal to the depth of the Rayleigh–Bénard cell and in the CBL it is a measure of the boundary-layer depth, which may be defined in numerous ways, though all are commensurate with one another (Garcia and Mellado, 2014). Here, we define the top of the CBL as the point of maximum mean buoyancy gradient away from the surface (see Fig A.2). Unlike the non-penetrative cases, where the depth of the cell is a control parameter, the CBL depth increases in time.

Each system has four control parameters and two fundamental dimensions; length and time. Dimensional analysis thus dictates that each system is governed by two non-

dimensional parameters: the Reynolds number (or the Rayleigh number) and the Prandtl number, $Pr = \nu/\kappa$. We fix Pr to be equal to one in all our simulations, leaving the Reynolds (or Rayleigh) number as the only non-dimensional control parameter.

The form of the Reynolds number depends on the choice of control parameters used for non-dimensionalization. By choosing $\{F_{b,0}, h\}$ in the LID and RBC cases, one finds the following convective Reynolds number, Re_* , and related convective Rayleigh number, Ra_* ,

$$Re_* = \frac{hw_*}{\nu} = \frac{(h^4 F_{b,0})^{1/3}}{\nu}, \quad (\text{A.8a})$$

$$Ra_* = \frac{h^4 F_{b,0}}{\nu\kappa^2} = Re_*^3 Pr^2, \quad (\text{A.8b})$$

where w_* in Eq. A.8a is an outer (or convective) velocity scale defined as (Deardorff, 1970a,b),

$$w_* = (hF_{b,0})^{1/3}. \quad (\text{A.9})$$

In the CBL case, by choosing $\{F_{b,0}, N\}$ to non-dimensionalize the system, one finds the reference Reynolds number, $Re_0 \equiv L_0(L_0N)/\nu = F_{b,0}/(\nu N^2)$, as a control parameter. In addition, the CBL case depends on the non-dimensional time variable Nt . The reference Reynolds number employs the length scale L_0 (Eq. A.7) and the velocity scale L_0N . The effect of Re_0 near the surface can be neglected as a first approximation once the CBL is in the quasi-steady regime considered here, as near-surface statistics only depend weakly on Re_0 (Mellado et al., 2016). Without loss of generality, the dependence on time can be expressed in terms of the dependence on Re_* (or Ra_*) defined in Eq. A.8 because the CBL depth, h , acts as a proxy time variable. Hence, the statistics of the three systems, CBL, LID and RBC, can be expressed solely as functions of Re_* (or Ra_*) and normalized height, z/h . We match Re_* in all three of our systems, such that $Re_* = 3258$ and $Ra_* = 3.5 \times 10^{10}$.

Using outer length and velocity scales allows us to define a convective turnover time, t_* ,

$$t_* = \frac{h}{w_*} = \left(\frac{h^2}{F_{b,0}} \right)^{1/3}. \quad (\text{A.10})$$

To remove the initial transient, we reject all data up to $h \approx 6.8L_0$ in the CBL case and up to $t \approx 12t_*$ in the non-penetrative cases. In order to improve statistical convergence, all statistics are then averaged over a period $t \approx 6t_*$ in the CBL case, and over $t \approx 16t_*$ in the non-penetrative cases. A shorter averaging time must be used in the CBL case so that Re_* does not change significantly as the CBL grows. The non-penetrative cases thus have the advantage that greater statistical convergence can be achieved through long time averaging.

A.2.3.2 Free-Fall Scales

If instead of $F_{b,0}$, one employs Δb , the mean buoyancy difference across the convective region (defined as the region of positive turbulent buoyancy flux), one finds the free-fall Reynolds and Rayleigh numbers,

$$Re_f = \frac{hw_f}{\nu} = \frac{(h^3 \Delta b)^{1/2}}{\nu}, \quad (\text{A.11a})$$

$$Ra_f = \frac{h^3 \Delta b}{\nu\kappa} = Re_f^2 Pr. \quad (\text{A.11b})$$

In Eq. A.11a, the free-fall velocity scale, w_f is

$$w_f = (h\Delta b)^{1/2}. \quad (\text{A.12})$$

Because we use a Neumann boundary condition on the buoyancy, Δb is not a control parameter and has to be obtained from the simulations, but within statistical convergence it is steady in the non-penetrative cases and quasi-steady in the CBL case. Mean values of Re_f and Ra_f are $\sim 10^4$ and 10^8 respectively in all simulations (see Table A.2). Employing h and w_f allows us to construct the free-fall time,

$$t_f = \frac{h}{w_f} = \left(\frac{h}{\Delta b} \right)^{1/2}. \quad (\text{A.13})$$

In terms of t_f , statistics are averaged over a period $t \approx 33t_f$ in the CBL case and over $t \approx 93t_f$ in the non-penetrative cases.

A.2.3.3 Diffusive Scales

Using the parameters $F_{b,s}$ and κ , one can define diffusive length, velocity and buoyancy scales as

$$z_\kappa = (\kappa^3 / F_{b,s})^{1/4}, \quad (\text{A.14a})$$

$$w_\kappa = (\kappa F_{b,s})^{1/4}, \quad (\text{A.14b})$$

$$b_\kappa = (F_{b,s}^3 / \kappa)^{1/4}. \quad (\text{A.14c})$$

Diffusive scales characterize the region of the boundary layer where the molecular diffusion of heat is equally or more important than the turbulent flux (Townsend, 1959). For flow over an aerodynamically smooth surface, this region is known as the diffusive layer and extends up to around $10z_\kappa$ (Mellado, 2012). Because we match Re_* in all three of our systems, given Eq. A.5, Eq. A.8a and Eq. A.14a, the scale separation in terms of the diffusive length scale, h/z_κ , is a factor of $2^{1/4}$ less in the RBC case than in the LID and CBL cases. However, in terms of the Kolmogorov length, $\eta = (v^3/\epsilon)^{1/4}$, where ϵ is the viscous dissipation rate of the turbulence kinetic energy (TKE), the scale separation, h/η , is similar in all three configurations.

The surface layer comprises both the diffusive layer and a region above in which MOST predicts distinct scaling laws to hold, though as discussed in Sect. A.1 the true scaling laws are uncertain. This region above the diffusive layer is the region of interest in this study, but a precise definition of its depth is elusive. Typically, the ASL depth is taken to be $0.1h$, which, for the Reynolds numbers considered here, is equivalent to $43z_\kappa$ in the LID and CBL cases and $36z_\kappa$ in the RBC case. However, an equally valid definition is the depth over which scaling laws hold. This is found to be of order 0.1 of the LSC width (Mellado et al., 2016), which is defined here as the wavelength of the maximum in the azimuthally integrated two-dimensional cospectrum between b and w . Consistent with Mellado et al. (2016) and Pandey et al. (2018), we find that λ_{LSC}/h is around twice as large in the RBC case compared to the CBL case (Fig. A.2 and Table A.2). Other plausible definitions of the LSC width, for example based on the peak in the vertical velocity spectrum, yield similar results (Mellado et al., 2016). Based on the magnitudes of λ_{LSC}/h given in Table A.2, the region of the ASL on which we focus is $10z_\kappa \lesssim z \lesssim 100z_\kappa$ in all cases.

Table A.2: Properties of the simulations considered in this study at $Re_* = 3258$ ($Ra_* = 3.5 \times 10^{10}$). The aspect ratio, Γ , is defined as the ratio between the width of the domain and h . The turbulent Reynolds number, Re_t , defined in Eq. A.15, is the maximum value. The free-fall Reynolds number, Re_f , defined in Eq. A.11a and the free-fall Rayleigh number, Ra_f , in Eq. A.11b, are temporal mean values. Column 6 shows the mean integral length over time, L_i , defined in Eq. A.17, and column 7 the LSC width, λ_{LSC} , defined as the wavelength of the peak in the azimuthally integrated two-dimensional cospectrum between buoyancy and vertical velocity.

Case	Grid	Γ	Re_t	Re_f	Ra_f	L_i/h	λ_{LSC}/h
CBL	$2560 \times 2560 \times 512$	11	1206	1.8×10^4	3.1×10^8	0.16	2.8
LID	$2560 \times 2560 \times 448$	11	4498	1.8×10^4	3.2×10^8	0.27	3.7
RBC	$2560 \times 2560 \times 448$	11	4349	1.9×10^4	3.7×10^8	0.33	5.6

A.2.4 Numerical Method, Resolution Requirements and Domain Size

The governing equations are discretized on a structured grid using sixth-order, spectral-like compact finite differences (Lele, 1992) and integrated in time using a low-storage, fourth-order Runge–Kutta scheme (Carpenter and Kennedy, 1994). The divergence-free condition, Eq. A.1b, is maintained by performing a Fourier decomposition of the Poisson equation for the pressure in the periodic, horizontal directions and factorizing the resulting set of equations in the vertical direction (Mellado and Anson, 2012). The grid is uniform and isotropic in most of the domain. Stretching is used to increase the vertical resolution near the walls in all cases, as well as to increase the domain depth in the CBL case.

The grid spacings are chosen according to previous studies of the resolution requirements for convection-driven flows (Shishkina et al., 2010; Mellado, 2012; Garcia and Mellado, 2014). The ratio of the vertical grid spacing, Δz , to the Kolmogorov length is $\Delta z/\eta \lesssim 1.5$ everywhere, which is sufficient for statistical properties of interest to depend less than 5% on the grid spacing. The vertical resolution near the walls in the non-penetrative RBC and LID cases is increased to $\Delta z/\eta \lesssim 0.9$ compared to $\Delta z/\eta \lesssim 1.1$ in the CBL case near the surface. This increase in resolution is necessary because the maximum value of the turbulent Reynolds number,

$$Re_t = \frac{e^2}{\epsilon \nu}, \quad (\text{A.15})$$

where e is the TKE, is reached near the upper wall in the LID case and near both walls in the RBC case and is at least three times larger in the non-penetrative cases than in the CBL case (see Table A.2). This is due to vigorous plume impingement and strong horizontal velocity fluctuations in the non-penetrative cases, resulting in greater TKE than in the CBL case where the large-scale horizontal motion is weaker (despite the convective Reynolds number being the same in the three systems).

The aspect ratio, Γ , defined as the ratio between the width of the domain and h , is equal to 11 in all three cases, which is at least twice as large as the typical LSC width (Table A.2). We verified that the domain size does not restrict the horizontal extent of the LSCs by performing simulations with a smaller aspect ratio of $\Gamma \approx 6.7$ and obtained similar results to the larger-aspect-ratio simulations (not shown).

A.3 CONDITIONAL ANALYSIS

In this section, we will look at how statistical properties of the flow behave within large-scale updraft and downdraft regions. In order to do this, a large-scale field first needs to be defined. The conditioned statistical properties we consider, however, come from the original DNS data and the large-scale field is simply used as an indicator of where the large-scale updraft and downdraft regions are located.

A.3.1 Defining a Large-Scale Field

We obtain a large-scale field by employing a low-pass Helmholtz filter in all three spatial dimensions. The Helmholtz filter is defined implicitly as (Foias et al., 2001),

$$(1 - \alpha^2 \nabla^2) \bar{\phi} = \phi, \quad (\text{A.16})$$

where $\alpha = \Delta/(2\pi)$, Δ is the filter size, $\phi(\mathbf{x}, t)$ is the unfiltered field and $\bar{\phi}(\mathbf{x}, t)$ is the filtered ('large-scale') field. Equation A.16 is solved by performing a Fourier decomposition in the periodic, horizontal directions to obtain a set of finite difference equations in the vertical direction. The boundary conditions are the same as those used in the simulation, in particular, the Helmholtz-filtered fields satisfy the no-slip condition. Being able to choose the boundary conditions that the large-scale field satisfies is a distinct advantage of the Helmholtz filter over more traditional spatial filters such as the box (or top-hat) filter, where each point is averaged over a volume specified by the filter size. Failing to satisfy the no-slip condition results in an unphysical increase in the large-scale TKE near the surface with the filter size (see Appendix A.A). For this reason, other, more conventional filters were rejected.

Of the many detection techniques we could have used to identify the LSCs, we favoured spatial filtering for the following reason. Other detection techniques, such as time averaging, proper orthogonal decomposition and Lagrangian techniques, critically rely on the choice of a finite time interval over which the structures are defined. This time scale should be on the order of, or less than, the decorrelation time to avoid averaging out the large-scale structures themselves. However, preliminary work using two-dimensional simulations revealed that the decorrelation time in the CBL case can vary by up to one order of magnitude depending on the initial time from which it is calculated, and this variability does not reduce with increasing aspect ratio. This makes the choice of time scale highly dependent on the time period considered. Hence, spatial filtering, which instead utilizes a length scale, is a convenient choice.

The filter size, Δ , determines the definition of "large scale" and here we consider two different characteristic length scales of the LSCs as candidates for Δ ; a vertical scale and a horizontal scale. For the vertical scale, we use h , which characterizes the depth of the LSCs and for the horizontal scale, we use the following integral length (Salesky et al., 2017),

$$L_i = \int_0^{l_0} \rho_w(s) ds, \quad (\text{A.17})$$

where $\rho_w(s)$ is the radial autocorrelation function of the vertical velocity field at its height of maximum variance and l_0 is the zero-crossing point of $\rho_w(s)$ (Fig. A.3a). The radial autocorrelation function at a given height is defined as

$$\rho_w(s) = \frac{\langle w(r, t) w(r + s, t) \rangle}{w_{\text{rms}}^2(t)}, \quad (\text{A.18})$$

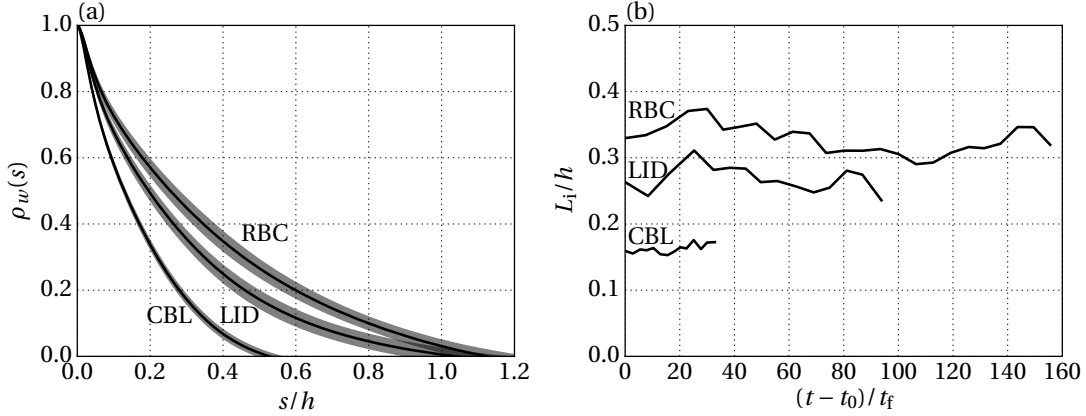


Figure A.3: (a) Radial autocorrelation function of the vertical velocity at its height of maximum variance. The *solid line* shows the time average and *shading* shows one standard deviation away from the mean. (b) Integral length, L_i , defined by Eq. A.17, as a function of time, where t_0 is the time at the beginning of the averaging period. In this figure, we have extended the RBC simulation to demonstrate that it is in a statistically steady state, but as stated in Sect. 2.3.2, all following statistics from the RBC case shown herein are averaged over a time period $t \approx 93t_f$.

where $r = \sqrt{x^2 + y^2}$ and the subscript rms indicates the root-mean-square. Since L_i is a measure of the horizontal distance over which vertical velocity fluctuations are correlated, it is a length scale characteristic of the large scales and naturally captures the greater horizontal extent of the LSCs found in Rayleigh–Bénard convection compared to the CBL (see Fig. A.3b). Moreover, L_i/h is steady in time (the standard deviation is less than 10% of the mean value in all cases), even in the CBL where h increases with time, so unlike the decorrelation time, L_i does not depend on the time period considered. This result corroborates Roode et al. (2004) for the CBL and Hardenberg et al. (2008) for Rayleigh–Bénard convection. The former study showed that a length scale based on the vertical velocity spectrum in the mid-CBL remains steady in time, whilst the latter study showed that for large enough aspect ratios and beyond the initial transient, the length scale of the large-scale structures in Rayleigh–Bénard convection is also steady in time. Mean values of L_i/h are shown in Table A.2 and indicate that L_i is 6 to 7% of the LSC width, λ_{LSC} , determined by the wavelength of the peak in the cospectrum between b and w .

In Table A.3, we show how the choice of filter length scale affects the proportion of TKE remaining in the large-scale field. Using L_i to define the large scales results in a slightly greater decrease of TKE in the RBC case than in the CBL case, and vice versa when using h . Either way, the partitioning of TKE between the systems is similar, despite the factor of two difference in horizontal scale between the CBL and RBC cases. For comparing the three configurations, it is thus irrelevant whether the LSCs are defined using their vertical scale or their horizontal scale. For a given configuration however, conditional statistics may well depend on the choice of filter length scale, and this is tested in Sect. A.3.7. For the sake of clarity of figures, we only utilize the h -filtered fields for the conditional analysis presented in Sect. A.3.3-A.3.6. The qualitative impact of spatial filtering with a filter size of h is shown in Fig. A.4 for reference.

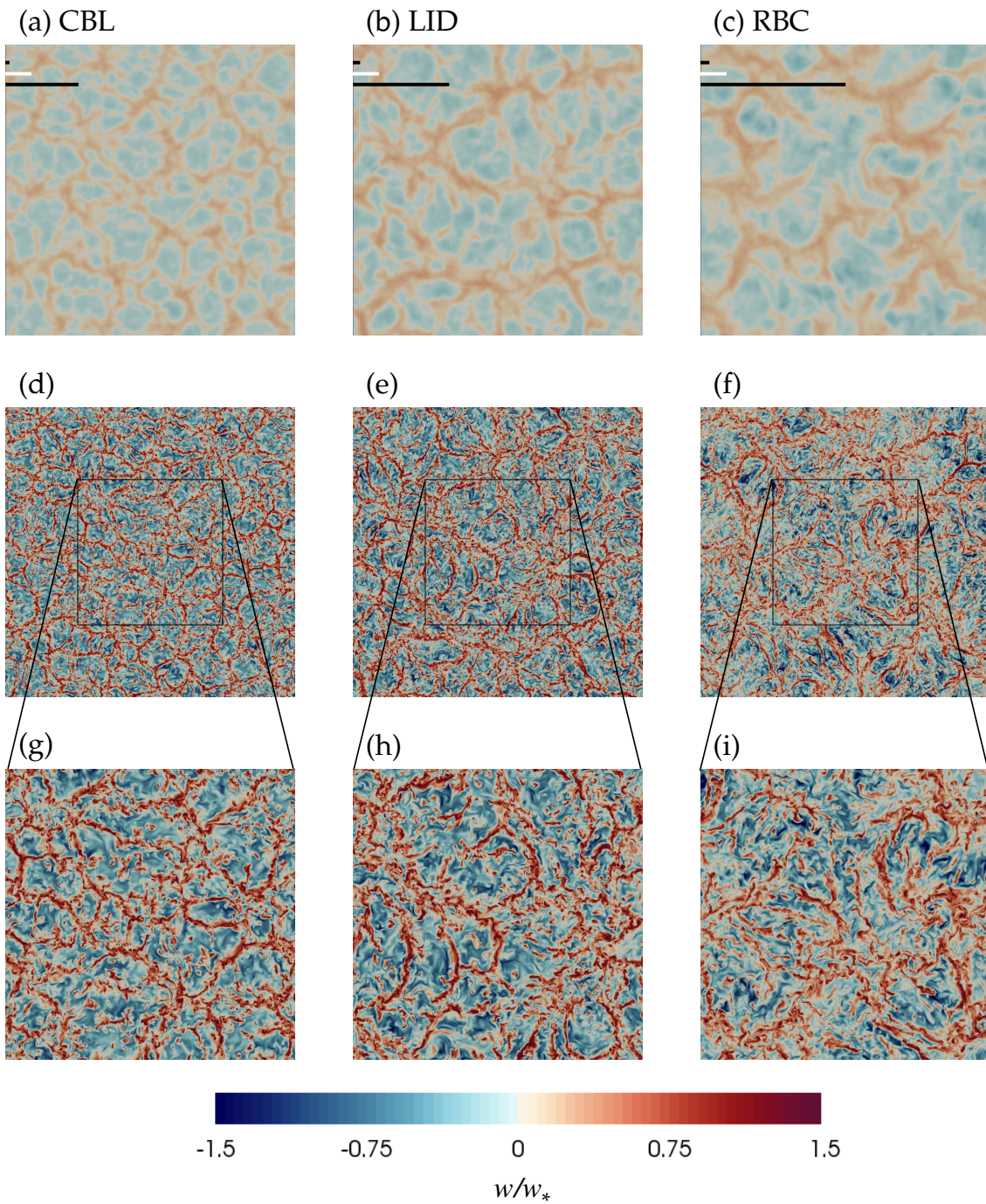


Figure A.4: (a)-(c) Horizontal cross-sections of the h -filtered vertical velocity field at $0.1h$. The *white horizontal line* shows the length of h , which is the same in all three cases. The *short black line* shows the integral length, L_i and the *long black line* shows the LSC width, λ_{LSC} . (d)-(f) Horizontal cross-sections of the unfiltered vertical velocity field at $0.1h$. (g)-(i) Zooms into the black boxes shown in panels (d)-(f).

Table A.3: Percentage of vertically integrated TKE remaining in the filtered flow, $\int_0^h \langle \bar{w}_i'^2 \rangle dz / \int_0^h \langle u_i'^2 \rangle dz$, depending on the filter size, Δ . The integral length, L_i , is defined in Eq. A.17.

Δ	TKE remaining (%)		
	CBL	LID	RBC
L_i	63	55	51
h	11	15	17

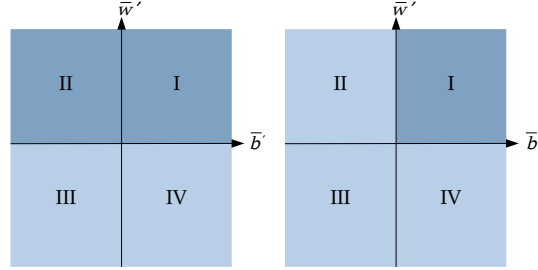


Figure A.5: Schematic of the two conditioning procedures used in this study. Out of the four quadrants, the domain is partitioned into two regions, as indicated by the colour shading. *Left*: Partitioning into updrafts (quadrants I and II) and downdrafts (quadrants III and IV). *Right*: Partitioning into buoyant updrafts (quadrant I) and anything outside of that region (quadrants II, III and IV).

A.3.2 Conditioning Criteria

We consider two different conditioning procedures. The first procedure conditions statistics from the original, unfiltered fields into large-scale updraft and downdraft regions based only on the sign of the large-scale vertical velocity field. For the second, we constrain our definition of updrafts to only large-scale buoyant updrafts, which have both positive vertical velocity and positive buoyancy fluctuation (see Fig. A.5). This second, bivariate approach aims to test how sensitive surface-layer properties are to the conditioning criteria. We emphasize that the filtered fields are only used to determine the location of large-scale updraft and downdraft regions. The statistics themselves are taken from the unfiltered fields.

By partitioning fields into two regions, the horizontal plane average of a dependent variable, ϕ , may be expressed as

$$\langle \phi \rangle = a_u \langle \phi \rangle_u + a_d \langle \phi \rangle_d, \quad (\text{A.19})$$

where a_u is the area fraction covered by updrafts, $a_d = 1 - a_u$ is the remaining area fraction covered by downdrafts, $\langle \phi \rangle_u$ is the mean inside updrafts and $\langle \phi \rangle_d$ is the mean inside downdrafts. Note that when we consider buoyant updrafts, where both $\bar{w}' > 0$ and $\bar{b}' > 0$, “downdraft” regions contain negatively buoyant, ascending air (quadrant II in Fig. A.5).

Using Eq. A.19 and the identity $\phi' = \phi - \langle \phi \rangle$, one can obtain the following expression for the variance,

$$\langle \phi'^2 \rangle = a_u \langle \phi'^2 \rangle_u + a_d \langle \phi'^2 \rangle_d + a_u a_d (\langle \phi \rangle_u - \langle \phi \rangle_d)^2, \quad (\text{A.20})$$

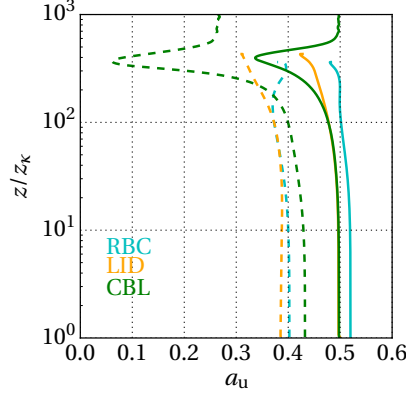


Figure A.6: Area fraction covered by (solid) updrafts ($\bar{w}' > 0$) and (dashed) buoyant updrafts ($\bar{w}' > 0, \bar{b}' > 0$).

where $\langle \phi'^2 \rangle_u = \langle \phi^2 \rangle_u - \langle \phi \rangle_u^2$ and $\langle \phi'^2 \rangle_d = \langle \phi^2 \rangle_d - \langle \phi \rangle_d^2$. The respective terms on the right-hand side of Eq. A.20 are contributions from the variance within updrafts, the variance within downdrafts and the squared difference between the mean inside updrafts and the mean inside downdrafts, hereafter referred to as the “mean difference term”. We will consider the relative contribution of each of the three terms on the right-hand side of Eq. A.20 to the buoyancy and vertical velocity variance. The contribution from downdrafts or the mean difference term should be large if downdrafts are to explain the significant deviations from MOST found in previous studies.

A.3.3 Area Fraction

Before we proceed directly onto the conditional analysis, it is first important to consider the updraft area fraction, as strong variations of a_u with height could by itself partly explain deviations from MOST. Previous studies considering the updraft area fraction profile have shown that it approaches 0.5 near the surface, but did not have sufficient data to analyze the near-surface behaviour in detail (Young, 1988; Schumann and Moeng, 1991; Sorbjan, 1996).

As shown in Fig. A.6, the updraft area fraction behaves in a similar way in the surface layer across all three systems; a_u only varies by $\sim 3\%$ in the interval $10z_\kappa \lesssim z \lesssim 100z_\kappa$, regardless of the conditioning criteria. When using the more restrictive buoyant updraft definition, a_u is simply smaller by $\sim 10\%$. Therefore, the variation of a_u with height has a negligible effect on the behaviour of updraft and downdraft properties in the surface layer.

A.3.4 Buoyancy Statistics

The first property we consider is the mean buoyancy gradient. Several studies agree that the mean buoyancy is consistent with MOST for sufficiently unstable conditions (Kader and Yaglom, 1990; Mellado et al., 2016; Maronga and Reuder, 2017). In Fig. A.7, we show the magnitude of the mean buoyancy gradient normalized by $(z/z_\kappa)^{-4/3}$, the free-convective scaling given by MOST, such that if this scaling law is satisfied in the surface layer, profiles will be constant in the vertical.

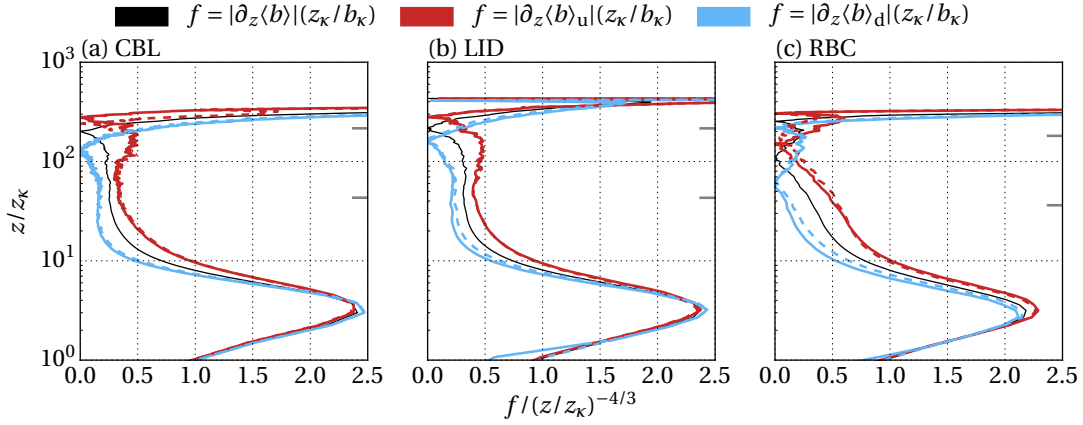


Figure A.7: Magnitude of the mean buoyancy gradient normalized by free-convective scaling. *Thick solid lines* indicate conditioning based only on \bar{w}' and *thick dashed lines* based on both \bar{w}' and \bar{b}' . *Grey ticks* on the right-hand side indicate $0.1h$ and $0.5h$.

We find that the mean buoyancy gradient follows free-convective scaling not only within updrafts, but also within downdrafts in the LID and CBL cases. For updrafts, this is in the range $40z_\kappa \lesssim z \lesssim 100z_\kappa$ and for downdrafts between $20z_\kappa \lesssim z \lesssim 80z_\kappa$. We also find that the magnitude of the mean buoyancy gradient in downdrafts is $\sim 50\%$ of that in updrafts, demonstrating that updrafts primarily determine the mean buoyancy gradient near the surface, but downdrafts make a non-negligible contribution. Moreover, these results do not depend on whether conditioning is based on the vertical velocity only, or on both the vertical velocity and the buoyancy.

In contrast to the LID and CBL cases, the mean buoyancy gradient does not follow free-convective scaling in either updrafts or downdrafts in the RBC case for the Reynolds numbers (equivalently Rayleigh numbers) that we reach in our simulations. The discrepancy of the mean buoyancy with the MOST prediction in the RBC case is in agreement with Pirozolli et al. (2017). We attribute this to a difference in the large-scale downdraft regions between the systems. In the RBC case, cold air descending from the upper plate results in the air becoming well-mixed lower down in the cell compared to the LID and CBL cases, where there is no forcing from above. Consequently, the mean buoyancy profile has less space to develop before its vertical gradient vanishes. This interpretation is supported in Fig. A.7, where the minimum in the buoyancy gradient occurs lower down in the RBC case compared to the other two systems, both in updrafts and in downdrafts.

Our results for the mean buoyancy already give one indication of how changes in the upper boundary condition can be felt near the surface. Although replacing a linearly stratified atmosphere with an impenetrable, adiabatic lid appears to hardly affect $\langle b \rangle$ in the surface layer, if downdrafts are comparatively cold, as in the RBC case, the behaviour of $\langle b \rangle$ is greatly modified. However, at higher Reynolds number, where the surface layer is deeper compared to the receding diffusive layer, the mean buoyancy gradient may vanish higher up, and it is possible that the profiles in the RBC case may tend towards those found in the LID and CBL cases.

Considering now the buoyancy variance, we first analyze the mean difference term in Eq. A.20. Given that both $\langle b \rangle_u$ and $\langle b \rangle_d$ are of the form $c_1(z/z_\kappa)^{-1/3} + c_2$ in the LID and CBL cases, where c_1 and c_2 are empirical constants obtained from the mean buoyancy

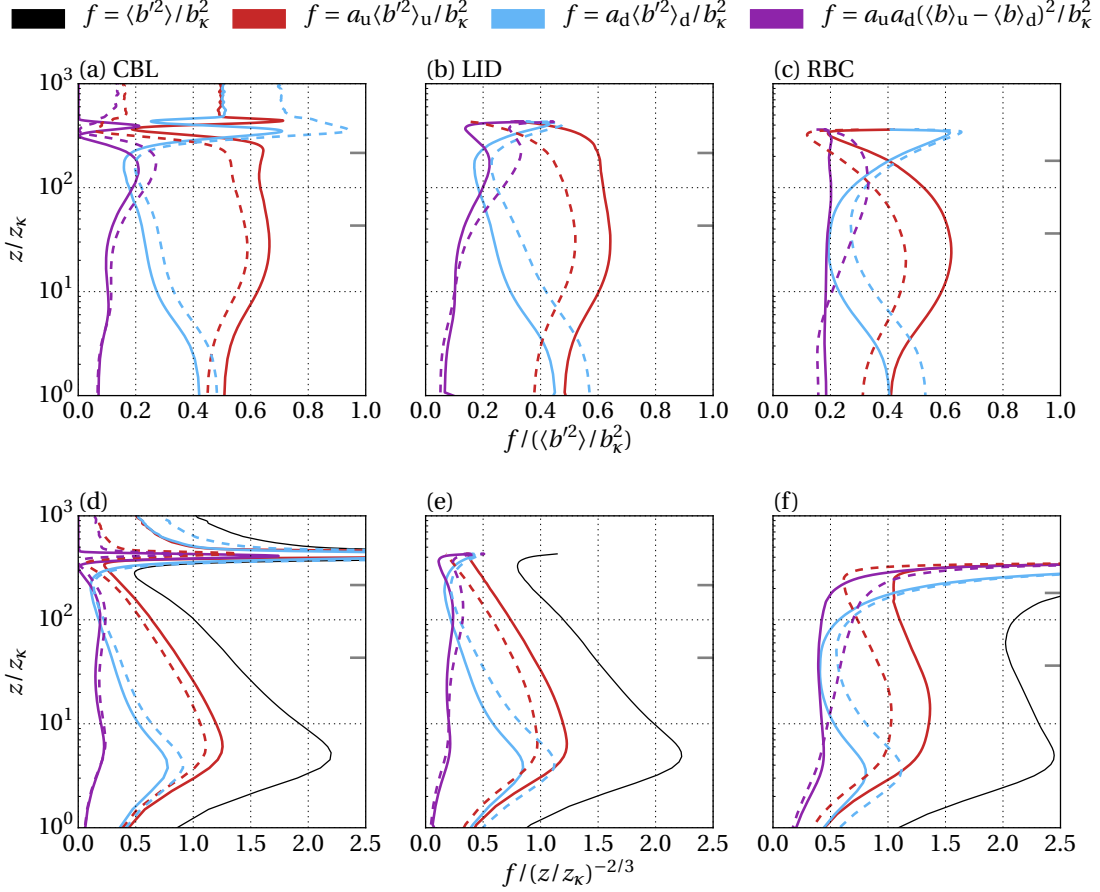


Figure A.8: (a)-(c) Contributions to the total buoyancy variance from updraft, downdraft and mean difference terms. (d)-(f) Buoyancy variance normalized by free-convective scaling. *Thick solid lines* indicate conditioning based only on \bar{w}' and *thick dashed lines* based on both \bar{w}' and \bar{b}' . *Grey ticks* on the right-hand side indicate $0.1h$ and $0.5h$.

profiles, we are able to calculate the form of the mean difference term analytically. This is

$$a_u a_d (\langle b \rangle_u - \langle b \rangle_d)^2 = \alpha (z/z_\kappa)^{-2/3} + \beta (z/z_\kappa)^{-1/3} + \gamma, \quad (\text{A.21})$$

where α , β and γ are constants. MOST predicts the buoyancy variance to follow a $(z/z_\kappa)^{-2/3}$ power law, so the mean difference term could explain part of the deviation from this prediction. However, as shown in Fig. A.8a-b, the mean difference term contributes the least to the total variance in the surface layer of the LID and CBL cases. Moreover, Fig. A.8d-e demonstrate that the mean difference term is in agreement with free-convective scaling (profiles are approximately constant with height) and is hence dominated by $\alpha (z/z_\kappa)^{-2/3}$ rather than $\beta (z/z_\kappa)^{-1/3}$. This confirms that deviations in the buoyancy variance are not caused by the mean difference term.

Downdrafts strongly deviate from free-convective scaling (Fig. A.8d-e) and make a contribution of $\sim 20 - 30\%$ to the total buoyancy variance in the surface layer (Fig. A.8a-b). Whilst this is non-negligible, it is updrafts that most strongly determine the buoyancy variance near the surface and despite expectations that updraft properties would comply better with MOST, strong deviations from free-convective scaling occur within large-scale updraft regions. This result is independent of whether we define updrafts based only on the vertical velocity, or also on the buoyancy fluctuation.

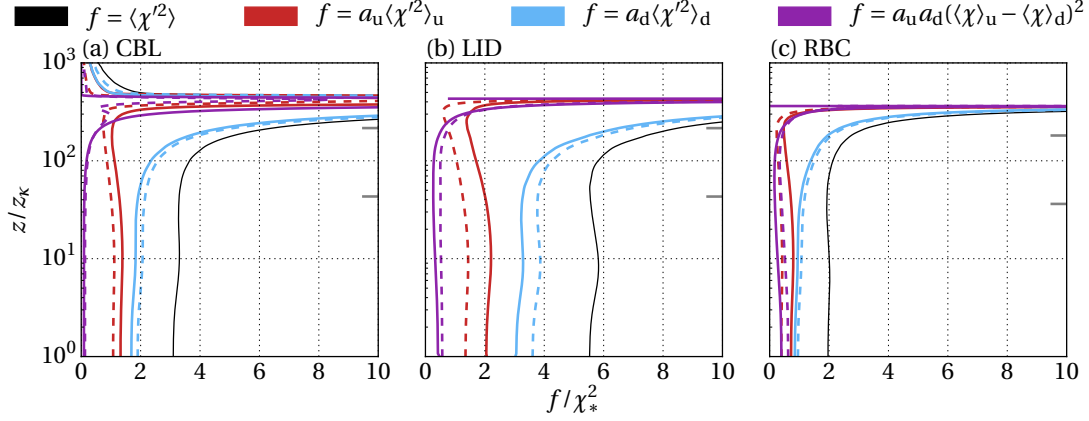


Figure A.9: Top-down scalar variance normalized by the convective scale, $\chi_* = F_{\chi,0}/w_*$. Linestyles are as in Fig. A.8. Grey ticks on the right-hand side indicate $0.1h$ and $0.5h$.

Compared to the other two systems, the buoyancy variance behaves in a similar manner in the RBC case and again, much of the deviation from free-convective scaling occurs within updraft regions (Fig. A.8c,f). The major difference is the behaviour of the downdraft profile and this will be discussed in Sect. A.3.5.

In summary, the first- and second-order moments of the buoyancy are primarily determined by large-scale updraft regions, but somewhat counter-intuitively, MOST is not satisfied within those regions any better than in downdraft regions. Moreover, the buoyancy field behaves very similarly in the LID and CBL cases, even within downdraft regions. This is interesting because the buoyancy is a purely bottom-up scalar in the LID case, but in the CBL case, the buoyancy also has a top-down contribution due to the entrainment flux, and yet the signature of that remote air is not evident in near-surface downdraft statistics. This suggests that even within downdrafts, the buoyancy in the CBL is primarily determined by the bottom-up contribution. In order to test this hypothesis, in the following section we consider the opposite limit of a purely top-down scalar, as this represents the case in which downdrafts have the strongest impact near the surface.

A.3.5 Top-Down Scalar Statistics

The results of the preceding section indicate that the buoyancy scales similarly in both large-scale updraft and downdraft regions. This seems to contradict the original hypothesis that downdrafts would show a much stronger signature of the top-down contribution than updrafts, and leads us to ask to what extent $\langle b'^2 \rangle_d$ near the surface is determined by air descending from aloft (the top-down contribution), and to what extent by thermals rising from the surface within the large-scale downdraft regions (the bottom-up contribution). A strong bottom-up contribution could partly explain the similarity to the updraft profile. To this end, we compare our buoyancy results to those for the top-down scalar (Fig. A.9), which characterizes the contribution of air from aloft since it has zero surface flux.

In all cases, the top-down scalar variance is larger in downdrafts than in updrafts, is approximately constant with height near the surface, and above $0.1h$ (the lower grey tick in Fig. A.9), $\langle \chi'^2 \rangle_d$ begins to increase with height, indicating that top-down scalar

variance from above is carried all the way to the surface layer by downdrafts. By contrast, $\langle b'^2 \rangle_d$ consistently decreases with height faster than $z^{-2/3}$ in the LID and CBL cases (profiles in Fig. A.8d-e lean to the left of the vertical line), indicating a negligible top-down contribution to the buoyancy field near the surface. In the RBC case, the situation is somewhat different (Fig. A.8f). Above $0.1h$, the decrease in $\langle b'^2 \rangle_d$ becomes markedly slower than $z^{-2/3}$ (profiles lean to the right of the vertical line). This suggests that the buoyancy variance within downdrafts already begins to be affected by cold air descending from aloft into the surface layer of the RBC case, whereas for the LID and CBL cases, $\langle b'^2 \rangle_d$ is mainly determined by the bottom-up contribution.

In Fig. A.9b-c, the larger normalized top-down scalar variance in the LID case compared to the RBC case is at first sight surprising and calls for some explanation. The reason is related to the scale at which scalar fluctuations are generated at the top of the domain. Buoyancy fluctuations at the top of the domain in the RBC case are generated at small scales and the dissipation is fast, but in the LID case, which has no buoyancy forcing at the upper plate, buoyancy fluctuations are generated at larger scales by the LSCs and the dissipation is comparatively slow (see Fig A.2). Since the buoyancy is an active scalar, it modulates fluctuations in the velocity field, which the passive scalar follows. Hence, $\langle \chi'^2 \rangle$ is generated at small scales and is dissipated quickly near the upper plate of the RBC case, but in the LID case, it takes longer to dissipate as it first needs to be transferred to smaller scales via the turbulent cascade, so there is more time for $\langle \chi'^2 \rangle$ to be carried down to the surface and accumulate (Mellado et al., 2017).

In summary, the buoyancy variance near the surface scales similarly between updrafts and downdrafts in the LID and CBL cases due to the dominating influence of the bottom-up contribution, associated with thermals penetrating into the downdraft region. In the RBC case, by contrast, the effect of the top-down contribution, associated with cold air descending from aloft, is evident in near-surface downdraft buoyancy statistics.

A.3.6 Vertical Velocity Statistics

We now consider the vertical velocity field. Since the mean velocity is zero in free convection, we only consider the variance. The vertical velocity variance confirms the major results from the analysis of the buoyancy. Both updrafts and downdrafts are of comparable importance to determining $\langle w'^2 \rangle$ near the surface (Fig. A.10a-c) and although deviations from free-convective scaling do occur in downdraft regions, they also occur in updraft regions (Fig. A.10d-f). Once again, the LID and CBL cases demonstrate remarkably similar behaviour, whilst in the RBC case, $\langle w'^2 \rangle_d$ is larger than in the other two cases due to the more vigorous downdraft plumes generating larger vertical velocity fluctuations.

A.3.7 Dependence on Filter Size

When large scales are defined based on a filter length scale equal to h , our results suggest that both large-scale updrafts and downdrafts contribute non-negligibly towards deviations from MOST in the buoyancy and vertical velocity variance. In this section we test the dependence of these results on the definition of updraft and downdraft regions. We utilize the same approach as before, but now define updraft and downdraft regions from three different vertical velocity fields with an increasing filter size: the unfiltered field (filter size equal to 0), the L_i -filtered field and the h -filtered field. For conciseness,

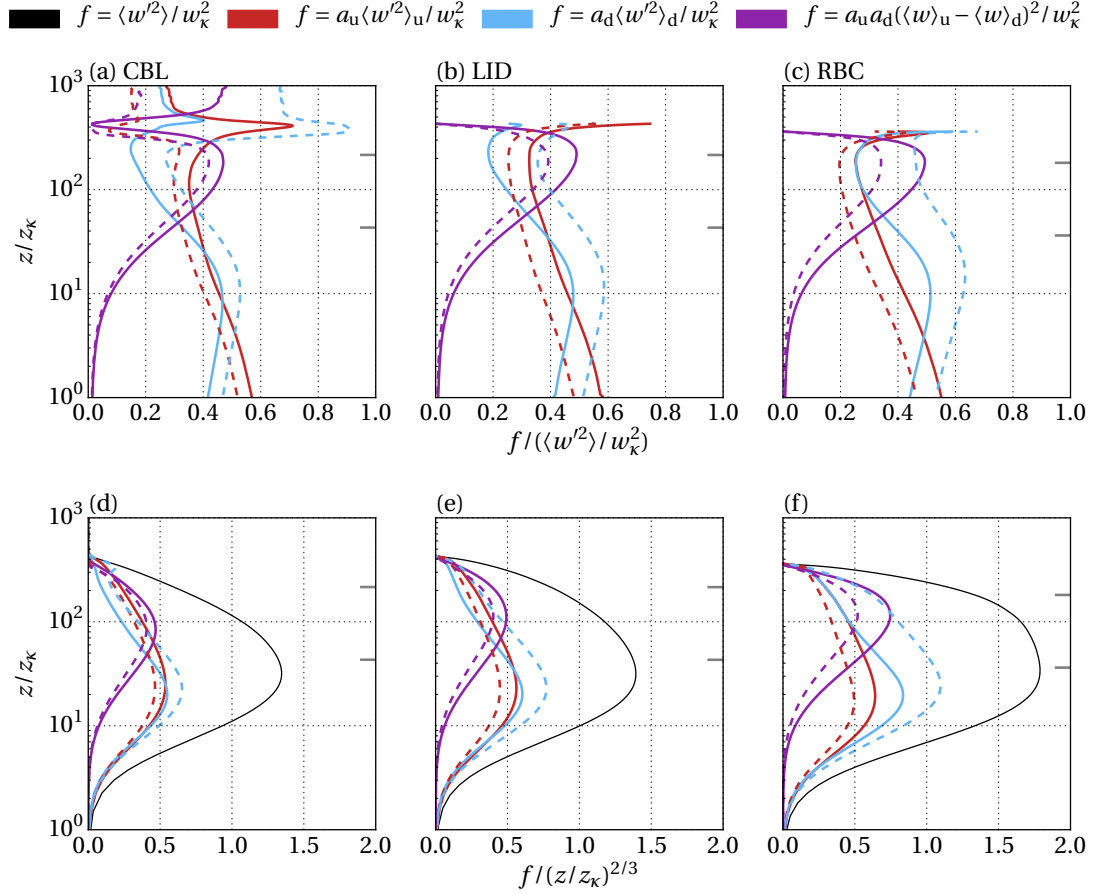


Figure A.10: (a)-(c) Contributions to the vertical velocity variance from updraft, downdraft and mean difference terms. (d)-(f) Velocity variance normalized by free-convective scaling. Linestyles are as in Fig. A.8. Grey ticks on the right-hand side indicate $0.1h$ and $0.5h$.

we only show the CBL case and conditioning based on the vertical velocity, but the results are similar for the non-penetrative cases and the factor of two difference in L_i between the RBC and CBL cases is unimportant.

Fig. A.11 demonstrates that the larger the filter size is, the larger the downdraft contribution is and the more similarly updrafts and downdrafts behave. For second-order moments (Fig. A.11c-d), the increasing downdraft contribution comes at the expense of the mean-difference term, indicating that mean properties within large-scale updraft and downdraft regions become more similar to each other when larger filter sizes are considered (e.g. Fig. A.11b). These order-of-one changes are not caused by differences in the area fraction profile, which only changes by $\sim 2\%$ in the surface layer between $\Delta = L_i$ and $\Delta = h$ (Fig. A.11a), but rather by fluctuations that occur within downdraft regions defined by a larger filter size. For filter sizes of order h , these fluctuations are filtered out of the large-scale fields (see Fig. A.4). When statistics from the original field are taken within those large-scale downdraft regions, they include the fluctuations. Their presence strongly increases the variance within downdraft regions and also causes downdraft properties to become more similar to those of updrafts. This behaviour is consistent with the observation in Sect. A.3.5 that the variance within downdrafts near the surface is mainly determined by the bottom-up contribution associated with thermals

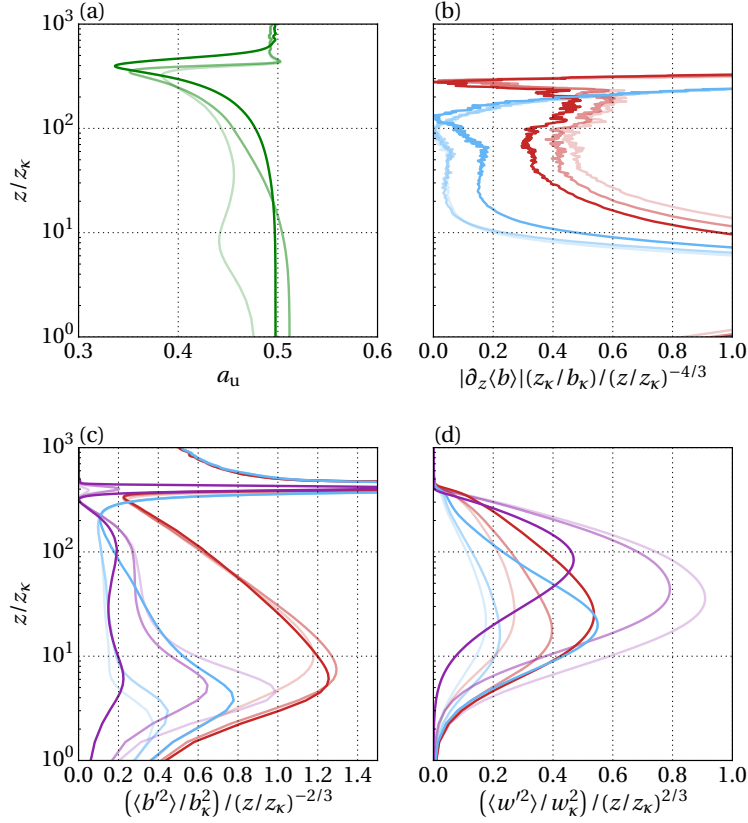


Figure A.11: Sensitivity of conditional statistics in the CBL case to filter size, Δ . (a) Updraft area fraction, (b) mean buoyancy gradient, (c) buoyancy variance and (d) vertical velocity variance. Colours are as in Fig. A.7–A.10. Colour shading indicates (*light*) $\Delta = 0$, (*medium*) $\Delta = L_i = 0.16h$ and (*dark*) $\Delta = h$.

penetrating into the downdraft. For smaller filter sizes of order L_i , the fluctuations are not filtered out (not shown) and instead belong to the updraft regions. Their presence does not greatly alter the behaviour in those regions, hence why updraft properties demonstrate a weaker dependence on filter size.

Despite changes to the downdraft profiles, many of our conclusions in previous sections are robust. Regardless of the filter size used to define LSCs, downdrafts are partially responsible for the failure of the vertical velocity variance to comply with MOST, either directly through the downdraft contribution, or through the mean difference term. Most importantly, for both the buoyancy and the vertical velocity variance, strong deviations occur within large-scale updraft regions, and these are at least as important as downdrafts, if not more so, for determining the behaviour near the surface.

A.4 SUMMARY AND CONCLUSIONS

We have used direct numerical simulation and conditional analysis to explore how large-scale circulations may lead to deviations from MOST in free-convective flows ranging from the convective boundary layer to Rayleigh–Bénard convection. In all three configurations, the Prandtl number is unity and the Reynolds number based on the free-fall velocity is of order 10^4 (equivalently, Rayleigh number of order 10^8). We have focused on the first- and second-order moments of the buoyancy and vertical velocity.

Previous studies have indicated that compliance with MOST is not guaranteed when large-scale downdrafts transport non-local, outer-layer air to the surface layer. Using a spatial filter to define the large scales, we have found that, whilst downdrafts contribute towards deviations from MOST, they are not the most important factor. Comparison with a top-down scalar (a scalar with zero surface flux) reveals that within downdraft regions, the buoyancy variance near the surface is predominantly determined by a bottom-up contribution, suggesting that the transport of non-local air into the surface layer is of little importance in causing deviations from MOST in this quantity.

Strong deviations from MOST also occur within large-scale updraft regions. These deviations are not due to changes in the updraft area fraction with height, which varies by no more than 5% in the surface layer, and occur regardless of the filter size used to define “large scale” and regardless of whether updrafts are defined as ascending air, or as air that is both ascending and positively buoyant. This indicates that near-surface updraft properties are not only determined locally by the surface buoyancy flux and the distance from the ground, but also by outer scales. The reasons for this are unclear. Shear effects caused by the large-scale horizontal flow may play a role here, as suggested before in studies of Rayleigh–Bénard convection, but this requires further investigation, particularly in the convective boundary layer where the large-scale horizontal motion is weaker.

A comparison of the CBL, LID and RBC configurations has shown that replacing a linearly stratified atmosphere with an impenetrable, adiabatic lid has very little impact on surface-layer properties, but if the upper plate is cooled, there are some notable changes of behaviour. In particular, the RBC case differs from the LID and CBL cases in the following ways: firstly, the mean buoyancy does not follow free-convective scaling. Secondly, the buoyancy variance within downdraft regions is not only affected by thermals rising from the surface, but also by cold air descending from aloft. Lastly, the contribution from downdraft regions to the vertical velocity variance is more important. It therefore seems that changes to the upper boundary conditions only result in significant changes in the surface layer if downdrafts are sufficiently cold and strong to modify properties there. Hence, we conclude that at the moderate Reynolds numbers considered here, the LID case is a better model of the unstable atmospheric surface layer than is classical Rayleigh–Bénard convection. The LID case has the advantage that it provides a longer statistically steady state than the CBL case, allowing for greater statistical convergence.

These findings also have implications for field measurements. For example, high- or low-pass filters are sometimes applied to atmospheric measurement data to remove mesoscale variations or inertial subrange turbulence. Whilst our results suggest that such a procedure would have little effect on measurements taken within updrafts, measurements taken within downdraft regions may be more strongly affected by the filter size.

ACKNOWLEDGEMENTS

The authors gratefully acknowledge the Gauss Centre for Supercomputing (GCS) for providing computing time through the John von Neumann Institute for Computing (NIC) on the GCS share of the supercomputer JUQUEEN at Jülich Supercomputing Centre (JSC). This work is supported by the Priority Programme SPP 1881 Turbulent Superstructures of the Deutsche Forschungsgemeinschaft (DFG). Primary data and scripts used in the analysis and other supporting information that may be useful in

reproducing the authors' work are archived by the Max Planck Institute for Meteorology and can be obtained by contacting publications@mpimet.mpg.de.

APPENDIX A.A

Top-hat filters are commonly used in the literature to define large-scale fields and we originally considered a three-dimensional top-hat filter for our study (Pope, 2000). However, the implementation of the top-hat filter near the top and bottom boundaries is challenging for several reasons. First, the top-hat filter is typically implemented defining the filter size equal to an integer multiple of the grid spacing, and because the grid spacing is varying with height near the surface to satisfy the resolution constraints as explained in Sect. A.2.4, the filter size is also varying with height. This artificially introduces an inhomogeneity in the large-scale field that could affect some of the properties that we are interested in, such as the variation with height of the area fractions associated with large-scale updrafts and downdrafts. This problem is solved when using the Helmholtz filter defined via Eq. A.16.

One could avoid this problem by interpolating the DNS data into a uniform grid with a grid spacing equal to the smallest grid spacing in the vertical direction. However, even in this case of a uniform grid, finding appropriate boundary conditions for the filter operation when using a three-dimensional top-hat filter remains a challenge. We considered ghost cells where the fields were defined based on a linear extrapolation from the interior of the domain towards the exterior of the domain, applying then the top-hat filter across the boundary. However, such an approach fails to satisfy the no-slip boundary condition. In Fig. A.12, we demonstrate this by comparing a top-hat filter with the Helmholtz filter in the RBC case. In the case of the top-hat filter, we obtain a non-zero filtered velocity field at the lower and upper boundaries, causing the proportion of TKE remaining in the filtered field to actually increase as the filter size becomes larger. The Helmholtz filter alleviates this issue and results in a systematic decrease in remaining TKE with increasing filter size.

To better understand the implicit definition of the Helmholtz filter via Eq. A.16, one can consider this filter applied only in the horizontal directions, where the periodic boundary conditions allow for Fourier analysis. In this case, one finds that

$$\hat{\phi} = \left[1 + \left(\frac{k\Delta}{2\pi} \right)^2 \right]^{-1} \hat{\phi}, \quad (\text{A.22})$$

where $\hat{\cdot}$ indicates the Fourier transform along the horizontal planes, and k is the corresponding wavenumber. This expression shows that the filtered field is approximately equal to the original field when $k \ll 2\pi/\Delta$, and that the filtered field is approximately zero when $k \gg 2\pi/\Delta$. Hence, Eq. A.16 defines a low-pass filter operation with a filter size Δ .

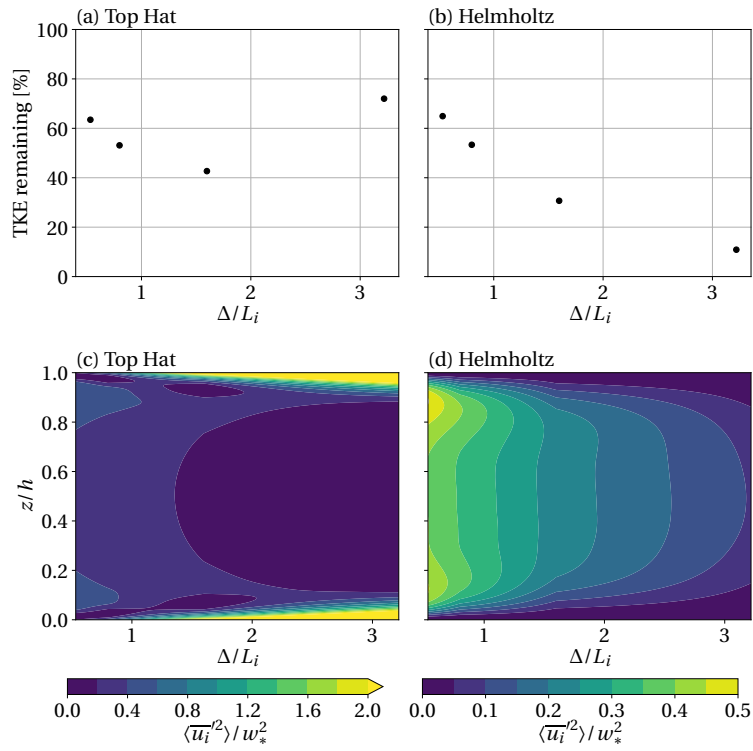


Figure A.12: Comparison of the effect of the top-hat filter and the Helmholtz filter on the TKE in the RBC case. (a)-(b) Percentage of vertically integrated TKE remaining in the filtered flow, $\int_0^h \langle \overline{u_i'^2} \rangle dz / \int_0^h \langle u_i'^2 \rangle dz$, against filter size, Δ . (c)-(d) TKE profile as a function of filter size.

NEW INSIGHTS INTO WIND SHEAR EFFECTS ON ENTRAINMENT
IN CONVECTIVE BOUNDARY LAYERS USING CONDITIONAL
ANALYSIS

The work in this appendix has been submitted to the Journal of Atmospheric Sciences.

The contributions of the authors to this paper are as follows:

K. Fodor performed the analysis and wrote the paper. JP. Mellado conceived the original idea for the work, discussed the results, gave direction on how to proceed and reviewed the manuscript.

New Insights into Wind Shear Effects on Entrainment in Convective Boundary Layers Using Conditional Analysis

Katherine Fodor¹ and Juan Pedro Mellado²

¹Max Planck Institute for Meteorology, Hamburg, Germany

²Universitat Politècnica de Catalunya, Barcelona, Spain

Received: 17 December 2019 / Accepted: XXXX / Published online: XXXX

Conventional analysis has shown that wind shear enhances the entrainment buoyancy flux in the convective boundary layer. By conditioning the entrainment zone into regions of turbulent and non-turbulent flow, some unexpected aspects of this process are revealed. It is found that turbulent regions contribute the most to the entrainment buoyancy flux, but that as wind shear increases, the magnitude of the buoyancy flux in turbulent regions remains approximately constant, or even decreases, despite substantially stronger buoyancy fluctuations. The reason is that the correlation between buoyancy and vertical velocity fluctuations decreases with increasing wind shear, to the extent that it compensates the stronger buoyancy fluctuations. In free convection, this correlation is high because the vertical velocity is mainly determined by the buoyancy force acting in the same direction. Under strong shear conditions, buoyancy is no longer the only external source of vertical velocity fluctuations and their correlation consequently decreases. Hence, shear enhancement of the buoyancy flux in the entrainment zone is primarily due to an increase of the turbulent area fraction, rather than a change of flux inside the turbulent regions.

B.1 INTRODUCTION

Wind shear is well known to enhance fluxes at the top of the convective boundary layer (CBL). This is commonly attributed to the additional shear production of turbulent kinetic energy (TKE), which acts to increase the magnitude of fluctuations in both the velocity field and thermodynamic properties (Pino et al., 2003; Conzemius and Fedorovich, 2006; Pino and Arrellano, 2006; Fedorovich and Conzemius, 2008). The growth of the CBL, as well as the evolution of boundary-layer clouds, depend crucially on these changes.

One of the more important properties with regards to CBL growth and cloud dynamics is the buoyancy flux. In order to understand the mechanisms behind shear enhancement of the buoyancy flux, Kim et al. (2003) employed quadrant analysis and found that buoyancy and vertical velocity fluctuations in each quadrant are increased by the large amplitude oscillations of the CBL top induced by wind shear.

Whilst quadrant analysis is helpful in determining the sign of fluctuations that contribute to entrainment (Sullivan et al., 1998), other aspects are more difficult to extract. One important issue is external intermittency, which is the property that at the edge of a free turbulent flow, the motion is in some places turbulent and in others not turbulent (Pope, 2000). The alternation between turbulent and non-turbulent regions can be seen in visualizations, for example, as a pattern of alternating regions of high and low vorticity magnitude. In the entrainment zone, external intermittency arises due to the entrainment of non-turbulent air from the free troposphere and the ascension of turbulent thermals from the CBL interior. Whilst motion within the non-turbulent regions is primarily downward, the turbulent motion within thermals is not uni-directional and hence quadrant analysis, which splits motion into ascending and descending air, is insufficient to distinguish turbulent from non-turbulent regions. As a result, quadrant analysis may be intermingling a number of different wind shear effects.

There are several plausible hypotheses for how wind shear could modify turbulent and non-turbulent properties, such that it leads to a stronger buoyancy flux in the entrainment zone:

1. Due to the larger amplitude oscillations of the turbulent/non-turbulent interface (TNTI), wind shear creates a larger difference in mean properties between turbulent and non-turbulent regions.
2. Wind shear generates more vigorous fluctuations within the turbulent region.
3. The large-scale structures in the CBL change when wind shear is added, which alters the distribution of turbulent patches in the entrainment zone and thereby the turbulent area fraction.

Each of these changes can contribute to a larger buoyancy flux, but currently their individual contributions are unknown. Understanding these contributions could help inform CBL models (Negggers et al., 2006; Siebesma et al., 2007; Mellado, 2017). In this paper, we introduce the method of conditional analysis as a way to understand the interplay between these different contributions towards wind shear enhancement of the entrainment buoyancy flux.

Partitioning of the flow into regions of high and low vorticity magnitude requires the detection of small-scale fluctuations in the enstrophy field. Direct numerical simulation (DNS) has been used with success in this regard for classical flows of engineering importance (Bisset et al., 2002; Mellado et al., 2009; van Reeuwijk and Holzner, 2014),

as well as in studies of unstratified penetrative convection (Holzner and van Reeuwijk, 2017) and gravity currents (van Reeuwijk et al., 2018). Despite DNS gaining traction in the study of sheared CBLs (Jonker et al., 2013; Haghshenas and Mellado, 2019), it has not yet been applied in that context in combination with conditioning on turbulent and non-turbulent regions. A further goal of this paper is therefore to assess whether the Reynolds numbers we are able to achieve nowadays with DNS are sufficiently large for this kind of conditional analysis to be useful in the CBL.

Conditioning statistics on either side of the TNTI has been used in a variety of canonical flows in fluid mechanics, such as wakes, jets and turbulent boundary layers (Corrsin and Kistler, 1955; Kovasznay et al., 1970; Silva et al., 2014). Deardorff et al. (1980) first considered the use of this kind of conditional analysis in laboratory studies of the CBL, noting that a description of the entrainment zone in terms of the turbulent area fraction, rather than in terms of buoyancy profiles, would aid comparison with mechanically-driven flows. In the stable boundary layer, partitioning of the flow into turbulent and non-turbulent sub-volumes has indicated that properties within turbulent regions remain similar with changing stratification strength (Ansorge and Mellado, 2016). By considering the unstable boundary layer here, we help to bridge work across a variety of atmospheric boundary layer regimes.

This paper is organized as follows. In Section B.2 we provide an overview of our simulations and the basics of conditional analysis. In Section B.3 we explain the method we use to partition the flow into turbulent and non-turbulent regions. We then explore how wind shear modifies the turbulent area fraction in Section B.4 and the buoyancy flux in Section B.5. A summary is given in Section B.6.

B.2 NUMERICAL SIMULATIONS AND ANALYSIS METHODS

We consider a barotropic CBL that is forced by a constant and homogeneous surface buoyancy flux, B_0 , and that grows into a linearly stratified free atmosphere. Such conditions are representative of the afternoon atmospheric boundary layer over land. We consider the limit of zero Coriolis parameter. The velocity and buoyancy frequency in the free atmosphere are denoted U_0 and N_0 respectively. Our set-up is identical to that in Haghshenas and Mellado (2019), so here we only provide a brief overview and refer the reader to the aforementioned work for further details. The only difference from that work is that we have continued one of the simulations further into the quasi-steady state of the CBL.

B.2.1 Governing Equations

We solve the conservation equations for mass, momentum and energy in the Boussinesq approximation:

$$\nabla \cdot \mathbf{u} = 0, \tag{B.1a}$$

$$\frac{\partial \mathbf{u}}{\partial t} + \nabla \cdot (\mathbf{u} \otimes \mathbf{u}) = -\nabla p + \nu \nabla^2 \mathbf{u} + b\mathbf{k}, \tag{B.1b}$$

$$\frac{\partial b}{\partial t} + \nabla \cdot (b\mathbf{u}) = \kappa \nabla^2 b, \tag{B.1c}$$

where $\mathbf{u}(\mathbf{x}, t)$ is the velocity vector with components (u, v, w) , $\mathbf{x} = (x, y, z)$ is the position vector with z as the vertical coordinate, t is time, $\mathbf{k} = (0, 0, 1)$ is the unit vector in the vertical direction and p is the modified pressure divided by a constant reference density. The

buoyancy, b , is related to the virtual potential temperature, θ_v , via $b \approx g(\theta_v - \theta_{v,0})/\theta_{v,0}$, where $\theta_{v,0}$ is a constant reference value and g is the gravitational acceleration. The parameters ν and κ are the kinematic viscosity and the thermal diffusivity respectively.

B.2.2 Simulations

The velocity field satisfies impermeable, no-slip boundary conditions at the surface and impermeable, free-slip boundary conditions at the top of the domain, which is placed sufficiently far above the CBL to not influence its evolution. An initial velocity field is constructed that is zero at the surface and a constant value, U_0 , in the free atmosphere that flows in the x -direction.

The buoyancy field satisfies Neumann boundary conditions at both the top and bottom of the domain. At the surface, $\partial_z b = -B_0/\kappa$, and at the top of the domain, $\partial_z b = N_0^2$. The initial buoyancy field is set such that the buoyancy increases linearly with height with gradient N_0^2 in the free atmosphere.

The system is characterized by three non-dimensional control parameters: the Prandtl number, $\text{Pr} \equiv \nu/\kappa$, a reference buoyancy Reynolds number,

$$\text{Re}_0 \equiv \frac{B_0}{\nu N_0^2}, \quad (\text{B.2})$$

and a reference Froude number:

$$\text{Fr}_0 \equiv \frac{U_0}{N_0 L_0}, \quad (\text{B.3})$$

where

$$L_0 \equiv \left(\frac{B_0}{N_0^3} \right)^{1/2} \quad (\text{B.4})$$

is a reference Ozmidov length. The Ozmidov length represents the largest scale at which overturning of eddies is uninhibited by the stratification (Dougherty, 1961; Ozmidov, 1965).

The Prandtl number characterizes the properties of the working fluid, the Reynolds number can be thought of as a measure of the scale separation present in the flow (see Section B.3 for more details) and the Froude number characterizes how strong the wind shear is. We fix the Prandtl number to be equal to one in all of our simulations as this is similar to the Prandtl number of air. Most of our analysis is conducted at $\text{Re}_0 = 42$, but in Appendix B.B we assess the Reynolds number dependence of some flow properties, for which we also consider simulations at $\text{Re}_0 = 25$ and $\text{Re}_0 = 117$ (see Table B.1). Our analysis compares simulations at $\text{Fr}_0 = 0$, a shear-free case, with a simulation at $\text{Fr}_0 = 20$, a strong shear case corresponding to wind speeds of around $10 - 15 \text{ m s}^{-1}$ for typical midday conditions over land.

Because the horizontal directions are statistically homogeneous, statistical properties of the system depend only on height and time. We non-dimensionalize height using the encroachment length scale:

$$z_{\text{enc}} \equiv \left\{ 2N_0^{-2} \int_0^{z_\infty} [\langle b \rangle(z, t) - N_0^2 z] dz \right\}^{1/2}, \quad (\text{B.5})$$

where z_∞ is located far enough into the free atmosphere for the integral to be approximately independent of z_∞ . In both the shear-free and the sheared cases, z_{enc} characterizes

Table B.1: Simulation Properties. The Reynolds number, Re_0 , is defined in Eq. (B.2) and the Froude number, Fr_0 , is defined in Eq. (B.3). The fourth column shows the final time of the simulations. The fifth column shows how the height of minimum buoyancy flux, $z_{i,f}$, varies between $z_{enc}/L_0 = 15$ and the final time of the simulation.

Re_0	Fr_0	Grid	z_{enc}/L_0	$z_{i,f}/z_{enc}$
25	0	$2560 \times 2560 \times 512$	35	1.14 – 1.14
42	0	$2560 \times 2560 \times 896$	33	1.14 – 1.14
42	20	$3072 \times 4608 \times 960$	26	1.24 – 1.16
117	0	$5120 \times 5120 \times 1024$	22	1.15 – 1.15

the depth of the mixed layer. Rather than using a non-dimensional time as an independent variable, it proves convenient to use the non-dimensional height z_{enc}/L_0 , which describes the temporal evolution of the CBL growth (Garcia and Mellado, 2014). By means of integral analysis of the evolution equation for the buoyancy, Eq. (B.1c), one obtains the following relationship between the encroachment length and time:

$$\frac{z_{enc}}{L_0} = [2N_0(1 + Re_0^{-1})(t - t_0)]^{1/2}, \quad (\text{B.6})$$

where t_0 is a constant of integration.

The reason we analyze the system using non-dimensional variables is that it removes redundancy, since various combinations of the dimensional parameters can yield equivalent results. This implies that we need only one simulation to cover all possible combinations of the dimensional parameters that yield the same non-dimensional parameters. Moreover, such an approach allows comparisons to be made between atmospheric measurements, physical experiments and numerical simulations. For instance, a CBL in the real atmosphere with a mixed-layer depth of $z_{enc} = 1$ km, a surface buoyancy flux of $B_0 = 0.5 \times 10^{-2} \text{ m}^2 \text{ s}^{-3}$ and a buoyancy frequency of $N_0 = 0.8 \times 10^{-2} \text{ s}^{-1}$ is comparable to a tank experiment of a CBL with a mixed-layer depth of $z_{enc} = 1$ m, a surface buoyancy flux of $B_0 = 1 \times 10^{-3} \text{ m}^2 \text{ s}^{-3}$ and a buoyancy frequency of $N_0 = 4.6 \times 10^{-1} \text{ s}^{-1}$ because both cases correspond to a state of development of $z_{enc}/L_0 \approx 10$.

We can match typical atmospheric values of all non-dimensional parameters except for the Reynolds number. Consequently, simulations at different Reynolds numbers are required to assess the dependence of our results on this parameter (see Appendix B.B).

B.2.3 Structure of the Entrainment Zone

We define the entrainment zone as the region of negative buoyancy flux, which starts at approximately z_{enc} in all cases, and has a two layer structure (Garcia and Mellado, 2014; Haghshenas and Mellado, 2019). The lower sublayer is located around $z_{i,f}$, the height of minimum buoyancy flux, and the upper sublayer is located around $z_{i,g}$, the height of maximum mean buoyancy gradient. Wind shear thickens the entrainment zone and hence reference heights in the sheared case are higher up than in the shear-free case. However, over time, shear effects diminish and the entrainment zone tends towards the convection-dominated regime (see column 5 in Table B.1).

The entrainment flux ratio is defined as the minimum of the buoyancy flux normalized by the surface flux: $-\langle b'w' \rangle_{z_{i,f}}/B_0$. Since we are seeking to explain how wind shear

increases this quantity, much of our analysis will take place at the height of minimum buoyancy flux.

B.2.4 Conditional Analysis Preliminaries

To investigate how properties differ between turbulent and non-turbulent regions in the entrainment zone and how they evolve over time, we use conditional statistics (Dopazo, 1977; Antonia, 1981). The conditional mean of a dependent variable, ϕ , may be expressed as:

$$\langle \phi \rangle = a_T \langle \phi \rangle_T + a_{NT} \langle \phi \rangle_{NT}, \quad (\text{B.7})$$

where a_T and $a_{NT} = 1 - a_T$ are respectively the turbulent and non-turbulent area fractions, and $\langle \phi \rangle_T$ and $\langle \phi \rangle_{NT}$ are respectively the mean inside turbulent and non-turbulent regions. From the definition $\phi' \equiv \phi - \langle \phi \rangle$, one obtains the following expression for the conditional variance:

$$\begin{aligned} \langle \phi'^2 \rangle &= a_T \langle \phi'^2 \rangle_T + a_{NT} \langle \phi'^2 \rangle_{NT} \\ &\quad + a_T a_{NT} (\langle \phi \rangle_T - \langle \phi \rangle_{NT})^2, \end{aligned} \quad (\text{B.8})$$

where $\langle \phi'^2 \rangle_T = \langle \phi^2 \rangle_T - \langle \phi \rangle_T^2$ and $\langle \phi'^2 \rangle_{NT} = \langle \phi^2 \rangle_{NT} - \langle \phi \rangle_{NT}^2$. The first term on the right-hand side of Eq. (B.8) is the contribution from the variance inside turbulent regions, the second term is the contribution from the variance inside non-turbulent regions and the third term is caused by the difference between the mean inside turbulent and non-turbulent regions, hereafter referred to as the mean difference term.

Similarly one can derive an expression for the vertical flux of ϕ as:

$$\begin{aligned} \langle \phi' w' \rangle &= a_T \langle \phi' w' \rangle_T + a_{NT} \langle \phi' w' \rangle_{NT} \\ &\quad + a_T a_{NT} (\langle \phi \rangle_T - \langle \phi \rangle_{NT}) (\langle w \rangle_T - \langle w \rangle_{NT}). \end{aligned} \quad (\text{B.9})$$

In Section B.5, we will show how wind shear affects each of the contributing terms in Eq. (B.9) for $\phi = b$.

B.3 DEFINITION OF TURBULENT AND NON-TURBULENT REGIONS

In order to proceed with the conditional analysis, we need to define what is turbulent and what is not. In studies of the TNTI, turbulent regions are typically defined based on a low enstrophy threshold, below which the flow may be considered approximately irrotational (Silva et al., 2014). In the real atmosphere, the scale separation between the enstrophy values characterizing the boundary layer and those characterizing the free troposphere is huge (of order 10^6 , as explained below), but in our simulations, we can only achieve a limited scale separation, which needs to be assessed.

Various methods for selecting an enstrophy threshold have been employed in past studies of the TNTI. One method commonly employed in shear-driven boundary layers takes into account the structure of the probability density function (PDF) of enstrophy, which has two peaks connected by a plateau: one above the boundary layer at low enstrophy values, indicating the non-turbulent region, and one within the boundary layer at high enstrophy values, indicating the turbulent region (Borrell and Jiménez, 2016; Watanabe et al., 2018). A threshold is then chosen as the saddle point in the PDF, because it divides between enstrophy values more likely to be found in the boundary

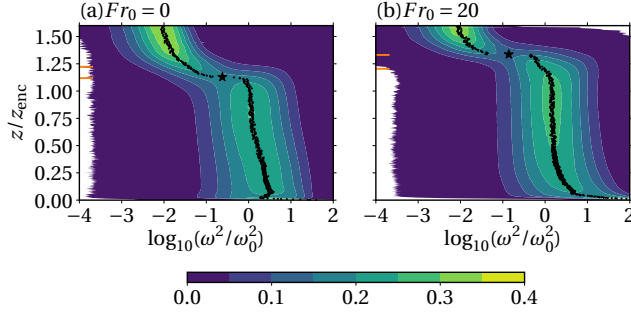


Figure B.1: Probability density functions of enstrophy at $z_{\text{enc}}/L_0 = 20$ averaged over an interval $\Delta z_{\text{enc}}/L_0 = 2$. The black dots indicate the maximum in the PDF at each height. The star shows the approximate saddle point. The orange markers on the left-hand side indicate (lower) $z_{i,f}$ and (upper) $z_{i,g}$. The reference scale ω_0^2 is defined in Eq. (B.13) with $c_\varepsilon = 0.1$.

layer and enstrophy values more likely to be found outside of it. Since the CBL has a similar structure to the shear-driven boundary layer in this regard, we employ a similar method to identify a threshold.

We first define a reference enstrophy scale in the mixed layer in order to normalize the PDFs. This can be derived from the relationship between enstrophy, ω^2 , and the viscous dissipation rate of TKE, ε :

$$\langle \varepsilon \rangle = \nu \langle \omega^2 \rangle + 2\nu \frac{\partial^2 \langle w^2 \rangle}{\partial z^2}, \quad (\text{B.10})$$

which simplifies to:

$$\langle \varepsilon \rangle \approx \nu \langle \omega^2 \rangle, \quad (\text{B.11})$$

because the second term on the right hand side of Eq. (B.10) is small in the mixed layer. It then follows that:

$$\langle \omega^2 \rangle \sim \frac{\langle \varepsilon \rangle}{\nu} \sim \frac{B_0}{\nu}, \quad (\text{B.12})$$

where the last relation follows from an integral analysis of the TKE evolution equation in the quasi-steady regime of the CBL (Fedorovich et al., 2004). We therefore define a reference enstrophy scale in the mixed layer as:

$$\omega_0^2 \equiv \frac{c_\varepsilon B_0}{\nu}. \quad (\text{B.13})$$

This reference scale is verified in Fig. B.1 with $c_\varepsilon = 0.1$.

Under typical midday conditions in the real CBL, $B_0 \approx (0.3 - 1) \times 10^{-2} \text{ m}^2 \text{ s}^{-3}$ and $\nu = 1.5 \times 10^{-5} \text{ m}^2 \text{ s}^{-1}$, yielding enstrophy values in the mixed layer of order $10 - 10^3 \text{ s}^{-2}$ (for c_ε of order 0.1-1). In the free atmosphere, which is dominated by gravity wave motion, the enstrophy scales with $N_0^2 \approx (0.4 - 3.2) \times 10^{-4} \text{ s}^{-2}$. Hence, the scale separation between the boundary layer and free atmosphere, $\omega_0^2/N_0^2 \approx \text{Re}_0$, is of order $10^5 - 10^7$, demonstrating that the scale separation increases with increasing Reynolds number (see also Appendix B.B). In numerical simulations however, the Reynolds number and the corresponding scale separation in the flow determine how many grid points are required, and thereby the size of the simulation. This is strongly constrained by computational resources and we are therefore limited to Reynolds numbers much smaller than those

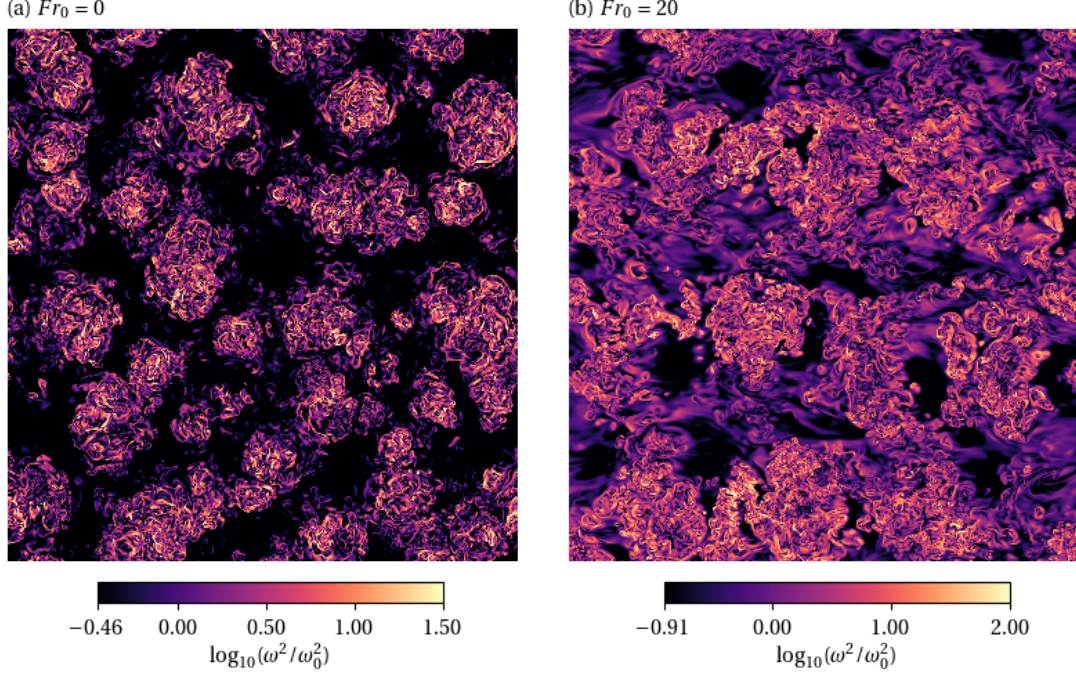


Figure B.2: Logarithm of enstrophy at the height of minimum buoyancy flux, at time $z_{\text{enc}}/L_0 = 20$ and for (a) $Fr_0 = 0$ and (b) $Fr_0 = 20$ (mean wind from left to right). The colour scale has black as the threshold indicated by the star in Fig. B.1. The full horizontal domain is shown and is equal to $215L_0 \times 215L_0$ in both cases.

characterizing the real atmosphere (Mellado et al., 2018). As observed in Fig. B.1, in our simulations at $Re_0 = 42$, we only achieve a scale separation of order 10^2 . Nonetheless, this is sufficient to make a distinction between turbulent and non-turbulent regions, as will be demonstrated in later sections.

To identify a reference threshold for our analysis, we find an approximation to the saddle point in the enstrophy PDF as follows. First, we find the maximum in the PDF at each height (the black dots in Fig. B.1). Then, we search along that set of points for where there is a jump in enstrophy values between two consecutive grid points. The size of this jump has to be tuned somewhat depending on the case. We choose the size of the jump to be a factor of at least $1.5 \omega^2/\omega_0^2$ in the $Fr_0 = 0$ case and a factor of at least $3 \omega^2/\omega_0^2$ in the $Fr_0 = 20$ case. The saddle point is then approximated as the mean value between the points on either side of the jump (the star in Fig. B.1). To give a visual impression of turbulence defined by this reference threshold, in Fig. B.2 we show a horizontal cross-section of the enstrophy field at $z_{i,f}$. Enstrophy values below the reference threshold are blacked out and what remains has the characteristic features of turbulent plumes in the shear-free case (Fig. B.2a) and of horizontal rolls in the sheared case (Fig. B.2b).

One of the main effects of wind shear is to increase the height of the saddle point from $z_{i,f}$ to $z_{i,g}$. The correspondence of the saddle point to these reference heights is seen more clearly in Fig. B.3a. Whilst it is expected that the saddle point lies within the entrainment zone, there is a priori no physical reason that the saddle point is closer to one reference height or another. The saddle point is higher up in the sheared case because the turbulence intensity only starts to decay around the height $z_{i,f}$ (Fig. B.1b). In the shear-free case by contrast, turbulence already starts to decay upon entering the entrainment zone (i.e. slightly above z_{enc} , Fig. B.1a) and as a result, the saddle point in

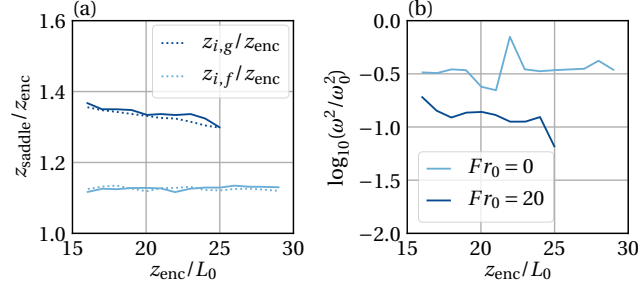


Figure B.3: Time evolution of (a) the height and (b) the magnitude of the saddle points indicated by the stars in Fig. B.1. Here and in the following, lines indicate the average over an interval $\Delta z_{\text{enc}}/L_0 = 2$.

the enstrophy PDF occurs lower down. The magnitude of the enstrophy saddle point is similar between the two cases, though slightly smaller in the sheared case due to the saddle point being closer to the non-turbulent region (Fig. B.3b). The reference threshold we use for each Fr_0 case in the following sections is the mean value of the respective curve in Fig. B.3b.

B.4 TURBULENT AREA FRACTION

One of the most important variables in the conditional analysis we perform is the turbulent area fraction, a_T (see Eq. (B.7)-(B.9)). As we will see, this property is also the one most directly affected by the definition of turbulent and non-turbulent regions. We therefore evaluate how changes to the enstrophy threshold impact the turbulent area fraction, whilst still maintaining our primary goal of investigating wind shear effects.

In Fig. B.4, we show the turbulent area fraction, a_T , as a function of height and threshold. The structure of these profiles mirrors the structure of the PDFs considered in the previous section. Turbulence starts to decay with height as soon as it enters the entrainment zone in the shear-free case, and maintains a constant value up to $z_{i,f}$ in the sheared case.

Around the height $z_{i,f}$, where our analysis is focused, the turbulent area fraction is sensitive to the threshold within a certain range, outside of which it no longer changes significantly. When the threshold is too high, $(a_T)_{z_{i,f}} \rightarrow 0$ and when the threshold is too low, $(a_T)_{z_{i,f}} \rightarrow 1$. In both of these circumstances, conditional statistics become equivalent to the conventional statistics, as can be seen from Eq. (B.7)-(B.9). There is therefore only a limited range of thresholds where the conditioning is meaningful. We can estimate this range from Fig. B.4a to be $-1.5 \lesssim \log_{10}(\omega_{\text{th}}^2/\omega_0^2) \lesssim 0.5$. Within that range, a comparable threshold on enstrophy in the shear-free and sheared cases always results in a higher turbulent area fraction in the sheared case at the same reference height. Thus, whilst changing the threshold alters the magnitude of turbulent and non-turbulent properties, the relationship between the shear-free and sheared cases remains qualitatively the same. This is shown to hold in Appendix B.A for a number of different properties.

By considering properties at a single threshold, we can better see the effects of wind shear. For our reference threshold defined in Section B.3, wind shear increases the turbulent area fraction in the mixed layer by around 15%, but in the entrainment zone the effects are more significant (Fig. B.5a). We see in Fig. B.5b that at $Fr_0 = 20$, the turbulent area fraction at $z_{i,f}$ has increased by around 70% of the shear-free value. Since the thresholds used are comparable between $Fr_0 = 0$ and $Fr_0 = 20$, we attribute this

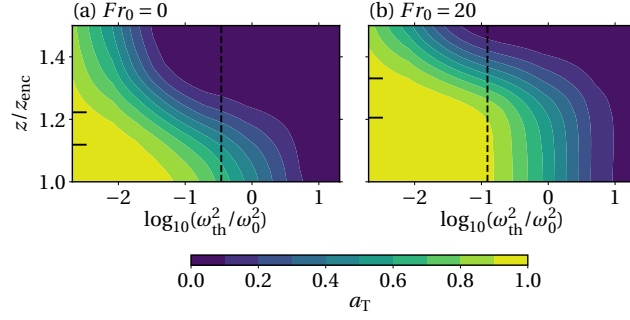


Figure B.4: Contour plots of turbulent area fraction as a function of height and enstrophy threshold at $z_{\text{enc}}/L_0 = 20$. The contours are averages over an interval $\Delta z_{\text{enc}}/L_0 = 2$. The black dashed line indicates the reference threshold (the mean value of the saddle point in Fig. B.3b). The black markers on the left-hand side indicate (lower) $z_{i,f}$ and (upper) $z_{i,g}$.

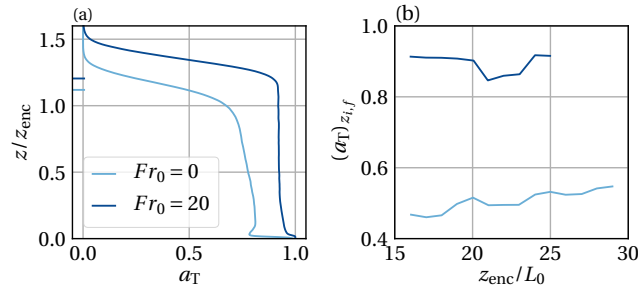


Figure B.5: Turbulent area fraction as a function of (a) height at $z_{\text{enc}}/L_0 = 20$ and (b) time at $z_{i,f}$. The threshold used in each case is the mean value of the respective curve in Fig. B.3b. The markers on the left-hand side in panel (a) indicate $z_{i,f}$.

increase of turbulence coverage to the changing structure of convective plumes, which undergo the well-known transition from cells to horizontal rolls with the addition of wind-shear (see Fig. B.2 and Salesky et al. (2017)). Indeed, if the same threshold value used in the $Fr_0 = 20$ case were used in the $Fr_0 = 0$ case, the turbulent area fraction at $z_{i,f}$ would increase, but still not exceed that in the sheared case. Wind shear thus definitively spreads turbulence over a wider area in the entrainment zone.

Fig. B.5b bears a strong resemblance to the evolution of the total buoyancy flux at $z_{i,f}$ over time at different Fr_0 (see Fig. 5a in Haghshenas and Mellado (2019)). This already suggests that the turbulent area fraction may be a key variable in controlling the magnitude of the entrainment flux under different shear conditions, lending support to the third hypothesis in Section B.1. We explore this possibility further in the following section.

B.5 WIND SHEAR EFFECTS ON THE BUOYANCY FLUX

Using the reference threshold defined in Section B.3, we show each of the three terms in Eq. (B.9) as a function of height in Fig. B.6a for each Fr_0 . It is immediately evident that the turbulent contribution is by far the largest to the total buoyancy flux and that wind shear does little to modify the other two terms. We can therefore already eliminate the first hypothesis posed in Section B.1 and write:

$$\langle b'w' \rangle \approx a_T \langle b'w' \rangle_T. \quad (\text{B.14})$$

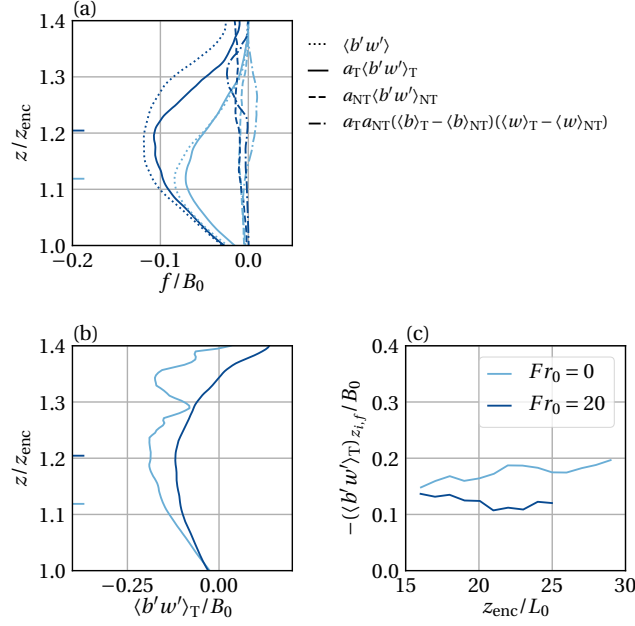


Figure B.6: (a) Contributions to the total buoyancy flux according to Eq. (B.9). The markers on the left-hand side indicate $z_{i,f}$. (b) Buoyancy flux within turbulent regions as a function of height at $z_{enc}/L_0 = 20$. (c) Entrainment flux ratio conditioned to turbulent regions as a function of time.

We have seen that, in the sheared CBL, the turbulent area fraction at $z_{i,f}$ increases by around 70% of its shear-free value, whereas the increase in the magnitude of the total buoyancy flux at $z_{i,f}$ between $Fr_0 = 0$ and $Fr_0 = 20$ is around 50%. By Eq. (B.14), this suggests that $\langle b'w' \rangle_T$ should in fact become somewhat *smaller* with increasing Fr_0 and this is verified in Fig. B.6b,c. Even with a lower enstrophy threshold in the shear-free case, the buoyancy flux in turbulent regions remains similar to that in the sheared case, as shown in Appendix B.A, which would seem to eliminate our second hypothesis that fluctuations become stronger in turbulent regions with increasing wind shear and thereby enhance the entrainment buoyancy flux. Although the first two hypotheses posed in Section B.1 were perhaps the more intuitive ones, our third hypothesis is confirmed: it is the increase in the turbulent area fraction with wind shear that is the main reason for the increase in the magnitude of the total buoyancy flux.

B.5.1 Why is the mean difference term so small?

It is not immediately obvious why our first hypothesis failed. In this section, we explore why the mean difference term turns out to be so small.

Figure B.7 shows the mean buoyancy and the mean vertical velocity separately in turbulent and non-turbulent regions. The mean buoyancy in non-turbulent regions tends towards the background buoyancy profile $N_0^2 z$. The mean buoyancy in turbulent regions corresponds to air ascending from the mixed layer. As the turbulent thermals mix with their environment, their mean buoyancy increases, resulting in a difference between $\langle b \rangle_T$ and $\langle b \rangle_{NT}$ of approximately $0.1b_{enc}$ in the upper entrainment zone sublayer and free atmosphere ($b_{enc} \equiv N_0^2 z_{enc}$).

The mean vertical velocity in non-turbulent regions is negative in the lower entrainment zone sublayer due to entrained air moving down towards the boundary layer interior.

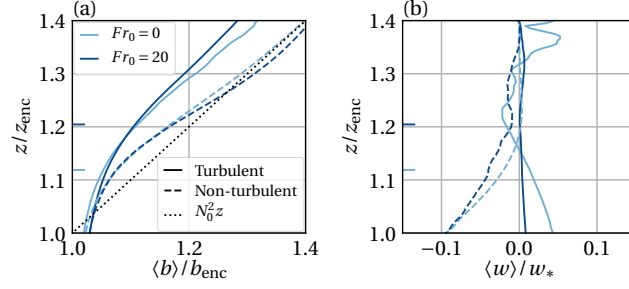


Figure B.7: (a) Mean buoyancy as a function of height and (b) mean vertical velocity as a function of height at $z_{enc}/L_0 = 20$. The scales b_{enc} and w_* are defined as: $b_{enc} \equiv N_0^2 z_{enc}$ and $w_* \equiv (B_0 z_{enc})^{1/3}$. The markers on the left-hand side indicate $z_{i,f}$.

Further up, $\langle w \rangle_{NT}$ becomes dominated by gravity wave motion, which, averaged over the horizontal plane, becomes zero. The mean vertical velocity in turbulent regions decreases to zero in the lower entrainment zone sublayer, which can be interpreted as a weakening of turbulent plumes as they penetrate into the overlying stratification. This effect is clearer in the shear-free case, as the vertical motion is stronger than in the sheared case. Fluctuations about zero in the upper entrainment zone sublayer and free atmosphere are due to limited statistical convergence as a_T becomes small.

Despite there being a relatively large difference between $\langle w \rangle_T$ and $\langle w \rangle_{NT}$ in the lower entrainment zone sublayer, the similarity between $\langle b \rangle_T$ and $\langle b \rangle_{NT}$ there results in a negligible contribution from the mean difference term in Eq. (B.9). In the upper entrainment zone sublayer, where the difference in the mean buoyancy between turbulent and non-turbulent regions increases, the mean velocity tends to zero in both regions and hence the mean difference term is also small there. This illustrates how nuanced the situation is, in that the mean buoyancy and mean vertical velocity *can* differ quite substantially between turbulent and non-turbulent regions, but the differences depend on height and precisely where there is a large difference in one variable between the two regions, it is cancelled out by an approximate equivalence between the two regions in the other variable.

B.5.2 Why does the buoyancy flux in turbulent regions not increase with wind shear?

We have seen that the turbulent contribution dominates the buoyancy flux, but that as wind shear increases, the magnitude of $\langle b'w' \rangle_T$ does not increase as one might expect from the increase in TKE. This leads us to examine more closely the second hypothesis posed in Section B.1 about whether wind shear generates more vigorous fluctuations within the turbulent region.

In Fig. B.8, we show the buoyancy and vertical velocity root-mean-square (r.m.s.) conditioned to turbulent regions. At the height of minimum buoyancy flux, $(b_{rms})_T$ in the sheared case is at least 50% larger than in the shear-free case (panel (b)), even though the vertical profiles lie on top of each other (panel (a)). In contrast, the vertical velocity r.m.s. in turbulent regions is hardly affected by wind shear (panel (d)), even though the vertical profile changes (panel (c)). This behavior occurs because wind shear compounds two effects; firstly, the change in the vertical profile and secondly, the change in the height of $z_{i,f}$. In the case of $(b_{rms})_T$, the profiles are increasing with height and as $z_{i,f}$ moves up with shear, buoyancy fluctuations are larger at that reference height in the sheared case. For $(w_{rms})_T$ on the other hand, the profile is decreasing in the shear-free

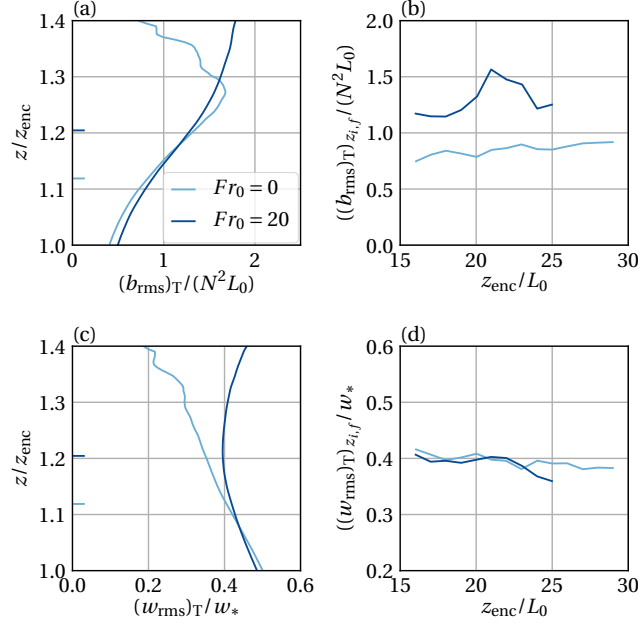


Figure B.8: (Top row) buoyancy r.m.s. and (bottom row) vertical velocity r.m.s. in turbulent regions as a function of (left column) height at $z_{\text{enc}}/L_0 = 20$ and (right column) time at $z_{i,f}$ for $Fr_0 = 0$ and $Fr_0 = 20$. The markers on the left-hand side in panels (a) and (c) indicate $z_{i,f}$.

case, whereas it curves back on itself in the sheared case. Hence the change in the profile and the change in the height of $z_{i,f}$ occur in such a way that they effectively cancel out. This highlights the difficulty of ascertaining shear effects on entrainment zone properties, as different effects can compensate each other.

It is perhaps surprising at first that the buoyancy flux within turbulent regions remains unchanged, or even weakens with wind shear (Fig. B.6b,c), despite buoyancy fluctuations becoming stronger in turbulent regions at $z_{i,f}$ (Fig. B.8b). However, as we have seen, vertical velocity fluctuations in turbulent regions at the same reference height do not increase with wind shear (Fig. B.8d). This suggests that the two signals are not in phase with one another.

Kim et al. (2003) found that above $z_{i,f}$, temperature fluctuations tend to advance vertical velocity fluctuations with a phase difference of around $\pi/2$ and hence the buoyancy flux weakens, even though fluctuations are strong. We see here that when conditioned to turbulent patches, a phase difference must also exist at $z_{i,f}$. We quantify this by calculating the correlation coefficient between buoyancy and vertical velocity fluctuations within turbulent regions, as shown in Fig. B.9. In the shear-free case, vertical velocity fluctuations are induced by buoyancy forces and there is a negative peak in the correlation due to warmer air moving down and cooler air moving up. When wind shear is added to the system, buoyancy is no longer the only external source of vertical velocity fluctuations and the correlation consequently decreases.

By expressing the buoyancy flux in terms of the correlation coefficient:

$$\langle b'w' \rangle_T = (\rho_{bw})_T (b_{\text{rms}})_T (w_{\text{rms}})_T, \quad (\text{B.15})$$

it becomes clear that even though the buoyancy r.m.s. becomes stronger in turbulent regions at $z_{i,f}$, the decrease in the correlation coefficient compensates, or even over-compensates that increase, such that the buoyancy flux remains similar or weakens within turbulent regions under sheared conditions.

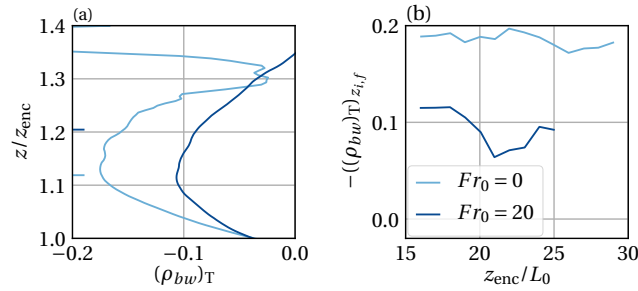


Figure B.9: Correlation between buoyancy and vertical velocity fluctuations in turbulent regions as a function of (a) height at $z_{\text{enc}}/L_0 = 20$ and (b) time at $z_{i,f}$. The markers on the left-hand side in panel (a) indicate $z_{i,f}$.

B.6 SUMMARY AND CONCLUSIONS

The shear enhancement of the entrainment flux in the CBL is compounded by external intermittency. Analysis tools employed in the past have not distinguished the various effects that wind shear can have on properties within turbulent and non-turbulent regions. Here we have employed conditional analysis on direct numerical simulations of the shear-free and sheared CBL to investigate what this method can reveal about shear effects on entrainment that is otherwise hidden by conventional statistics.

We have shown that even with the moderate Reynolds numbers we are able to achieve in our simulations, a clear distinction between turbulent and non-turbulent fluid is possible. Peaks in the probability density function of enstrophy representing the turbulent boundary layer and the non-turbulent free atmosphere are separated by two orders of magnitude. There is a similarly wide range of thresholds on enstrophy where the conditioning is meaningful, in that the turbulent area fraction in the entrainment zone is neither zero nor one and the conditional statistics differ from the conventional statistics.

As a first application, we have demonstrated the utility of this kind of conditioning for understanding shear effects on entrainment. We have found that the largest contribution to the entrainment flux ratio, $-\langle b'w' \rangle_{z_{i,f}}/B_0$, comes from turbulent regions and not from the difference in mean properties between turbulent and non-turbulent regions. Yet the main reason that the entrainment flux ratio increases with wind shear is *not* because the flux itself becomes stronger in turbulent regions, despite what might be expected from the increase in turbulent kinetic energy. Although buoyancy fluctuations do become stronger under sheared conditions, there is a compensating effect due to the decrease in the correlation between buoyancy and vertical velocity fluctuations. Hence, the main reason the entrainment flux increases with wind shear is simply due to there being a larger turbulent area in which entrainment can take place more efficiently than in non-turbulent regions.

The potential applications of this kind of conditional analysis need not be restricted to the dry CBL. Cloud boundaries co-exist with the turbulent/non-turbulent interface, but do not normally coincide (Moeng et al., 2005; Mellado et al., 2017). Whilst conditioning on the liquid water content to distinguish between cloudy and non-cloudy air has been used in the past to study various aspects of cloud mass transport, entrainment and detrainment (de Roode and Wang, 2007; Jonker, 2008), further useful insights may well be gained by conditioning statistics on either side of the turbulent/non-turbulent interface.

ACKNOWLEDGEMENTS

We thank A. Haghshenas for running the $Re_0 = 42$ simulations and for discussing the $Fr_0 = 20$ case with K. Fodor. The authors also acknowledge the Gauss Centre for Supercomputing e.V. (www.gauss-centre.eu) for providing computing time through the John von Neumann Institute for Computing (NIC) on the GCS Supercomputer JUWELS at Jülich Supercomputing Centre (JSC). This work is supported by the Priority Programme SPP 1881 Turbulent Superstructures of the Deutsche Forschungsgemeinschaft (DFG). Primary data and scripts used in the analysis and other supporting information that may be useful in reproducing the authors' work are archived by the Max Planck Institute for Meteorology and can be obtained at [link to be provided].

APPENDIX B.A: DEPENDENCE ON ENSTROPY THRESHOLD

To ascertain to what extent our results regarding wind shear effects on the buoyancy flux, the buoyancy r.m.s. and the vertical velocity r.m.s. depend on the threshold chosen to distinguish turbulent from non-turbulent regions, we examine these properties as a function of threshold. In the following, we essentially answer the question: if the threshold in the shear-free and sheared cases is comparable, and that threshold changes within a given range, does the relationship between the two cases change?

Fig. B.10a,b shows the conditioned buoyancy flux at $z_{i,f}$. As explained in Section B.4, non-turbulent statistics (left column of Fig. B.10) in the limit of increasing thresholds converge with turbulent statistics (right column of Fig. B.10) in the limit of decreasing thresholds and this converged profile is equivalent to the conventional statistic. Within the range of thresholds $-1.5 \lesssim \log_{10}(\omega_{th}^2/\omega_0^2) \lesssim 0.5$ given in Section B.4, where the turbulent area fraction is neither zero nor one and the conditioning may be considered meaningful, $\langle b'w' \rangle_T$ at $z_{i,f}$ is similar, or smaller at $Fr_0 = 20$ compared to $Fr_0 = 0$. Hence this result is not an outcome of the specific threshold we chose.

Fig. B.10c,d demonstrates that the increase of the buoyancy r.m.s. with wind shear is also independent of the specific threshold chosen. Both $(b_{rms})_T$ and $(b_{rms})_{NT}$ are larger at $z_{i,f}$ in the $Fr_0 = 20$ case across the full range of thresholds considered. Fig. B.10e,f shows that $(w_{rms})_T$ at $z_{i,f}$ remains similar between $Fr_0 = 0$ and $Fr_0 = 20$ for a comparable threshold within the range $-1.5 \lesssim \log_{10}(\omega_{th}^2/\omega_0^2) \lesssim 0.5$.

APPENDIX B.B: REYNOLDS NUMBER DEPENDENCE

Since we are restricted to low-to-moderate Reynolds numbers, it is worthwhile to consider the extent to which changes to the Reynolds number influence our results. Reynolds number effects are strongest for the shear-free case so in this section, we only show results relating to $Fr_0 = 0$.

As expected, Fig. B.11 indicates that the scale separation between the boundary layer and free atmosphere increases with Reynolds number. The scale ω_0^2 characterizes the enstrophy in the mixed layer for all Reynolds numbers considered and as the Reynolds number is increased, the characteristic vorticity magnitudes in the free atmosphere decrease in comparison, as seen by a shift in the upper lobes of the PDFs towards smaller normalized enstrophy values. Correspondingly, the saddle point also moves to smaller enstrophy values.

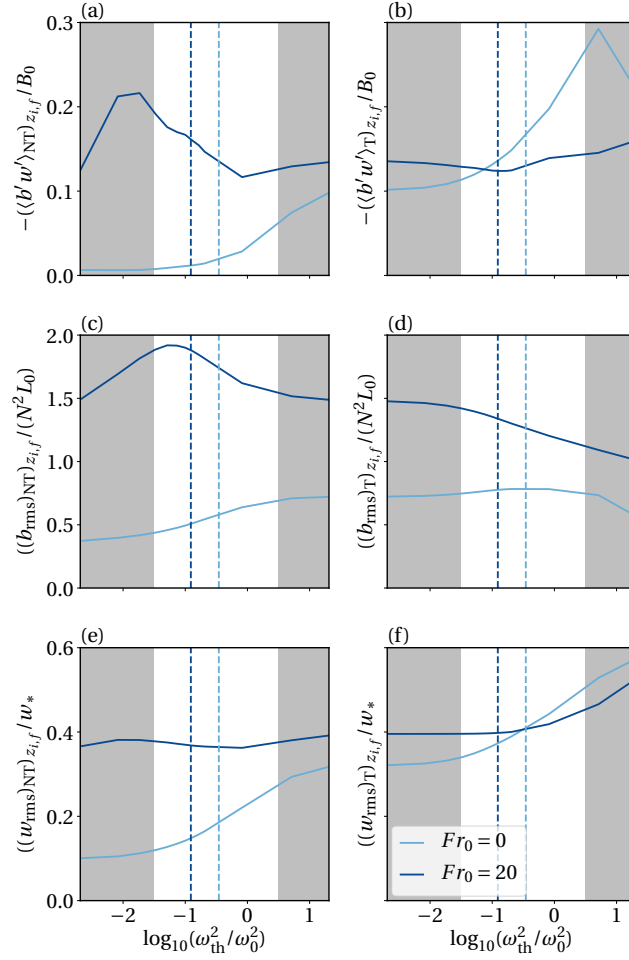


Figure B.10: (a),(b) Buoyancy flux, (c),(d) buoyancy r.m.s. and (e),(f) vertical velocity r.m.s. at $z_{i,f}$ conditioned to (left column) non-turbulent and (right column) turbulent regions as a function of entrainment threshold at $z_{\text{enc}}/L_0 = 20$. The dashed lines indicate the reference threshold defined in Section B.3. The grey shaded areas indicate the range of thresholds where the turbulent area fraction in the shear-free case is greater than 0.9 or less than 0.1.

The change in the PDFs with increasing Reynolds number is also reflected by the turbulent area fraction in Fig. B.12. Contours indicating a non-zero turbulent area fraction in the free atmosphere show a marked shift towards lower normalized enstrophy values as Re_0 increases from 25 to 117. The contours within the upper entrainment zone sublayer (i.e. around the height $z_{i,g}$) consequently flatten. This suggests that at the very high Reynolds numbers that characterize the real CBL, the turbulent area fraction would become very insensitive to the threshold in the upper entrainment zone sublayer.

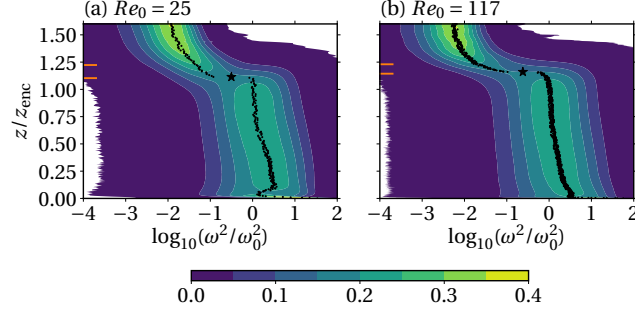


Figure B.11: Probability distribution functions of enstrophy at $z_{\text{enc}}/L_0 = 20$. The black dots indicate the maximum in the PDF at each height. The star shows the approximate saddle point. The heavy orange markers on the side indicate (lower) $z_{i,f}$ and (upper) $z_{i,g}$. The reference scale ω_0^2 is defined in Eq. (B.13) with $c_\varepsilon = 0.1$.

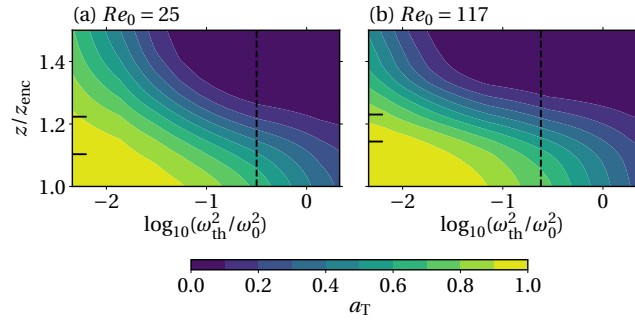


Figure B.12: Turbulent area fraction as a function of height and enstrophy threshold at $z_{\text{enc}}/L_0 = 20$. The black dashed line indicates the magnitude at which the saddle point in Fig. B.11 is located. The black markers on the left-hand side indicate (lower) $z_{i,f}$ and (upper) $z_{i,g}$.

BIBLIOGRAPHY

- Adrian, R., R. Ferreira, and T. Boberg (1986). "Turbulent thermal convection in wide horizontal fluid layers". *Exp. Fluids* 4, pp. 121–141.
- Adrian, R.J. (1996). "Variation of temperature and velocity fluctuations in turbulent thermal convection over horizontal surfaces". *Int. J. Heat Mass Transfer* 39, pp. 2303–2310.
- Adrian, R.J. (2007). "Hairpin vortex organization in wall turbulence". *Physics of Fluids* 19, p. 041301.
- Ansorge, C. (2017). *Analyses of Turbulence in the Neutrally and Stably Stratified Planetary Boundary Layer*. Springer.
- Ansorge, C. and J.P. Mellado (2014). "Global Intermittency and Collapsing Turbulence in the Stratified Planetary Boundary Layer". *Boundary-Layer Meteorol.* 153, pp. 89–116.
- Ansorge, C. and J.P. Mellado (2016). "Analyses of external and global intermittency in the logarithmic region of Ekman flow". *J. Fluid Mech.* 805, pp. 611–635.
- Antonia, R.A. (1981). "Conditional Sampling in Turbulence Measurement". *Annu. Rev. Fluid Mech.* 13, pp. 131–156.
- Atkinson, B.W. and J.W. Zhang (1996). "Mesoscale shallow convection in the atmosphere". *Rev. Geophys* 34, pp. 403–431.
- Balakumar, B.J. and R.J. Adrian (2007). "Large- and very-large-scale motions in channel and boundary-layer flows". *Philos. Trans. Royal Soc. A* 365.
- Barnier, B. (1998). "Forcing the Ocean". In: *Ocean Modeling and Parameterization*. Ed. by E.P. Chassignet and J. Verron. Kluwer Academic Publishers, pp. 45–80.
- Berkooz, G., P. Holmes, and J.L. Lumley (1993). "The Proper Orthogonal Decomposition in the Analysis of Turbulent Flows". *Annu. Rev. Fluid Mech.* 25, pp. 539–575.
- Bisset, D.K., J.C.R. Hunt, and M.M. Rogers (2002). "The turbulent/non-turbulent interface bounding a far wake". *J. Fluid Mech.* 451, pp. 383–410.
- Bonan, G. (2008). *Ecological Climatology: Concepts and Applications*. 2nd edition. Cambridge University Press.
- Bony, S., B. Stevens, D.M.W. Frierson, C. Jakob, M. Kageyama, R. Pincus, T.G. Shepherd, S.C. Sherwood, A.P. Siebesma, A.H. Sobel, M. Watanabe, and M.J. Webb (2015). "Clouds, circulation and climate sensitivity". *Nature Geoscience* 8, pp. 261–268.
- Bony, S. et al. (2017). "EUREC4A: A Field Campaign to Elucidate the Couplings Between Clouds, Convection and Circulation". *Surv. Geophys.* 38, pp. 1529–1568.
- Borrell, G. and J. Jiménez (2016). "Properties of the turbulent/non-turbulent interface in boundary layers". *J. Fluid Mech.* 801, pp. 554–596.
- Bradshaw, P. (1972). "The understanding and prediction of turbulent flow". *The Aeronautical Journal* 76, pp. 403–418.
- Buckingham, E. (1914). "On Physically Similar Systems; Illustrations of the Use of Dimensional Equations". *Phys. Rev.* 4, pp. 345–376.
- Businger, J.A., J-C. Wyngaard, Y. Izumi, and P-F. Bradley (1971). "Flux-Profile Relationships in the Atmospheric Surface Layer". *J. Atmos. Sci.* 28, pp. 181–189.
- Businger, J.A. (1973). "A note on free convection". *Boundary-Layer Meteorol.* 4, pp. 323–326.
- Cantwell, B.J. (1981). "Organized Motion in Turbulent Flow". *Annu. Rev. Fluid Mech.* 13, pp. 457–515.

- Carpenter, M. and C. Kennedy (1994). *Fourth-Order 2N-Storage Runge-Kutta Schemes*. Tech. rep. NASA Technical Memorandum 109112. NASA Langley Research Center.
- Carson, D.J. and F.B. Smith (1975). "Thermodynamic model for the development of a convectively unstable boundary layer". *Adv. Geophys.* 18, pp. 111–124.
- Caughey, S.J. (1982). "Observed characteristics of the atmospheric boundary layer". In: *Atmospheric Turbulence and Air Pollution Modelling*. Ed. by F.T.M. Nieuwstadt and H. van Dop. D. Riedel Publishing Company, pp. 107–158.
- Charney, J.G. and A. Eliassen (1964). "On the Growth of the Hurricane Depression". *J. Atmos. Sci.* 21, pp. 68–75.
- Chesnutt, C.W. (1999). "Obliterating the Color Line". In: *Charles W. Chesnutt: Essays and Speeches*. Ed. by J.R. McElrath Jr., R.C. Leitz III, and J.S. Crisler. Stanford University Press, pp. 170–171.
- Chillà, F. and J. Schumacher (2012). "New perspectives in turbulent Rayleigh-Bénard convection". *Eur. Phys. J. E* 35, p. 58.
- Chung, D. and G. Matheou (2012). "Direct numerical simulation of stationary homogeneous stratified shear turbulence". *J. Fluid Mech.* 696, pp. 434–467.
- Conzemius, R. and E. Fedorovich (2006). "Dynamics of Sheared Convective Boundary Layer Entrainment. Part I: Methodological Background and Large-Eddy Simulations". *J. Atmos. Sci.* 63, pp. 1151–1178.
- Corrsin, S. and A.L. Kistler (1955). *Free-Stream Boundaries of Turbulent Flows*. Tech. rep. 1244. The Johns Hopkins University.
- Couvreux, F., F. Hourdin, and C. Rio (2010). "Resolved Versus Parametrized Boundary-Layer Plumes. Part I: A Parametrization-Oriented Conditional Sampling in Large-Eddy Simulations". *Boundary-Layer Meteorol.* 134, pp. 441–458.
- de Bruin, H.A.R., W. Kohsiek, and B.J.J.M. van den Hurk (1993). "A verification of some methods to determine the fluxes of momentum, sensible heat, and water vapour using standard deviation and structure parameter of scalar meteorological quantities". *Boundary-Layer Meteorol.* 63, pp. 231–257.
- de Roode, S.R. and Q. Wang (2007). "Do stratocumulus clouds detrain? FIRE I data revisited". *Boundary-Layer Meteorol.* 122, pp. 479–491.
- Deardorff, J. (1970a). "Preliminary Results from Numerical Integrations of the Unstable Planetary Boundary Layer". *J. Atmos. Sci.* 27, pp. 1209–1211.
- Deardorff, J. (1970b). "Convective Velocity and Temperature Scales for the Unstable Planetary Boundary Layer and for Rayleigh Convection". *J. Atmos. Sci.* 27, pp. 1211–1213.
- Deardorff, J.W., G.E. Willis, and B.H. Stockton (1980). "Laboratory studies of the entrainment zone of a convectively mixed layer". *J. Fluid Mech.* 100, pp. 41–64.
- Dimotakis, P.E. and G.L. Brown (1976). "The mixing layer at high Reynolds number: large-structure dynamics and entrainment". *J. Fluid Mech.* 78, pp. 535–560.
- Dopazo, C. (1977). "On conditioned averages for intermittent turbulent flows". *J. Fluid Mech.* 81, pp. 433–438.
- Dougherty, J.P. (1961). "The anisotropy of turbulence at the meteor level". *J. Atmos. Terr. Phys.* 21, pp. 210–213.
- Emanuel, K.A. (1991). "The Theory of Hurricanes". *Annu. Rev. Fluid Mech.* 23, pp. 179–196.
- Emmitt, G.D. (1978). "Tropical Cumulus Interaction with and Modification of the Sub-cloud Region". *J. Atmos. Sci.* 35, pp. 1485–1502.
- Emran, M.S. and J. Schumacher (2015). "Large-scale mean patterns in turbulent convection". *J. Fluid Mech.* 776, pp. 96–108.

- Fedorovich, E. and R. Conzemius (2008). "Effects of wind shear on the atmospheric convective boundary layer structure and evolution". *Acta Geophysica* 56, pp. 114–141.
- Fedorovich, E., R. Conzemius, and D. Mironov (2004). "Convective Entrainment into a Shear-Free, Linearly Stratified Atmosphere: Bulk Models Reevaluated through Large Eddy Simulations". *J. Atmos. Sci.* 61, pp. 281–295.
- Foias, C., D. Holm, and E. Titi (2001). "The Navier-Stokes-alpha model of fluid turbulence". *Physica D* 152-153, pp. 505–519.
- Frisch, U. and S.A. Orszag (1990). "Turbulence: Challenges for Theory and Experiment". *Phys. Today* 43, pp. 24–32.
- Garcia, J.R. and J.P. Mellado (2014). "The Two-Layer Structure of the Entrainment Zone in the Convective Boundary Layer". *J. Atmos. Sci.* 71, pp. 1935–1955.
- Garratt, J.R. (1992). *The atmospheric boundary layer*. Cambridge University Press.
- Guervilly, C., D.W. Hughes, and C.A. Jones (2014). "Large-scale vortices in rapidly rotating Rayleigh-Bénard convection". *J. Fluid Mech.* 758, pp. 407–435.
- Haghshenas, A. and J.P. Mellado (2019). "Characterization of wind-shear effects on entrainment in a convective boundary layer". *J. Fluid Mech.* 858, pp. 145–183.
- Hardenberg, J. von, A. Parodi, G. Passoni, A. Provenzale, and E.A. Spiegel (2008). "Large-scale patterns in Rayleigh-Bénard convection". *Phys. Lett. A* 372, pp. 2223–2229.
- Hartlep, T., A. Tilgner, and F.H. Busse (2003). "Large Scale Structures in Rayleigh-Bénard Convection at High Rayleigh Numbers". *Phys. Rev. Lett* 91, p. 064501.
- Hirsch, M.W. (1984). "The Dynamical Systems Approach to Differential Equations". *Bull. Amer. Math. Soc.* 11, pp. 1–64.
- Högström, U. (1996). "Review of some basic characteristics of the atmospheric surface layer". *Boundary-Layer Meteorol.* 78, pp. 215–246.
- Holzner, M. and M. van Reeuwijk (2017). "The turbulent/nonturbulent interface in penetrative convection". *J. Turbul.* 18, pp. 260–270.
- Johansson, C., A.-S. Smedman, U. Högström, J.G. Brasseur, and S. Khanna (2001). "Critical Test of the Validity of Monin-Obukhov Similarity during Convective Conditions". *J. Atmos. Sci.* 58, pp. 1549–1566.
- Jonker, H.J.J. (2008). "A refined view of vertical mass transport by cumulus convection". *Geophys. Res. Lett.* 35, p. L07810.
- Jonker, H.J.J., M. van Reeuwijk, P. Sullivan, and E. Patton (2013). "On the scaling of shear-driven entrainment: a DNS study". *J. Fluid Mech.* 732, pp. 150–165.
- Kader, B.A. and A.M. Yaglom (1990). "Mean fields and fluctuation moments in unstably stratified turbulent boundary layers". *J. Fluid Mech.* 212, pp. 637–662.
- Kaimal, J.-C., J.-C. Wyngaard, D.-A. Haugen, O.-R. Coté, and Y. Izumi (1976). "Turbulence Structure in the Convective Boundary Layer". *J. Atmos. Sci.* 33, pp. 2152–2169.
- Khanna, S. and J.G. Brasseur (1997). "Analysis of Monin-Obukhov similarity from large-eddy simulation". *J. Fluid Mech.* 345, pp. 251–286.
- Khanna, S. and J.G. Brasseur (1998). "Three-Dimensional Buoyancy- and Shear-Induced Local Structure of the Atmospheric Boundary Layer". *J. Atmos. Sci.* 55, pp. 710–743.
- Kim, K.C. and R.J. Adrian (1999). "Very large-scale motion in the outer layer". *Physics of Fluids* 11, p. 417.
- Kim, S.-W., S.-U. Park, and C.-H. Moeng (2003). "Entrainment Processes in the Convective Boundary Layer with Varying Wind Shear". *Boundary Layer Meteorol.* 108, pp. 221–245.
- Kline, S.J., W.C. Reynolds, F.A. Schraub, and P.W. Runstadler (1967). "The structure of turbulent boundary layers". *J. Fluid Mech.* 30, pp. 741–773.
- Koschmieder, E.L. (1979). "Turbulent Taylor vortex flow". *J. Fluid Mech.* 93, pp. 515–527.

- Kovaszny, L.S.G., V. Kibens, and R.F. Blackwelder (1970). "Large-scale motion in the intermittent region of a turbulent boundary layer". *J. Fluid Mech.* 41, pp. 283–325.
- Kraichnan, R.H. (1962). "Turbulent Thermal Convection at Arbitrary Prandtl Number". *Physics of Fluids* 5, pp. 1374–1389.
- Lele, S. (1992). "Compact Finite Difference Schemes with Spectral-like Resolution". *J Comput Phys* 103, pp. 16–42.
- Li, Q., P. Gentine, J.P. Mellado, and K.A. McColl (2018). "Implications of Nonlocal Transport and Conditionally Averaged Statistics on Monin–Obukhov Similarity Theory and Townsend’s Attached Eddy Hypothesis". *J. Atmos. Sci.* 75, pp. 3403–3431.
- Lohou, F., F. Saïd, M. Lothon, P. Durand, and D. Serça (2010). "Impact of Boundary-Layer Processes on Near-Surface Turbulence Within the West African Monsoon". *Boundary-Layer Meteorol.* 136, pp. 1–23.
- Lorenz, E.N. (1963). "Deterministic Nonperiodic Flow". *J. Atmos. Sci.* 20, pp. 130–141.
- Maronga, B. and J. Reuder (2017). "On the Formulation and Universality of Monin–Obukhov Similarity Functions for Mean Gradients and Standard Deviations in the Unstable Surface Layer: Results from Surface-Layer-Resolving Large-Eddy Simulations". *J. Atmos. Sci.* 74, pp. 989–1010.
- McColl, K.A., C.C. van Heerwaarden, G.G. Katul, P. Gentine, and D. Entekhabi (2017). "Role of large eddies in the breakdown of the Reynolds analogy in an idealized mildly unstable atmospheric surface layer". *Q. J. R. Meteorol. Soc.* 143, pp. 2182–2197.
- Mellado, J.P. (2012). "Direct numerical simulation of free convection over a heated plate". *J. Fluid Mech.* 712, pp. 418–450.
- Mellado, J.P. (2017). "Cloud-Top Entrainment in Stratocumulus Clouds". *Annu. Rev. Fluid Mech.* 49, pp. 145–169.
- Mellado, J.P. and C. Ansorge (2012). "Factorization of the Fourier transform of the pressure-Poisson equation using finite differences in colocated grids". *Z. Angew. Math. Mech.* 92, pp. 380–392.
- Mellado, J.P., C.S. Bretherton, B. Stevens, and M.C. Wyant (2018). "DNS and LES for Simulating Stratocumulus: Better Together". *J. Adv. Model. Earth Sy.* 10.
- Mellado, J.P., M. Puche, and C.C. van Heerwaarden (2017). "Moisture statistics in free convective boundary layers growing into linearly stratified atmospheres". *Q. J. R. Meteorol. Soc.* 143, pp. 2403–2419.
- Mellado, J.P., C.C. van Heerwaarden, and J.R. Garcia (2016). "Near-Surface Effects of Free Atmosphere Stratification in Free Convection". *Boundary-Layer Meteorol.* 159, pp. 69–95.
- Mellado, J.P., L. Wang, and N. Peters (2009). "Gradient trajectory analysis of a scalar field with external intermittency". *J. Fluid Mech.* 626, pp. 333–365.
- Moeng, C.-H. and R. Rottuno (1990). "Vertical Velocity Skewness in the Buoyancy-Driven Boundary Layer". *J. Atmos. Sci.* 47, pp. 1149–1162.
- Moeng, C.-H. (1998). "Stratocumulus-Topped Atmospheric Planetary Boundary Layer". In: *Buoyant Convection in Geophysical Flows*. Ed. by E.J. Plate, E.E. Fedorovich, D.X. Viegas, and J.C. Wyngaard. Kluwer Academic Publishers, pp. 421–440.
- Moeng, C.-H., B. Stevens, and P.P. Sullivan (2005). "Where is the Interface of the Stratocumulus-Topped PBL?" *J. Atmos. Sci.* 62, pp. 2626–2631.
- Moin, P. and K. Mahesh (1998). "Direct Numerical Simulation: A Tool in Turbulence Research". *Annu. Rev. Fluid Mech.* 30, pp. 539–578.
- Monin, A.S. and A.M. Obukhov (1954). "Basic laws of turbulent mixing in the surface layer of the atmosphere". *Tr. Akad. Nauk SSSR Geophys. Inst.* 24, pp. 163–187.
- Montgomery, M.T. and R.K. Smith (2014). "Paradigms for tropical cyclone intensification". *Aust. Meteorol. Ocean Journal* 64, pp. 37–66.

- Neggers, R., B. Stevens, and J.D. Neelin (2006). "A simple equilibrium model for shallow-cumulus-topped mixed layers". *Theor. Comput. Fluid Dyn.* 20, pp. 305–322.
- Nordlund, Å., R.F. Stein, and M. Asplund (2009). "Solar Surface Convection". *Living Rev. Solar Phys.* 6.
- Ooyama, K. (1969). "Numerical Simulation of the Life Cycle of Tropical Cyclones". *J. Atmos. Sci.* 26, pp. 3–40.
- Ozmidov, R.V. (1965). "On the turbulent exchange in a stably stratified ocean". *Izv. Acad. Sci. USSR Atmos. Ocean Phys.* 1 (8), pp. 853–860.
- Pandey, A., J.D. Scheel, and J. Schumacher (2018). "Turbulent superstructures in Rayleigh-Bénard convection". *Nat. Commun.* 9, p. 2118.
- Panofsky, H-A., H. Tennekes, D-H. Lenschow, and J-C. Wyngaard (1977). "The characteristics of turbulent velocity components in the surface layer under convective conditions". *Boundary-Layer Meteorol.* 11, pp. 355–361.
- Park, S-B, P. Gentine, K. Schneider, and M. Farge (2016). "Coherent Structures in the Boundary and Cloud Layers: Role of Updrafts, Subsiding Shells and Environmental Subsidence". *J Atmos Sci* 73, pp. 1789–1814.
- Pino, D. and J. Vilà-Guerau de Arrellano (2006). "Effects of shear in the convective boundary layer: analysis of the turbulent kinetic energy budget". *Acta Geophysica* 56, pp. 167–193.
- Pino, D., J. Vilà-Guerau de Arrellano, and P. Duynkerke (2003). "The Contribution of Shear to the Evolution of a Convective Boundary Layer". *J. Atmos. Sci.* 60, pp. 1913–1926.
- Pirozolli, S., M. Bernardini, R. Verzicco, and P. Orlandi (2017). "Mixed convection in turbulent channels with unstable stratification". *J. Fluid Mech.* 821, pp. 482–516.
- Pope, S.B. (2000). *Turbulent Flows*. Cambridge University Press.
- Prandtl, L. (1904). "Über Flüssigkeitsbewegung bei sehr kleiner Reibung". In: *Verhandl. III Intern. Math. Kongr. Heidelberg*, pp. 484–491. Engl. transl. NACA Tech. Mem. 452.
- Prandtl, L. (1932). "Meteorologische Anwendung der Strömungslehre". *Beitr. Phys. Atmos.* 19, pp. 188–202.
- Priestley, C.H.B. (1954). "Convection from a large horizontal surface". *Aust J Phys* 7, pp. 176–201.
- Puits, R. du and C. Willert (2016). "The evolution of the boundary layer in turbulent Rayleigh-Bénard convection in air". *Phys. Fluids* 28, p. 044108.
- Rao, K.N., R. Narashimha, and M.A.B. Narayanan (1971). "The 'bursting' phenomenon in a turbulent boundary layer". *J. Fluid Mech.* 48, pp. 339–352.
- Raupach, M.R., R.A. Antonia, and S. Rajagopalan (1991). "Rough-wall turbulent boundary layers". *Appl. Mech. Rev.* 44, pp. 1–25.
- Rieck, M., L. Nuijens, and B. Stevens (2012). "Marine Boundary Layer Cloud Feedbacks in a Constant Relative Humidity Atmosphere". *J. Atm. Sci* 69, pp. 2538–2550.
- Roode, S.R. de, P.G. Duynkerke, and H.J.J. Jonker (2004). "Large-Eddy Simulation: How Large is Large Enough?" *J. Atmos. Sci.* 61, pp. 403–421.
- Salesky, S.T. and W. Anderson (2018). "Buoyancy effects on large-scale motions in convective atmospheric boundary layers: implications for modulation of near-wall processes". *J. Fluid Mech.* 856, pp. 135–168.
- Salesky, S.T., M. Chamecki, and E. Bou-Zeid (2017). "On the Nature of the Transition Between Roll and Cellular Organization in the Convective Boundary Layer". *Boundary-Layer Meteorol.* 163, pp. 41–68.
- Schlichting, H. (1979). *Boundary-Layer Theory*. 7th edition. McGraw-Hill.

- Schmidt, H. and U. Schumann (1989). "Coherent structure of the convective boundary layer derived from large-eddy simulation". *J. Fluid Mech.* 200, pp. 511–562.
- Schulz, B. (2019). "On the Role of Wind Shear and Cloud Droplet Sedimentation on Entrainment in Stratocumulus". PhD thesis. Universität Hamburg.
- Schumann, U. and C-H. Moeng (1991). "Plume Fluxes in Clear and Cloudy Convective Boundary Layers". *J. Atmos. Sci.* 48, pp. 1746–1757.
- Shah, S.K. and E. Bou-Zeid (2014). "Direct numerical simulations of turbulent Ekman layers with increasing static stability: modifications to the bulk structure and second-order statistics". *J. Fluid Mech.* 760, pp. 494–539.
- Sherwood, S.C., S. Bony, and J.-L. Dufresne (2014). "Spread in model climate sensitivity traced to atmospheric convective mixing". *Nature* 505, pp. 37–42.
- Shishkina, O., S. Horn, S. Wagner, and E. Ching (2015). "Thermal Boundary Layer Equation for Turbulent Rayleigh-Bénard Convection". *Phys. Rev. Lett.* 114, p. 114302.
- Shishkina, O., R.J.A.M. Stevens, S. Grossmann, and D. Lohse (2010). "Boundary layer structure in turbulent thermal convection and its consequences for the required numerical resolution". *New J. Phys.* 12, p. 075022.
- Siebert, H. and R.A. Shaw (2017). "Supersaturation Fluctuations during the Early Stage of Cumulus Formation". *J. Atmos. Sci.* 74, pp. 975–988.
- Siebert, H. et al. (n.d.). "Observations of Aerosol, cloud, turbulence and radiation properties at the top of the marine boundary layer over the Subtropical North-Eastern Atlantic Ocean: The ACORES campaign". In preparation.
- Siebesma, A. and J. Cuijpers (1995). "Evaluation of Parametric Assumptions for Shallow Cumulus Convection". *J. Atmos. Sci.* 52, pp. 650–666.
- Siebesma, A.P. (1998). "Shallow Cumulus Convection". In: *Buoyant Convection in Geophysical Flows*. Ed. by E.J. Plate, E.E. Fedorovich, D.X. Viegas, and J.C. Wyngaard. Kluwer Academic Publishers, pp. 441–486.
- Siebesma, A.P., P.M.M. Soares, and J. Teixeira (2007). "A Combined Eddy-Diffusivity Mass-Flux Approach for the Convective Boundary Layer". *J. Atmos. Sci.* 64, pp. 1230–1248.
- Silva, C. da, J. Hunt, I. Eames, and J. Westerweel (2014). "Interfacial Layers Between Regions of Different Turbulent Intensity". *Annu. Rev. Fluid Mech.* 46, pp. 567–590.
- Sorbjan, Z. (1996). "Numerical Study of Penetrative and "Solid Lid" Nonpenetrative Convective Boundary Layers". *J. Atmos. Sci.* 53, pp. 101–112.
- Stewart, R.W. (1969). "Turbulence and waves in a stratified atmosphere". *Radio Science* 4, pp. 1269–1278.
- Stewart, R.W. (1979). *The Atmospheric Boundary Layer*. World Meteorological Organization.
- Stull, R.B. (1988). *An Introduction to Boundary-Layer Meteorology*. Kluwer Academic Publishers.
- Sullivan, P.P., C.-H. Moeng, B. Stevens, D.H. Lenschow, and S.D. Mayor (1998). "Structure of the Entrainment Zone Capping the Convective Atmospheric Boundary Layer". *J. Atmos. Sci.* 55, pp. 3042–3064.
- Thom, R. (1975). *Structural Stability and Morphogenesis*. W.A. Benjamin, Inc.
- Townsend, A. (1959). "Temperature fluctuations over a heated horizontal surface". *J. Fluid Mech.* 5, pp. 209–241.
- Townsend, A.A. (1976). *The Structure of Turbulent Shear Flow*. 2nd ed. Cambridge University Press.
- Tsinober, A. (2009). *An Informal Conceptual Introduction to Turbulence*. Springer.

- van de Boer, A., A.F. Moene, A. Graf, D. Schüttemeyer, and C. Simmer (2014). "Detection of Entrainment Influences on Surface-Layer Measurements and Extension of Monin-Obukhov Similarity Theory". *Boundary-Layer Meteorol.* 152, pp. 19–44.
- van Reeuwijk, M. and M. Holzner (2014). "The turbulence boundary of a temporal jet". *J. Fluid Mech.* 739, pp. 254–275.
- van Reeuwijk, M., H.J.J. Jonker, and K. Hanjalić (2008). "Wind and boundary layers in Rayleigh Bénard convection. II. Boundary layer character and scaling". *Phy. Rev. E* 77, p. 036312.
- van Reeuwijk, M., D. Krug, and M. Holzner (2018). "Small-scale entrainment in inclined gravity currents". *Environ. Fluid Mech.* 18, pp. 225–239.
- van Stratum, B.J.H., J. Vilá-Guerau de Arellano, C.C. van Heerwaarden, and H.G. Ouwens (2014). "Subcloud-Layer Feedbacks Driven by the Mass Flux of Shallow Cumulus Convection over Land". *J. Atmos. Sci.* 71, pp. 881–895.
- Warhaft, Z. (2000). "Passive Scalars in Turbulent Flows". *Annu. Rev. Fluid Mech.* 32, pp. 203–240.
- Watanabe, T., X. Zhang, and K. Nagata (2018). "Turbulent/non-turbulent interfaces detected in DNS of incompressible turbulent boundary layers". *Phys. Fluids* 30, p. 035102.
- Wilczak, J.M. (1984). "Large-Scale Eddies in the Unstably Stratified Atmospheric Surface Layer. Part I: Velocity and Temperature Structure". *J. Atmos. Sci.* 41, pp. 3537–3550.
- Williams, A.G. and J.M. Hacker (1992). "The composite shape and structure of coherent eddies in the convective boundary layer". *Boundary-Layer Meteorol.* 61, pp. 213–245.
- Wynngaard, J.-C., O.-R. Coté, and Y. Izumi (1971). "Local Free Convection, Similarity, and the Budgets of Shear Stress and Heat Flux". *J. Atmos. Sci.* 28, pp. 1171–1182.
- Wynngaard, J.C. (2010). *Turbulence in the Atmosphere*. Cambridge University Press.
- Young, G.S. (1988). "Turbulence Structure of the Convective Boundary Layer. Phoenix 78 Aircraft Observations of Thermals and Their Environment". *J. Atmos. Sci.* 45, pp. 727–735.
- Zhang, Y. and S.A. Klein (2010). "Mechanisms Affecting the Transition from Shallow to Deep Convection over Land: Inferences from Observations of the Diurnal Cycle Collected at the ARM Southern Great Plains Site". *J. Atmos. Sci.* 67, pp. 2943–2959.

VERSICHERUNG AN EIDES STATT

Hiermit versichere ich an Eides statt, dass ich die vorliegende Dissertation mit dem Titel: "The Influence of Large Coherent Structures on Near-Surface and Entrainment Zone Properties in Convective Boundary Layers" selbstständig verfasst und keine anderen als die angegebenen Hilfsmittel – insbesondere keine im Quellenverzeichnis nicht benannten Internet-Quellen – benutzt habe. Alle Stellen, die wörtlich oder sinngemäß aus Veröffentlichungen entnommen wurden, sind als solche kenntlich gemacht. Ich versichere witerhin, dass ich die Dissertation oder Teile davon vorher weder im In- noch im Ausland in einem anderen Prüfungsverfahren eingereicht habe und die eingereichte schriftliche Fassung der auf dem elektronischen Speichermedium entspricht.

Hamburg, January 2020

Katherine Fodor

Hinweis / Reference

Die gesamten Veröffentlichungen in der Publikationsreihe des MPI-M
„Berichte zur Erdsystemforschung / Reports on Earth System Science“,
ISSN 1614-1199

sind über die Internetseiten des Max-Planck-Instituts für Meteorologie erhältlich:
<http://www.mpimet.mpg.de/wissenschaft/publikationen.html>

*All the publications in the series of the MPI -M
„Berichte zur Erdsystemforschung / Reports on Earth System Science“,
ISSN 1614-1199*

*are available on the website of the Max Planck Institute for Meteorology:
<http://www.mpimet.mpg.de/wissenschaft/publikationen.html>*

